NBSIR 80-2082

NBS: Materials Measurements

J. R. Manning

National Bureau of Standards
U.S. Department of Commerce
Washington, D.C. 20234
Phone: (301) 921-3354

NBSIR 80-2082

NBS: MATERIALS MEASUREMENTS

J. R. Manning

National Bureau of Standards
U.S. Department of Commerce
Washington, D.C. 20234
Phone: (301) 921-3354

July 1980

Annual Report
For the Period 2 April 1979 - 1 April 1980
NASA Government Order H-27954B
Properties of Electronic Materials

TABLE OF CONTENTS

National Bureau of Standards
Materials Measurements

Summary

This report describes NBS work for NASA in support of NASA's Materials

Processing in Space Program under NASA Government Order H-27954B (Properties

of Electronic Materials) covering the period April 2, 1979 to April 1, 1980.

The work emphasizes materials measurements and has two main thrusts:

1)   Carrying out precision measurements in space and investigating the

feasibility of improved measurements when the space environment offers a

unique opportunity for performing such measurements. These measurements

would be useful for either space processing or processes on the ground.

2)   Obtaining precision measurements on materials properties when these

properties are important to the design and interpretation of space processing

experiments. These measurements would be carried out either in space or on

the ground.

This work has been carried out in four tasks. These tasks have, as two

of their focal points, the role of convection effects and the role of container

effects, both of which would differ in space-based experiments from those

found in ground-based experiments. The results obtained for each task are

given in detailed summaries in the body of the report. Briefly, in Task 1 -

Surface Tensions and Their Variations with Temperature and Impurities -

measurements in an Auger spectrometer of surface impurity concentrations on

liquid gallium showed that the principal impurities were oxygen and carbon.

The impurities showed a tendency to collect into plates or clumps. Heating

in hydrogen atmospheres and ion sputtering were both found to be effective

methods of removing impurities. When these methods of removing impurities

were applied, reproducible surface tension (γ) values at room temperature

were found with $\gamma \simeq 710 \text{ mJ/m}^2$. The surface tension decreased quadratically with increasing temperature to $\gamma \simeq 690 \text{ mJ/m}^2$ at 500 °C. In Task 2 - Solutal Convection During Directional Solidification - in Pb-rich Pb-Sn off-eutectic alloys, macrosegregation caused by solutal convection was not reduced by vertical or horizontal fields of 0.1T, but downward solidification (liquid below solid) virtually eliminated macrosegregation in small ($\sim$ 3 mm) diameter samples. Calculations were made to predict the onset of convective and interfacial instabilities during directional solidification of lead-tin alloys including effects of variations in gravitational acceleration and Prandtl number. Results obtained in calculations with a constant gravitational acceleration of 10^{-6} g_e show a noticeably larger stability range than those for 10^{-4} g_e; at 10^{-6} g_e the instabilities will develop more slowly with time. In Task 3 - A Thermochemical Study of Corrosive Reactions in Oxide Materials - phase assemblages of selected compositions on the joins $K[Fe_{0.5}Si_{0.5}]$ O_2 - SiO_2 and $KFeO_2$ - SiO_2 were determined over a large range of oxygen partial pressures and the temperature range 800 °C to 1400 °C. In melts containing ferrous ions, excessive reaction with platinum containers occurred. In Task 4 - Thermodynamic Properties of Refractory Materials at High Temperatures - use of pyroelectric detectors to determine the radiant heat loss from spherical samples as cooling occurs in free-cooling experiments is being investigated. The heat capacities and, under some conditions, the thermal conductivities in leviatated high temperature materials can be derived from simultaneous measurement of radiant heat loss and rate of temperature change. Details of the thermal gradients to be expected in both metallic and non-metallic samples have been examined. Limitations from sample vaporization will occur when the vapor pressure reaches the vicinity of 10 Pa (10^{-4} atm).

Task 1

Surface Tensions and Their Variations
with Temperature and Impurities

S. C. Hardy
Metallurgy Division
Center for Materials Science

and

J. Fine
Surface Science Division
Center for Thermodynamics and Molecular Science

Summary

The surface tension of gallium has been measured as a function of tem-
perature in vacuum and hydrogen atmospheres using cups of quartz and graphite
to contain the sessile drops. The results are generally in good agreement
with two previous measurements and show that the surface tension decrease is
nearly quadratic in temperature. A non-linear least squares analysis gave
the following function as the best fit to the data:

$$\gamma = 709.9 + .0016 \ (T-29.87) - .0000923 \ (T-29.37)^2.$$

Measurements in vacuum using quartz cups, however, have revealed a complex
heating history dependence which we think is due to an oxide contamination of
the gallium by the quartz.

In related work the surfaces of liquid gallium sessile drops have been
studied in an Auger spectrometer to determine the concentration of impurities.
The gallium surface after formation of the drop was found to be covered with
a solid layer containing a high concentration of oxygen and carbon. Prolonged
heating to several hundred degrees effectively desorbed the oxygen but the
carbon was still present in the form of a precipitate. The conditions under

which these precipitates form is not understood. The surfaces were also cleaned by sputtering with argon ions and complex flow phenomena observed. The surface tension at the melting point of a drop with a sputtered clean surface was in fair agreement with the results of the sessile drop measurements.

Introduction

Studies of liquid gallium surfaces have proceeded along two lines in the past year. Extensive surface tension measurements have been made using the apparatus and techniques described in last year's report. In addition, we have attempted to characterize the surface composition of liquid gallium in an Auger spectrometer. These latter experiments have revealed complex impurity phenomena which we do not fully understand.

The central problem in determining the surface tension of liquids is to produce a clean surface. Segregation of impurities at the liquid-vapor interface will drastically alter the surface tension as described by the Gibb's equation. This sensitivity to surface active impurities is probably the basic cause for the wide discrepancies in reported surface tension values. A related problem is that there is almost no independent characterization of the chemical composition at the interface with a surface tension measurement. It is assumed that the procedures and materials used have produced a clean surface, the cleanest surface being ascribed to the one with the highest surface tension, i.e., the one with the least surface segregation. An independent characterization of the surface by some direct technique would be extremely valuable in the interpretation of surface tension measurements, particularly in cases where there is a wide discrepancy in the results. The Auger work was undertaken primarily to address this problem.

Oxygen is probably the most troublesome surface contaminant for most metals; gallium, which is chemically similar to aluminum, is particularly subject to the formation of stable surface oxides. These may be either

Ga_2O or αGa_2O_3[1]. There are four additional modifications of the trioxide which are formed only under unusual conditions. Several approaches are available which one hopes might succeed in producing a gallium surface free of oxide. Our samples are prepared in a syringe under alcohol containing HCl which dissolves gallium oxides. The gallium is squeezed out into a shallow cup to form the sessile drop under an atmosphere of flowing nitrogen or helium. Although gross oxides are removed by the acid, a thin oxide film undoubtedly remains after this procedure. Observations supporting this will be discussed later in connection with the Auger work. Once the sessile drop is formed in the vacuum system, it may be cleaned further by heating. This desorbs weakly bound gases and, at around 500 °C, decomposes the trioxide to the suboxide according to the following reaction:

$$Ga_3O_3 + 4Ga \rightleftharpoons 3Ga_2O$$
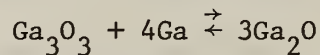
The suboxide has a high vapor pressure and is deposited on the walls of the vacuum system. This reaction, however, does not go to completion as shown by x-ray diffraction measurements[1]. Alternatively, the surface oxide can be reduced by heating in hydrogen by the following reactions:

$$Ga_2O_3 + 2H_2 \rightleftharpoons Ga_2O + 2H_2O$$

$$Ga_2O + H_2 \rightleftharpoons 2Ga + H_2O$$
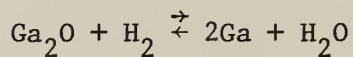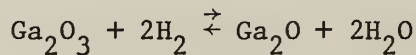
We have used both of these approaches in attempts to produce clean surfaces. A third possibility for cleaning the surface is ionic sputtering. We will discuss this technique in connection with our Auger work. This alternative is very attractive because it can be carried out at low temperatures, thus minimizing the diffusion of gases and other impurities from the cup into

the gallium and any reaction of the gallium with the cup or residual gases.

A detailed discussion of the apparatus and techniques used in this work is contained in last year's report[2]. Rather than repeat this, we will simply note that the gallium drops are contained in cups of various materials in an ion pumped vacuum system capable of reaching the 10^{-10} torr range. The optics and film used in the measurements have a resolution which permits the surface tension to be measured over the profile of the drop with a precision of about 0.5% using the Bashforth and Adams technique. This was verified last year with a computer program which fitted the entire measured profile to calculated solutions of the Young-Laplace equation. Thus we have some confidence in the measurements themselves. Additional experimental details will be given when necessary with the presentation of the data.

Surface Tension Measurements

The initial surface tension measurements used quartz cups to contain the sessile drops. Fig. 1 reproduces data shown in last year's report. Although the surface tension appears to decrease linearly with temperature above 120 °C, there is a maximum in the curve at that temperature. This kind of behavior is usually interpreted as evidence of impurity segregation which builds up at low temperatures because desorption is too slow to keep the surface clean. This seemed to be a reasonable explanation because hours were required to cool the drop to this temperature range after the initial high temperature bake, a time sufficient to adsorb many monolayers of gas from the residual atmosphere of the vacuum system which was at a pressure of 10^{-8} torr.

Analysis of subsequent measurements proved this adsorption explanation to be wrong in that the impurity did not originate in the residual gases in the vacuum system. When the drop was heated for twenty hours at 570 °C and then cooled, the data shown as open circles were obtained. The lengthy heat treatment enhanced the low temperature depression of the surface tension and moved the maximum in the data to a higher temperature. An additional twenty hour heat treatment lowered the surface tension even more dramatically as shown by the open boxes. The vacuum level during these measurements was about 10^{-8} torr. In subsequent experiments on other drops the entire vacuum system was baked and the pressure was in the mid 10^{-10} torr range. Measurements at this lower pressure confirmed the behavior shown in Fig. 1, suggesting the residual gases were not the adsorbed species.

This observation that the temperature and heating time control the behavior at lower temperatures indicates a contamination of the sample by the crucible at high temperatures. Although gallium is known to attack quartz at temperatures over 1000 °C[3], it was thought to be non-reactive at the maximum temperatures used in our experiments. It is possible, however, that the contamination does not come about from gallium dissolving the crucible but rather from gases or other components of the crucible diffusing into the gallium. Alternatively, the silica glass tube forming the vacuum jacket could release gases during bakeout which react at the gallium surface. A likely candidate for this would be water which is the primary constitutent desorbed from quartz at 600 °C[4]. Thus a possible reaction taking place might be the following:

$$2Ga + H_2O \overset{\rightarrow}{\leftarrow} Ga_2O + H_2$$
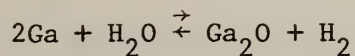
Another possibility for contamination exists, however. Silicon contamination of gallium in quartz containers has been studied in connection with the growth of GaAs[4].

Support for the oxide contamination hypothesis is shown in Fig. 2. This sample was loaded into the cup as a solid under high vacuum conditions in an attempt to avoid adsorbed gases at the quartz-gallium interface. The gallium was frozen under alcohol in the form of a cylindrical ingot with a thin rhenium wire along the axis. The rhenium wire was attached to iron slugs which could be moved magnetically through the silica wall of the vacuum system. With this solid loading technique, the cup could be baked at high temperature and the gallium loaded into it without breaking vacuum and back filling with an inert gas, a procedure which undoubtedly results in some oxygen and water adsorption on the quartz cup. When this procedure was followed and the gallium subsequently heated to 760 °C for twenty-four hours, the surface tension varied with temperature as shown by the solid points in Figure 2; a very strong surface tension depression at low temperatures with a maximum at about 300 °C. This behavior resembles that shown in Fig. 1. Hydrogen gas was then admitted to the tube through a liquid nitrogen cooled trap to about atmospheric pressure. When the gallium was heated to 550 °C for 30 minutes, the surface tension at low temperatures increased dramatically and effectively removed the maximum in the curve. These data are shown as open circles in Fig. 2 and suggest that an oxide at the surface is being reduced by heating in hydrogen, the second cleaning procedure mentioned in the Introduction.

The surface oxides in this experiment may not have been identical to those formed with the drop of Fig. 1 because of the different procedures used to form the sessile drop. There was probably a heavy oxide layer present when the gallium was loaded as a solid because the ingot was exposed to air during transfer to the vacuum system. Larger surface tension depressions were found at low temperature in this case than when the liquid loading procedure was used. This high concentration of oxide may have led to silicon contamination of the gallium by dissolving the quartz during the extensive high temperature bake.

A third experiment was performed in the quartz cup. Prior to forming the sessile drop the system was evacuated and the cup and adjacent tube baked at 900 °C for eighteen hours in an attempt to thoroughly eliminate water. The gallium was then added to the cup as a liquid and the system evacuated to the 10^{-8} torr range. After heating the gallium to about 100 °C to desorb weakly bound gases, hydrogen was admitted to the tube through a copper coil immersed in liquid N_2. Heating to progressively higher temperatures for periods of about 30 minutes and then cooling to the melting point and measuring the surface tension established that significant cleaning of the surface occurred at temperatures as low as 316 °C. After 30 minutes at 460 °C, the low temperature depression of the surface tension was found below 50 °C and was so slight it could not positively be separated from measurement imprecision, i.e., it was about 7 mJ/m^2, which is 1% of the surface tension. The gallium was then heated to 550 °C for fifteen minutes and photographed. The surface tension was measured after equilibration

at a number of lower temperatures. These data are shown as filled circles in Fig. 3. We also show as filled squares the results obtained after heating to 600 °C for eighteen hours. This hotter and longer heat treatment seems to have raised the surface tension at the melting point, but the change is only 2 mJ/m^2, well within the normal measurement imprecision. The general agreement of the two sets of data is good.

We see, therefore, that prolonged heating in hydrogen with the quartz cup seems to have little effect on the surface tension at lower temperatures in contrast to the behavior in the vacuum experiments typified in Fig. 1. Moreover, the surface tension now varies monotonically with temperature; there is no identifiable relative maximum in the data. The temperature variation, however, does not seem to be linear. The departure from linearity could be caused by impurities in the hydrogen gas being adsorbed at low temperatures. An increase in surface tension of 1% to about 718 mJ/m^2 at the melting point would effectively linearize the data.

After the measurements described above, the system was evacuated. When the pressure had dropped to the high 10^{-8} torr range, the gallium was heated for about 15 hours at 550 °C. A subsequent measurement of surface tension as a function of temperature produced the data plotted as open triangles in Fig. 3. The surface tension has been reduced significantly, but the variation with temperature is still monotonic. This is quite different from the results cited earlier and illustrated in Fig. 1. It is not clear whether the change has been brought about by the extended high temperature treatment prior to forming the drop or by initially heating in hydrogen rather than vacuum. The results using quartz cups seem to be very dependent on the history of the sample; i.e., the atmosphere and previous

11

heat treatment. Although the results in hydrogen are encouraging, the depression of surface tension with heating in vacuum indicates a container reaction which raises questions about the sample purity in all of the experiments. Presumably the contaminant is an oxide which is reduced by the hydrogen, but there may be an associated silicon contaminant also playing a role.

The ambiguous results with quartz led us to try a number of other cup materials. Sessile drop experiments were performed in cups of alumina, boron nitride, and two types of graphite. For the most part these materials were inferior to the quartz. Cups of high purity, pyrolitic graphite, however, gave more reproducible and consistent results than the other materials. A series of measurements were made under a variety of conditions in one of these graphite cups in an attempt to see if the surface tension changed systematically with heat treatment and atmosphere. To eliminate considerations of changing drop sizes and cup orientations or uncontrollable differences in the gallium introduced during preparation, all of the data we will show have been taken with the same drop. These results, however, are reproducible from drop to drop.

After the drop was formed using the liquid loading technique, the system pressure quickly reached the low 10^{-7} torr region. The drop was heated overnight to about 85 °C to desorb weakly attached gases. The surface tension was under 600 mJ/m^2 at this temperature afterwards indicating no significant cleaning of the surface had occurred. The temperature was then raised to 185 °C for two hours, the pressure in the system being about 10^{-7} torr. When the drop was cooled to the melting point, the surface

12

tension was measured to be 696 mJ/m^2 indicating a substantial cleaning of

the surface had been achieved. Subsequent heating for short periods to

progressively higher temperatures slightly increased the melting point

surface tension. Fig. 4 shows that the temperature variation of the

surface tension after heating to 465 °C is approximately linear with no

evidence of a maximum. The vacuum level during these measurements was

about 2 x 10^{-8} torr. Subsequently the drop was heated to 565 °C for

eighteen hours with the results shown in Fig. 5. These results do not

differ significantly from those shown in Fig. 4. The important fact is

that the measured surface tension has not been changed with a prolonged

high temperature bake, in contrast to the results with quartz cups in

similar vacuums.

After these measurements hydrogen was admitted to the vacuum system in

the normal manner and the temperature was raised briefly to 550 °C. This

produced no significant changes from the data of Fig. 5. An overnight

heating to 600 °C produced the results shown in Fig. 6. Again, there does

not seem to be any significant change from the results in vacuum shown in

Fig. 5.

A direct comparison of the data obtained after prolonged high temperature

heating with graphite cups in vacuum and hydrogen and with quartz cups in

hydrogen is made in Fig. 7. We have simply plotted the data shown in Figs.

3, 5, and 6 on one graph; no adjustment or normalization has been used. As

is evident, the measurements are in agreement and suggest that the surface

tension of gallium does not vary linearly with temperature. A least squares

non-linear fit to an equation of the form

$$\gamma = a - b\,(T-29.87) - c\,(T-29.87)^2$$

gave final parameter estimates of

$$a = 709.92 \ (.57)$$
$$b = -.160275 \times 10^{-2} \ (.5311 \times 10^{-2})$$
$$c = .923122 \times 10^{-4} \ (.9474 \times 10^{-5})$$

where the numbers in parentheses are the approximate standard deviations. For b the standard deviation is larger than the estimate of the parameter indicating that this coefficient is negligible. Thus, the dependence is essentially quadratic.

The general agreement of the vacuum and hydrogen measurements in graphite with the hydrogen measurements in quartz reinforces our feeling that gallium picks up an oxide impurity when it is heated to high temperature in quartz. This oxide presumably is effectively reduced in hydrogen but in vacuum it segregates at the surface and depresses the surface tension at low temperatures. A superposition of Fig. 1 on Fig. 7, however, reveals an additional complication. Although the high temperature data of Figs. 1 and 7 superpose nicely, at and below 200 °C, the surface tension in the quartz cup in vacuum rises above the data of Fig. 7. The maximum of Fig. 1 which occurs at about 150 °C is about 6 mJ/m^2 higher than the curve of Fig. 7. This is not a large discrepancy but a reexamination of the original data indicates that it is real. It may result from the fact that gallium oxides seem to form in patches rather than in a uniform surface layer. Thus, it is possible that the surface is no longer strictly described by the Young-Laplace equation and the Bashforth and Adams analysis is invalid.

Auger Spectrometer Experiments

As mentioned previously, the lack of any independent characterization of the surface is a serious problem in surface tension measurements. A number of modern surface analysis techniques are available which might fill this need, but they have been applied infrequently to liquids. The high vapor pressure of most liquids, of course, reduces the range of materials which can be studied. Nevertheless, the complementary use of these techniques with surface tension measurements seems feasible for some liquids and such studies are being attempted by several groups.

Liquid gallium is compatible with high vacuum instruments because of its low vapor pressure and melting point. It melts near 30 °C and the vapor pressure is about 10^{-6} torr at 700 °C so that a large temperature range is usable. We have been studying liquid and solid gallium in an Auger spectrometer. Our specimens are in the form of sessile drops and are contained in cups of graphite or rhenium which can be heated to over 500 °C and cooled to low temperatures. The drops are formed using the liquid loading technique described previously. The geometry of the spectrometer is not ideal for these measurements because the drops must be positioned well off the axis of the bell jar in order to be within working range of the horizontal cylindrical mirror analyzer. This makes simultaneous Auger analysis of the surface and photography of the drop profile impossible. Furthermore, the cup cannot be precisely aligned with the horizontal. Thus surface tension measurements in the present spectrometer are less accurate than those we have been discussing.

Although the surface of the drop during Auger analysis is difficult to observe visually, a video image can be obtained by a technique similar to that

15

used in scanning electron microscopy (SEM). A primary electron beam is rastered over the surface of the specimen and the local change in secondary electron emission is used to intensity modulate a video monitor in synchronization with the two-dimensional position of the electron beam. This imaging mechanism reveals surface features which are difficult to see optically. Although the video images do not have high contrast or resolution, they provide valuable information about the surface. Furthermore, the video imaging permits the sample orientation to be adjusted so that selected regions may be analysed with the Auger spectrometer. The instrument is equipped with an ion gun and a gas handling system so that the sample surface can be sputtered. In addition, a quadrupole mass spectrometer permits residual gas analysis. The pumping is provided by liquid nitrogen cooled sorption pumps and ion pumps so that the system is oil free.

After forming the sessile drop in the cup and evacuating the system to the low 10^{-9} torr region, an Auger spectrum of the surface has intense oxygen and carbon lines as seen in Fig. 8. Although the video image of the drop is uniform and featureless as would be expected of a liquid, the surface is actually solid. If the electron gun is left on for a number of hours, a dark rectangular spot develops where the beam has been rastered over the surface which persists unchanged and stationary after the beam is turned off. The amplitude of the Auger lines vary differently over this dark region, oxygen decreasing and carbon increasing as the beam is moved from the center of the raster area to an unbombarded area. This does not necessarily mean that the concentration of these constitutents is varying in the same way because the Auger line intensities of different elements are interrelated.

The loading technique, therefore, produces a sessile drop with a solid oxide surface layer containing significant concentrations of carbon. Our experience with the surface tension measurements suggested this layer might be decomposed and desorbed by heating to a moderate temperature. The effect of heat treatment on the gallium surface was examined by heating the drop briefly to progressively higher temperatures, then cooling and taking Auger spectra. After heating to 250 °C for five minutes, the oxygen line was halved and the carbon line was also reduced somewhat. However, the surface was no longer uniform and featureless. A "white" streak (as seen on the video picture) developed which gave Auger lines for oxygen and carbon at least twice the amplitude of the adjacent, featureless surface. Thus it appears that the thermal decomposition and desorption of the surface layer is not uniform, or that segregation and growth may occur during the heating and cooling procedure. The surface of the drop after heating is, of course, no longer solid and flows can develop. As the drop cools a phenomena is seen which we do not yet fully understand. The drop surface is initially featureless after heating to 400 °C. On cooling to about 120 °C, however, small black spots appear near the apex of the drop and move down the side collecting into a broad band on the surface above the cup edge. An Auger spectrum of the deposit shows carbon but no noxygen. This process was observed in both rhenium and graphite cups. The Auger spectra of areas of the surface without precipitates have oxygen and carbon lines which have diminished to the point at which they are indistinguishable from the noise. Concurrently the gallium lines become more intense.

Other experiments have shown that heating to 200 °C for several hours produces a surface which is clean except for the precipitates described above. The surface of the precipitates remains clean for long periods; no oxygen or carbon was detected after twenty-four hours at a pressure of 6 x 10^{-8} torr. Exposure to the residual atmosphere for a number of days produced a significant carbon line and a somewhat smaller oxygen line. This is to be expected because CO is an important residual gas in the vacuum system presumably because of the hot filaments in the ionization gauge.

In addition to carbon and oxygen the measurements in the vitreous graphite cup found some precipitates with a high sulfur content. An Auger analysis of the cup wall also found some sulfur. We suspect that the sulfur was introduced in a grinding procedure used on the cup during modification. A more stringent cup cleaning procedure eliminated or greatly reduced sulfur indications in later experiments. Several precipitates on one drop gave strong lead lines.

Another surface cleaning procedure we have tried is ionic sputtering. Within ten seconds of the initiation of sputtering with 2.5 keV argon ions, the uniform, solid surface film breaks up into large islands which move and rotate about the bombardment area. These islands shrink in the ion beam and eventually, when the surface is sufficiently clean, fluid flow develops which brings small islands from the rest of the drop to the site of sputtering. When the ion beam is turned off, the motion of the islands abruptly halts. With continued sputtering, the number and size of the islands decreases. Eventually the flow slows and stops with a few residual islands resting near the cup edge below the ion beam impact area. An Auger spectrum of the surface

after sputtering for several hours is shown in Fig. 9. This is identical to the result found after thermal cleaning and shows no carbon or oxygen. The same spectrum is obtained if the gallium is frozen and sputtered further.

Although there are other explanations for the processes seen on the surface during sputtering, the generation of fluid flow by surface tension gradients comes immediately to mind. In this model the sputtering produces and maintains a clean area of high surface tension. If adjacent areas have a lower surface tension because of adsorption, a high surface tension gradient will exist about the periphery of the sputtering site. The tangential shear stress generated on the liquid surface by the gradient will set up a fluid flow on the surface which will be directed from the area of low surface tension into the area of high surface tension, i.e., into the sputtering site. Presumably this becomes a convection node with the surface flow entering the drop volume at that point. If the sputtering is interrupted, the surface quickly equilibrates and the flow stops. As the surface becomes cleaner, the gradient is reduced and the fluid flow disappears.

A surface cleaned by sputtering will apparently stay clean for days with no change in the Auger spectrum or any additional island formation. If, however, the gallium is heated briefly, on cooling a precipitation process occurs which is similar to the one described previously. Small dark islands appear and descend from the apex of the drop piling up in a belt of precipitates at the base. An Auger spectrum of these precipitates again shows a strong carbon line and no oxygen. Most of these precipitates disappear under ion sputtering within a minute which indicates they are

19

very thin. Repeated sputtering and heating seems to reduce their numbers, but it is not clear that they can be totally eliminated in this way.

Our understanding of these sputtering and precipitation phenomena is limited with major questions to resolve about the origin and evolution of carbon in the gallium. It does not seem likely that the carbon concentration can be only that originally adsorbed on the surface, probably as CO_2. We suspect a continuing source of contamination which is logically the graphite cup. Occasionally large and thick carbon islands have been seen which we feel must have originated in the cup. Thus it is possible that the cup surface is flaking off under repeated heating and cooling cycles. It does seem that there was significantly less carbon with rhenium cups. However, this work is very limited because the gallium drops tend to run out of rhenium cups probably because of good wetting. Some carbon is certainly due to long exposures to the residual gases in the vacuum system because it is uniformly present on the surface and not associated with a precipitate, at least before heating. It is possible that the sputtering does not effectively remove carbon from the system but just disperses it into the volume as very fine particles so that it is not seen. Heating then could lead to agglomeration and reappearance at the surface because of buoyancy and fluid flow.

As mentioned earlier we cannot make accurate surface tension measurements on the sessile drops in the Auger spectrometer because of geometric and alignment problems. We have, however, measured the surface tension of a drop which was sputtered for several hours and whose Auger spectrum indicated a clean surface. In order to make the measurement, the drop was repositioned in the Auger spectrometer after sputtering and analysis so

that its profile could be photographed in parallel light. The surface tension was about 700 mJ/m^2. Recognizing that this may be inaccurate, it seems unlikely that the error could be more than a few percent. It seems beyond possibility that the surface tension could be as high as 800 mJ/m^2, the anomously high values found previously in two instances[2]. A new spectrometer is being assembled which will permit accurate surface tension measurements and simultaneous Auger spectral analysis. We believe that it will permit a resolution to this discrepancy in previous measurements.

Discussion

The experiments with gallium in the Auger spectrometer have shown the primary surface impurities to be oxygen and carbon. A relatively low temperature heating in vacuum can clean the surface of oxygen but the carbon is either not effectively desorbed or is being resupplied, possibly from the crucible. The carbon after heating is contained in thin plates which collect on the drop surface near the cup edge. Thus the surface of the drop, although clean for the most part, will have regions in which it is not liquid. The entire drop shape in this case is not described precisely by the Young-Laplace equation. Because the precipitates collect at the base, however, the resultant distortion of the drop near the apex may be small. Thus the surface tension values calculated by the Bashforth and Adams technique above the drop maximum may not be seriously affected. Assuming such a precipitation phenomenon is also occurring in our sessile drop experiments, the fact that very nearly the same surface tension is calculated at various points on the drop in this region suggests the profile is not severely perturbed. We do not know, of course, that precipitation

is occurring in the sessile drop experiments. The cups are different forms of graphite from different sources in the two experiments; the Auger cup is "vitreous" graphite and the sessile drop cup is high purity pyrolitic graphite. Sessile drop measurements in a companion vitreous graphite cup indicated some surface tension depression at low temperatures, but it is difficult to compare the results because of variations in procedure in the two groups of measurements. The approximate agreement at the melting point of the surface tension values shown in Fig. 7 with that measured for a drop that was sputtered clean in the Auger spectrometer is additional evidence that the precipitates, if present, are not having much effect on the drop shape.

The sessile drop surface tension measurements and the measurements and observations in the Auger spectrometer demonstrate a strong sensitivity on cup material and heating history. Certainly quartz cups used at high temperatures in vacuum result in contamination of the gallium with what seems to be an oxide because of the ease with which it is reduced in hydrogen. The gallium may also be contaminated with silicon which has little effect on surface tension values presumably because of low concentration or no tendency for surface segregation.

The surface contamination by the residual gases in the vacuum system is much less significant than that originating in the cup. We have found in the sessile drop experiments that surface tension values at the melting point decline very slowly at vacuum levels of 10^{-8} to 10^{-7} torr. This is also true in the hydrogen atmospheres. The Auger measurements support this observation.

The general agreement of the surface tension values measured in graphite cups in vacuum and hydrogen with the values found in quartz cups in hydrogen is shown in Fig. 7. Although this is strong evidence the gallium surfaces are in a similar state for these three groups of measurements, it does not prove the surfaces are clean. The very limited measurements of surface tension on the one drop in the Auger spectrometer, however, gave surface tensions at the melting point which are only about 1% lower than those shown in Fig. 7. Given the probable error in these measurements, this is good agreement and suggests that the data of Fig. 7 are typical of a clean surface.

There are, however, unanswered questions and unresolved contradictions in the surface tension measurements. Fig. 1 is data taken in a quartz cup which shows a low temperature surface tension depression which we have interpreted as arising from surface segregation of an oxide contaminant. A comparison of this data with the compilation of data from "clean" surfaces in Fig. 7 shows a very good agreement at higher temperatures. However, between 250 °C and the melting point, the surface tensions in the oxide contaminated gallium of Fig. 1 rise above that for the clean gallium by as much as 6 mJ/m^2 at the maximum. We, therefore, have a contradiction: if surface segregation is producing the maximum in Fig. 1 by depressing the surface tension at low temperatures, how can the surface tension of the contaminated surface be higher than that of a clean surface? A possible resolution would be that an impurity is also active in the data of Fig. 7 and the curvature evident at low temperatures is due to adsorption. This impurity would necessarily be independent of cup material and atmosphere. Another hypothesis is that the impurities in the "contaminated" gallium

23

are confined to patches so that the drop shape is not being described by the Young-Laplace equation. We have no evidence supporting either of these speculations.

As mentioned in last year's report, there have been three previous measurements of the surface tension of gallium as a function of temperature. The functions suggested by the authors to describe their data are as follows:

$$\gamma_I = 708 - .0031(T-29.87) - .000067(T-29.87)^2 \text{ [5]}$$

$$\gamma_{II} = 706.7 - .000647(T-29.87) - .0000965(T-29.87)^2 \text{ [6]}$$

$$\gamma_{III} = 718.0 - .101(T-29.87) \text{ [7]}.$$

The non-linear least squares analysis of the data shown in Fig. 7 mentioned previously gave the relationship

$$\gamma = .709.9 + .0016(T-29.87) - .0000923(T-29.87)^2.$$

Note that our results and those described by the first two relations above differ at the melting point by no more than 3.2 mJ/m^2. Since small systematic errors must exist in all work, it is interesting to compare the various measurements by making them all coincide at one temperature. We do this in Fig. 10 where we have translated γ_I and γ_{II} to agree with Fig. 7 at the melting point. Our data is then seen to lie between the two curves over the entire temperature range. The differences in the data adjusted in this way is hardly more than the precision with which the measurements were made in our work except possibly at the high temperature end of the curve.

We also show the linear relationship γ_{III} (unadjusted). These measurements clearly disagree with the other data shown in Fig. 11. The

linearity of the surface tension values as a function of temperature in this work was cited as evidence that the gallium was cleaner than that used in the measurements showning non-linear behavior. However, at temperatures above 125 °C, the surface tension values in the linear data are lower than the non-linear data. At 360 °C, the highest temperature used, they find a surface tension value about 15 mJ/m^2 lower than the other results in Fig. 11. Thus it is hard to argue that the linear data represents a cleaner surface. This is the same problem discussed previously with respect to our own data and we cannot rationalize the contradiction. We note, however, that the gallium preparation used in this work involved heating to 1000 °C in a quartz ampoule. We suspect their gallium may have been contaminated with silicon. We do not know how this would have affected their surface tension values.

References

1. I. A. Sheka, I. S. Chans and T. T. Mityureav, <u>The Chemistry of Gallium</u>, Elsevier Publishing Co., New York, 1966.

2. S. C. Hardy and S. R. Coriell, <u>Properties of Electronic Materials</u>, NBSIR 79-1767, 1 (1979).

3. A. P. Thompson, <u>Rare Metals Handbook</u>, Second Edition, Edited by Clifford A. Hampel (Chapman & Hall Ltd., London, 1958) p. 178.

4. L. Ekstrom and L. R. Weisberg, J. Electro Chem. Soc. <u>109</u>, 321 (1962).

5. O. A. Timofeevicheva and P. P. Pugachevich, Dokl. A. Kad. Nan K. SSR, <u>134</u>, 840 (1960).

6. V. I. Nizhenko, L. P. Sklyarenko and B. N. Evemenko, Ukrain. Khim. Zhur. <u>6</u>, 550 (1965).

7. A. A. Karashaev, S. N. Zadumkin and A. I. Kukhno, Russ. J. of Phys. Chem. <u>41</u>, 329 (1967).
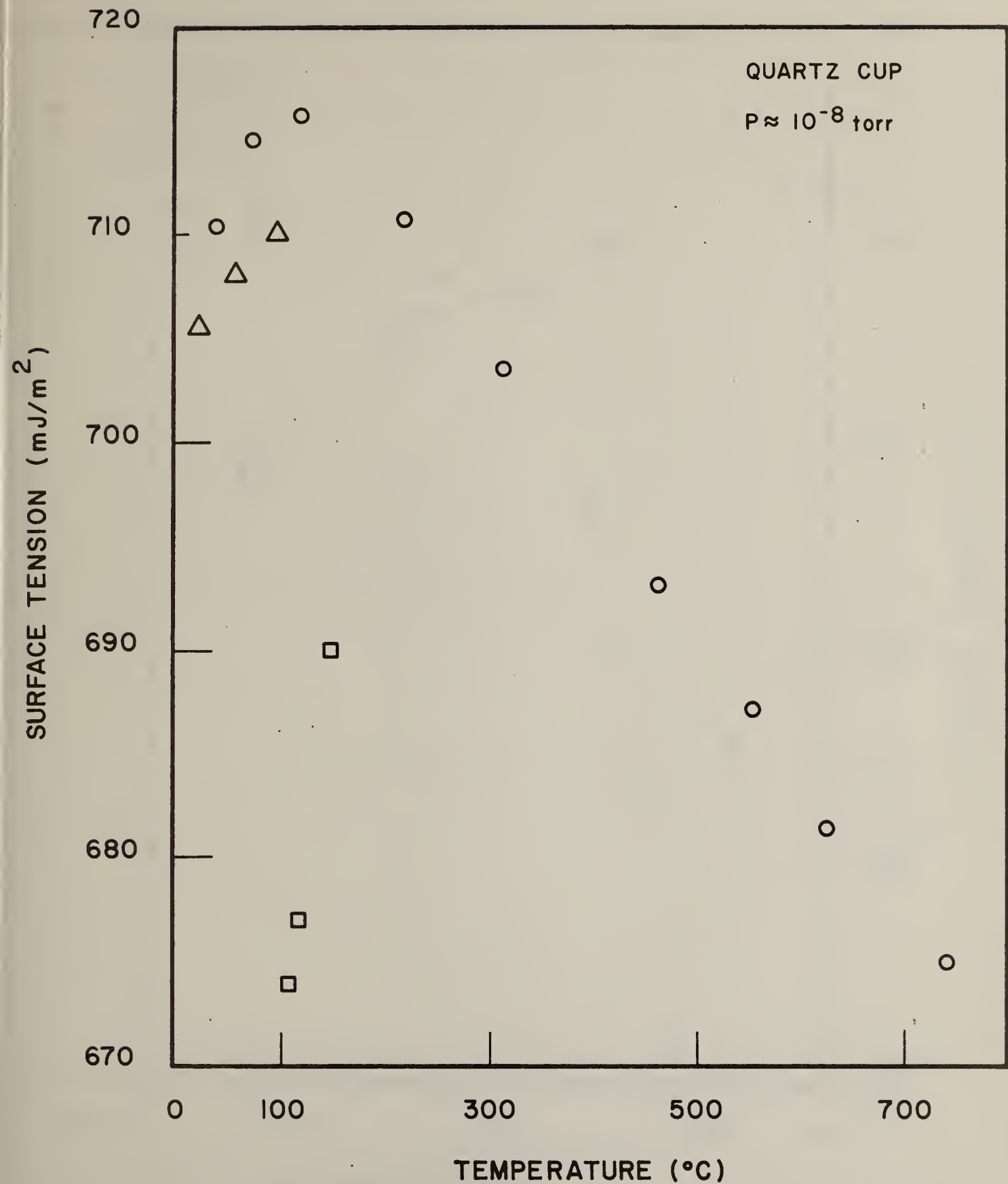
Fig. 1.   The surface tension of gallium as a function of temperature (quartz cup; sample heated in vacuum).
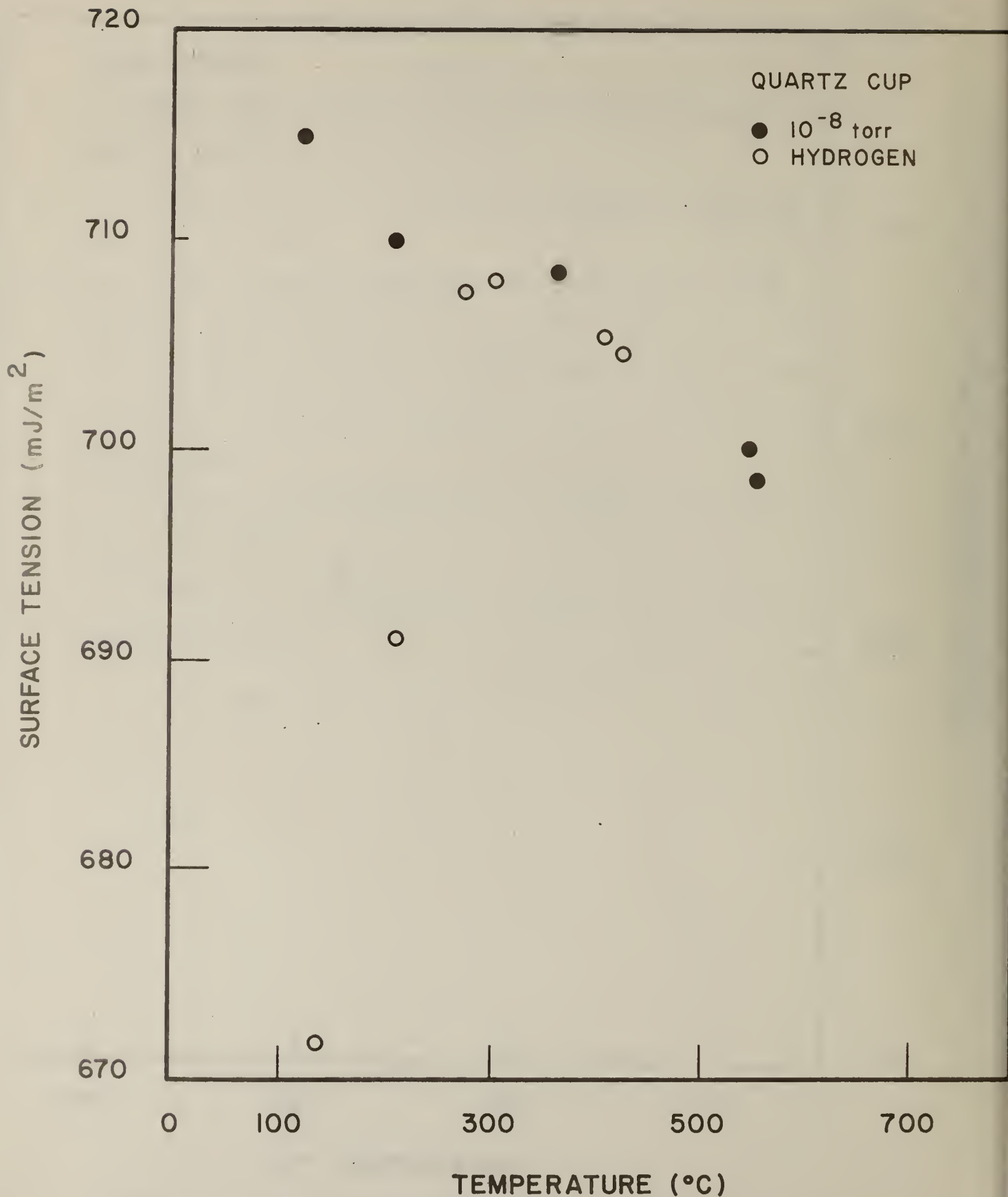
Fig. 2. The surface tension of gallium as a function of temperature (quartz cup; sample heated initially in vacuum, then in hydrogen).
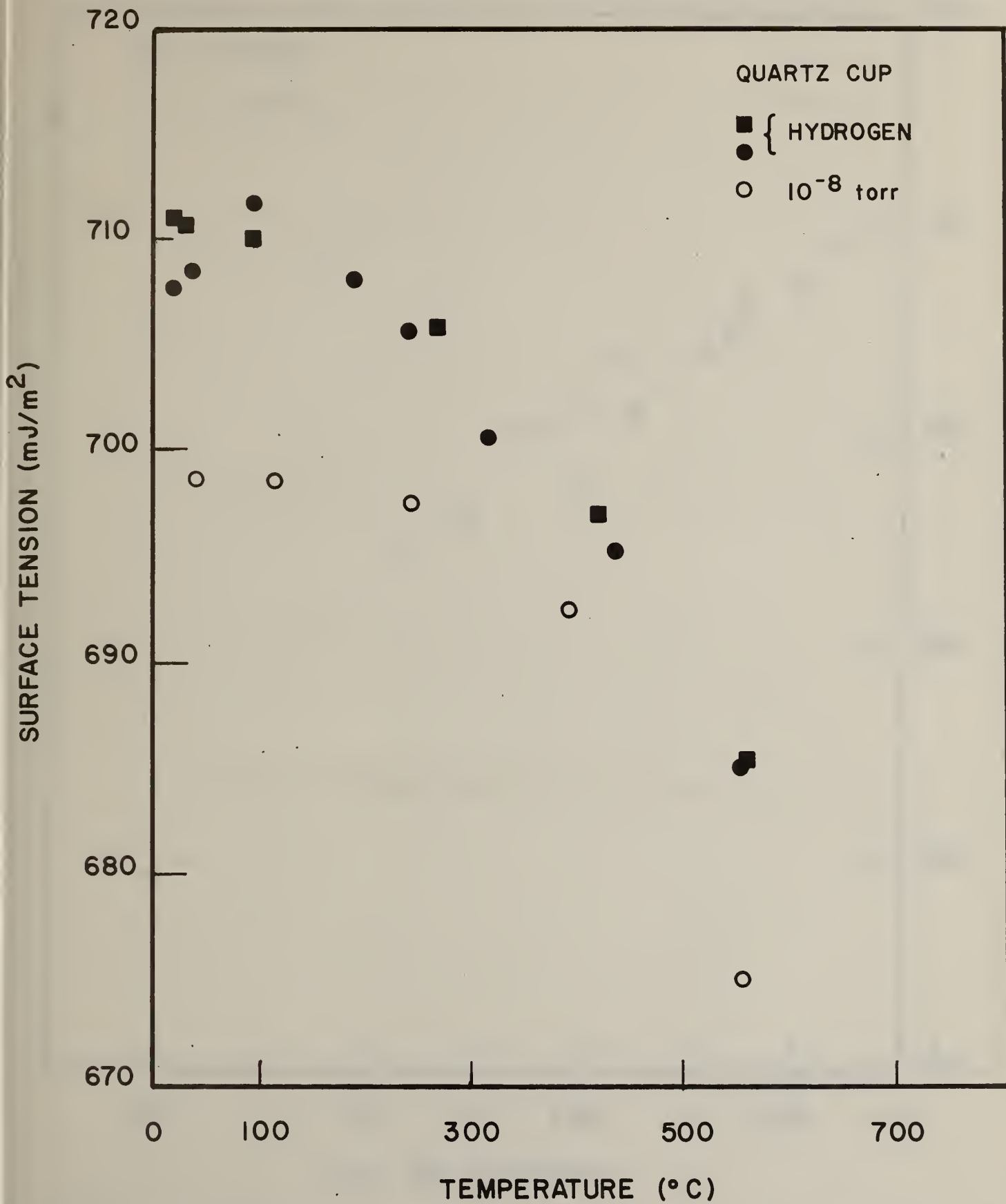
28

Fig. 3.   The surface tension of gallium as a function of temperature (quartz cup; sample heated initially in hydrogen, then in vacuum).
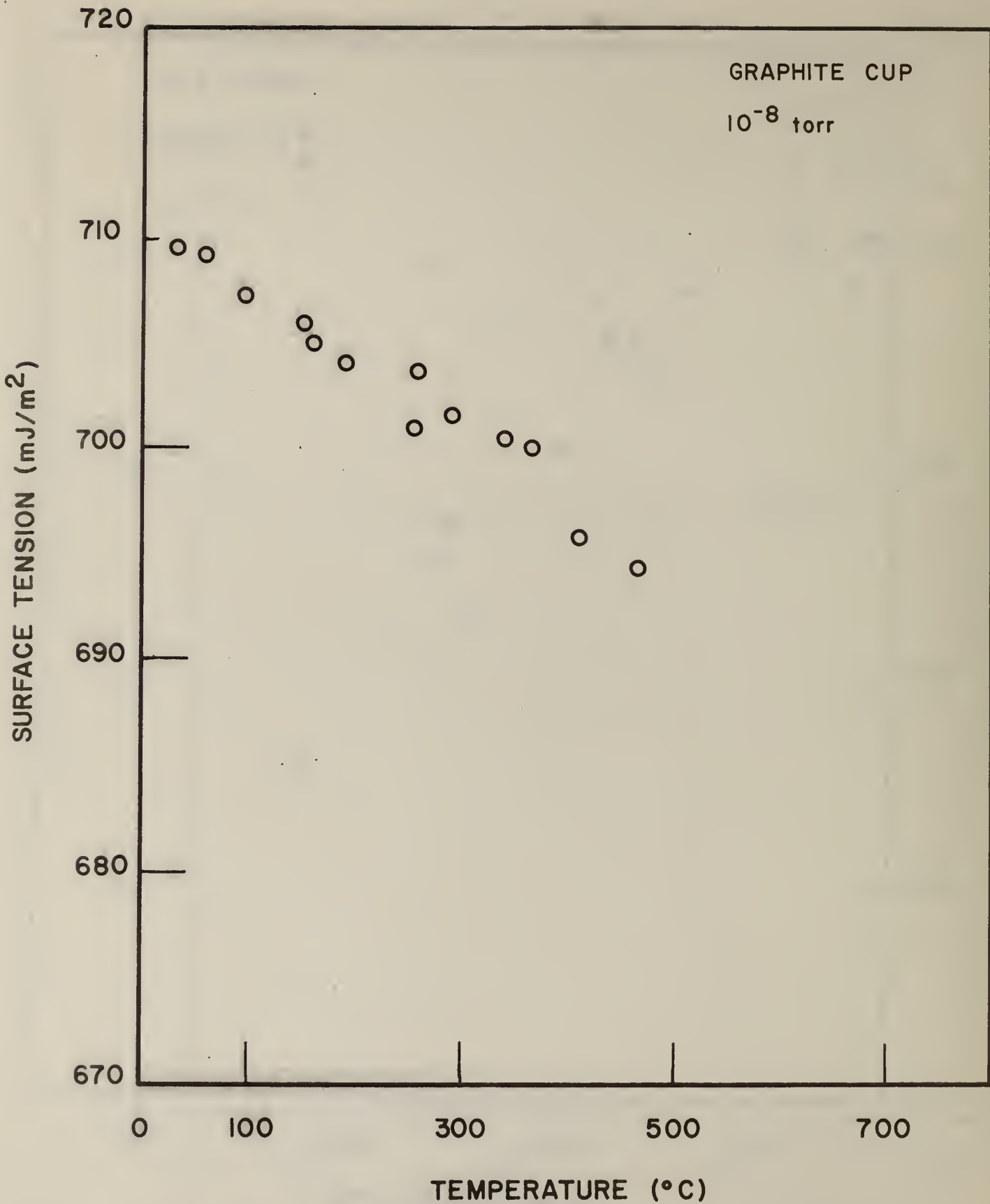
Fig. 4. The surface tension of gallium as a function of temperature (graphite cup; sample heated to 465 °C for 30 min. in vacuum).
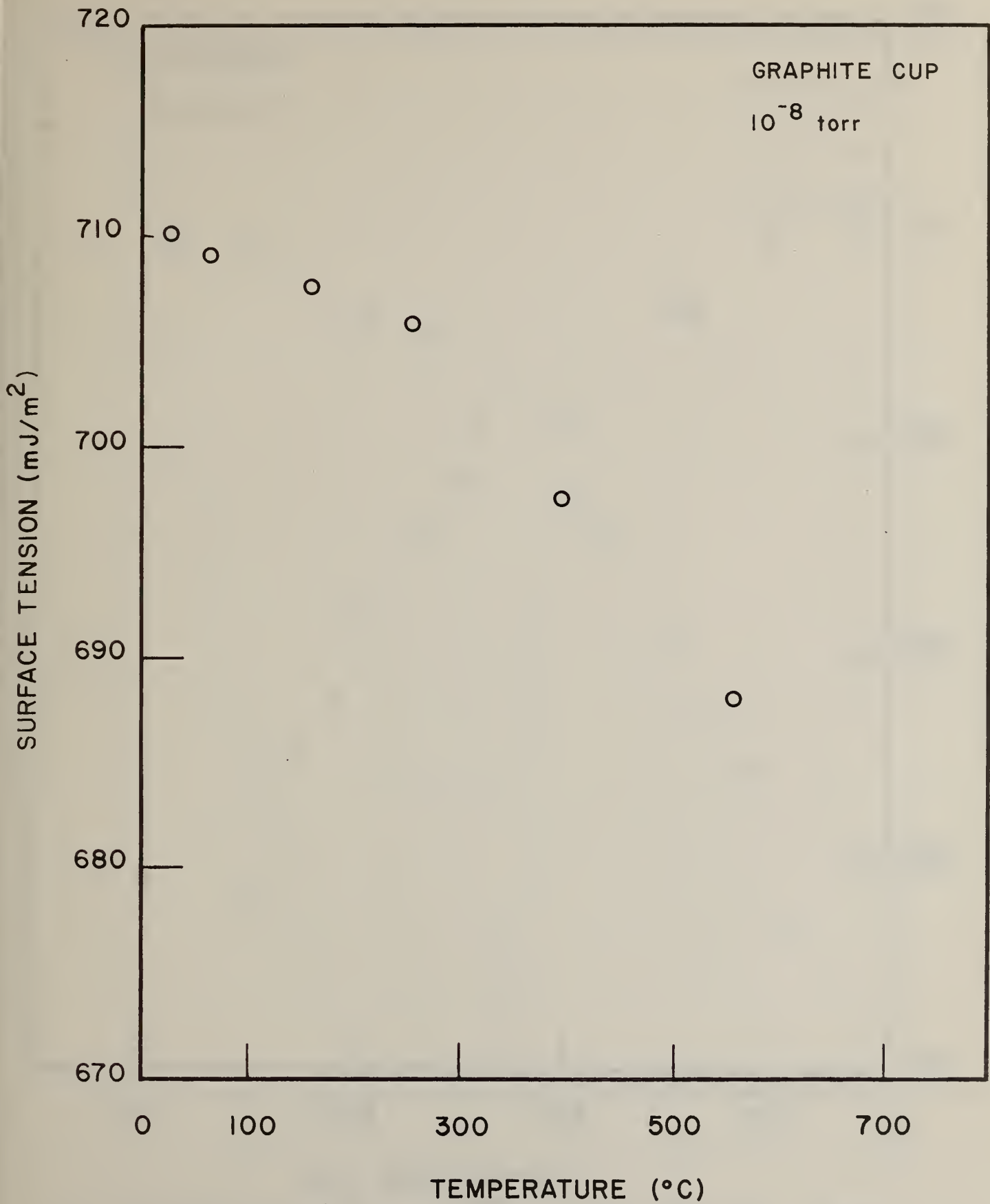
30

Fig. 5.   The surface tension of gallium as a function of temperature (same drop as Fig. 4; sample heated to 565 °C for 18 hours in vacuum).
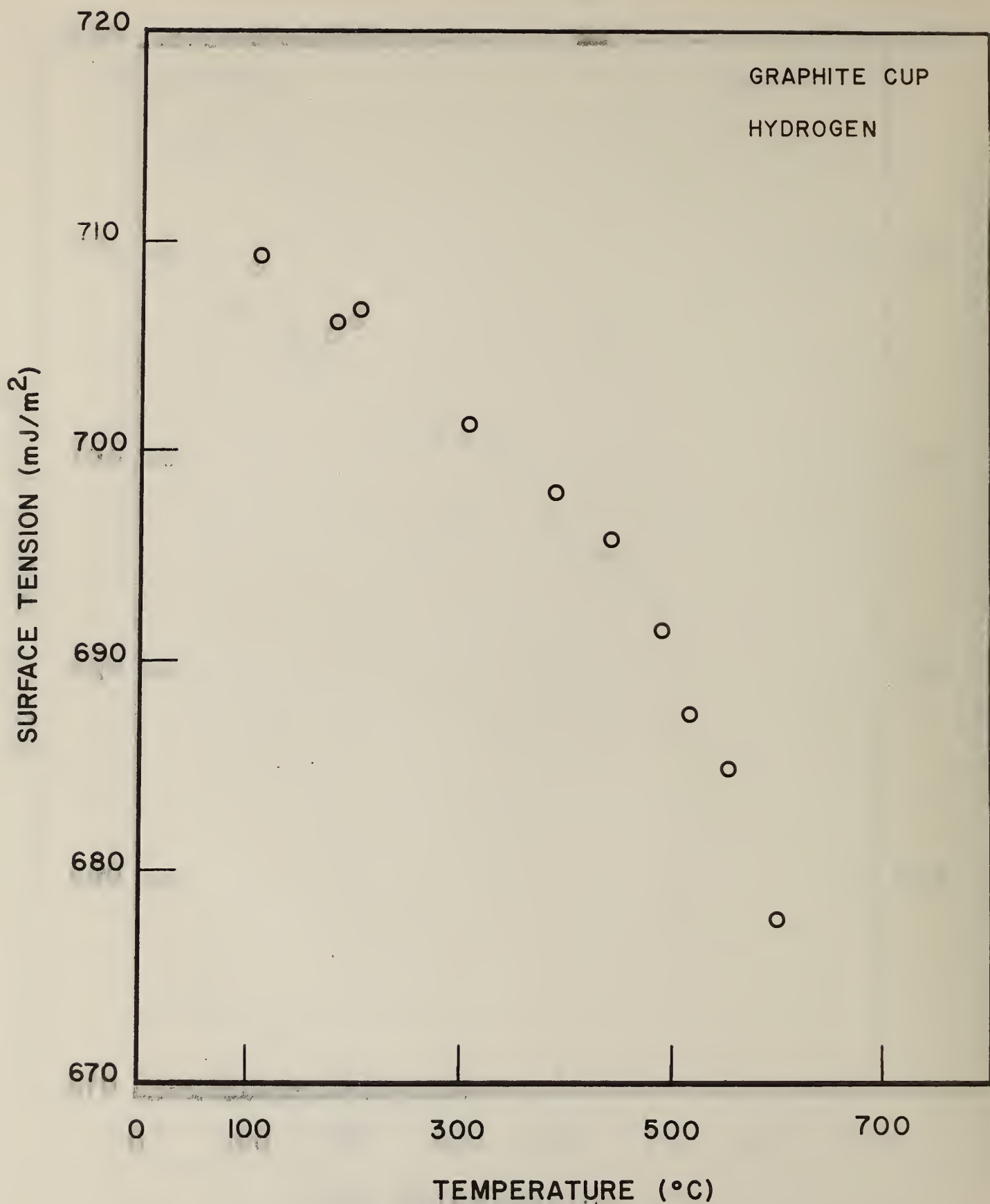
Fig. 6.   The surface tension of gallium as a function of temperature (same drop as Fig. 4; heated to 600 °C for 18 hours in hydrogen).

32
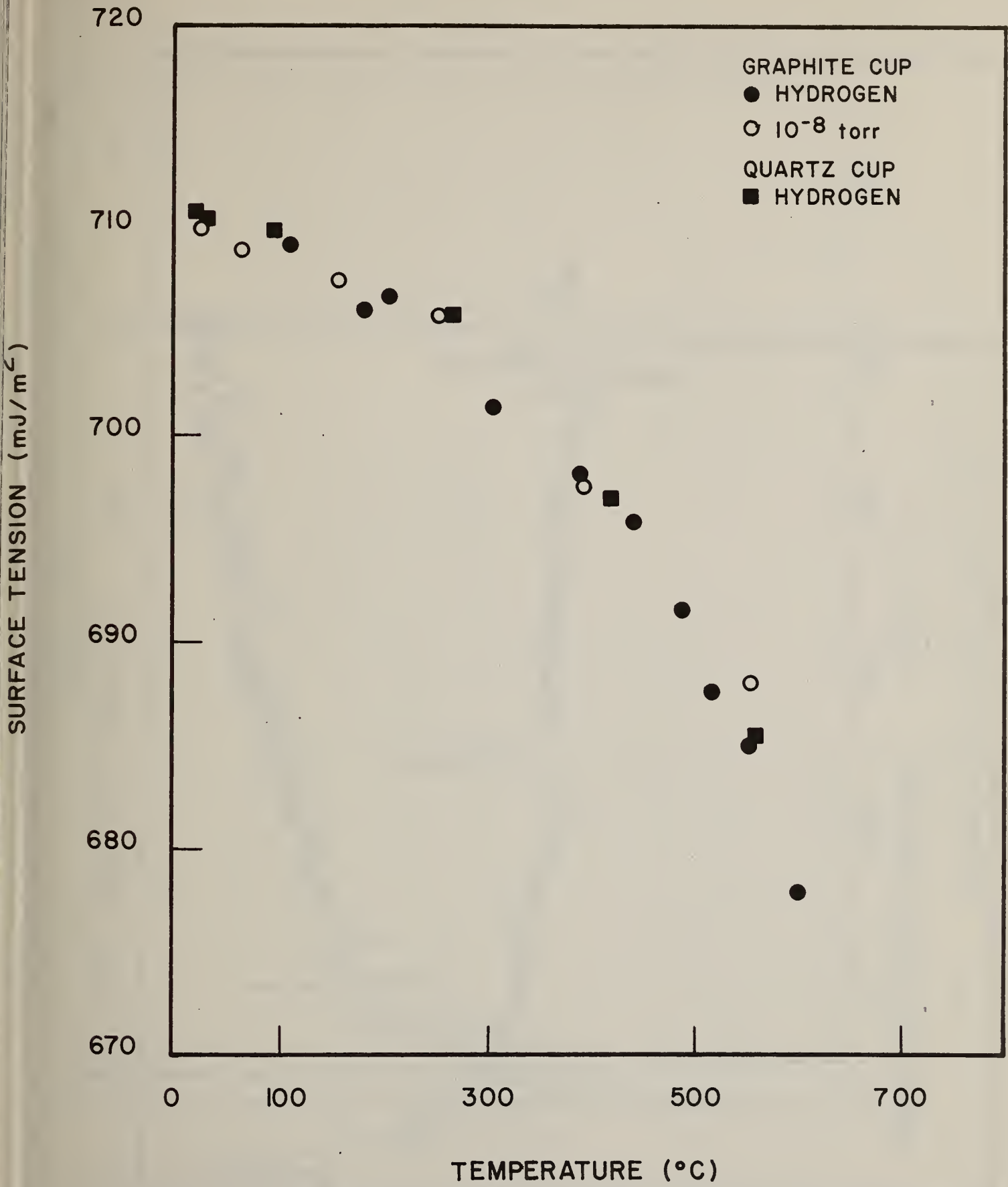
Fig. 7. The surface tension of gallium as a function of temperature (combination of Figs. 3, 5, and 6).

33

AUGER SPECTRUM OF GALLIUM
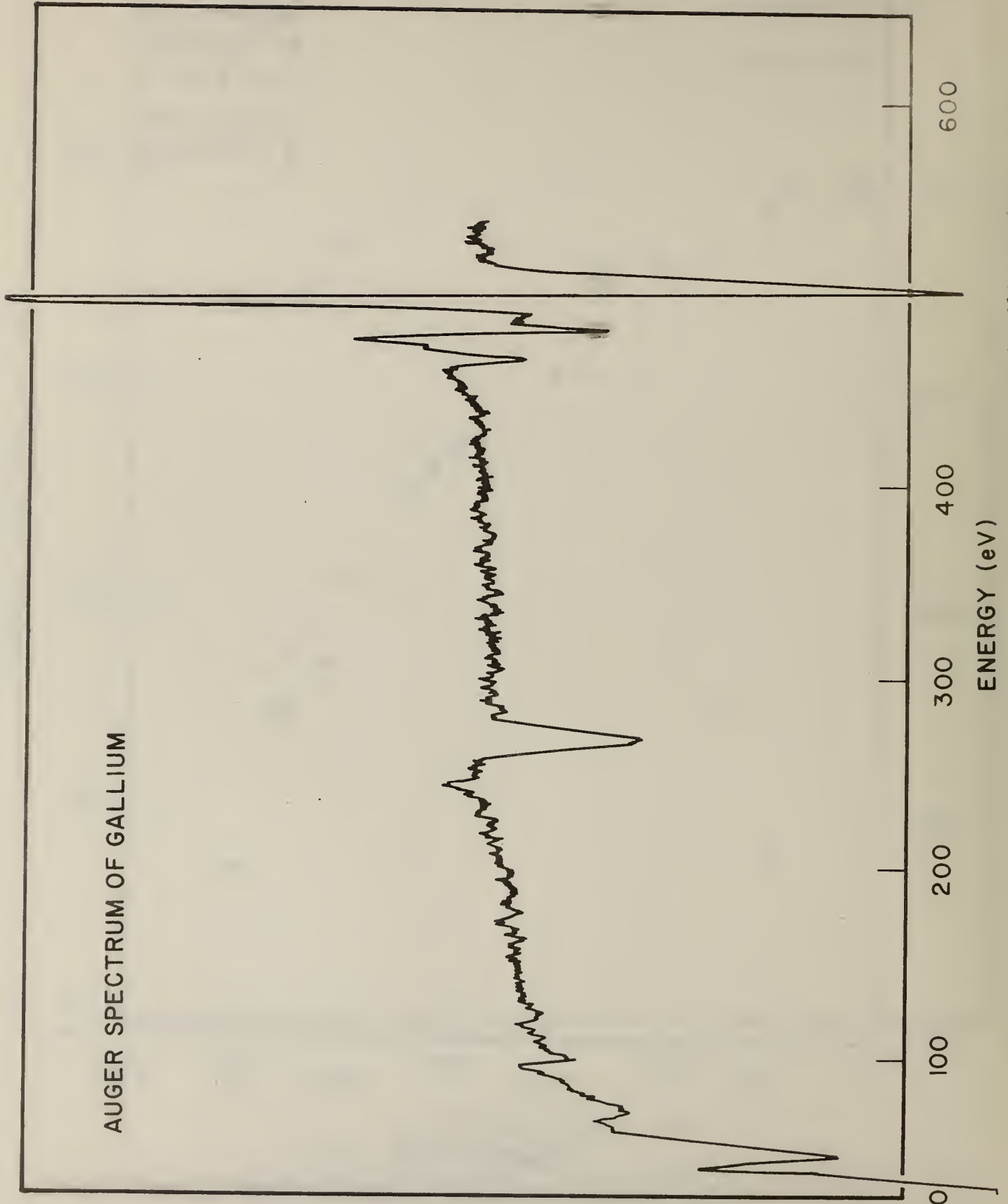
ENERGY (eV)

Fig. 8.   The Auger electron spectrum of an uncleaned liquid gallium surface.

AUGER SPECTRUM OF GALLIUM

ENERGY (eV)

Fig. 9.   The Auger electron spectrum of a liquid gallium surface which was
sputtered with 2.5 keV Argon ions for several hours.

Fig. 10. Comparison of the surface tension of gallium as a function of temperature found previously with this measurement.

36

Task 2

Solutal Convection During Directional Solidification

W. J. Boettinger, S. R. Coriell and F. S. Biancaniello
Metallurgy Division
Center for Materials Science

and

M. R. Cordes
Mathematical Analysis Division
Center for Applied Mathematics

Summary

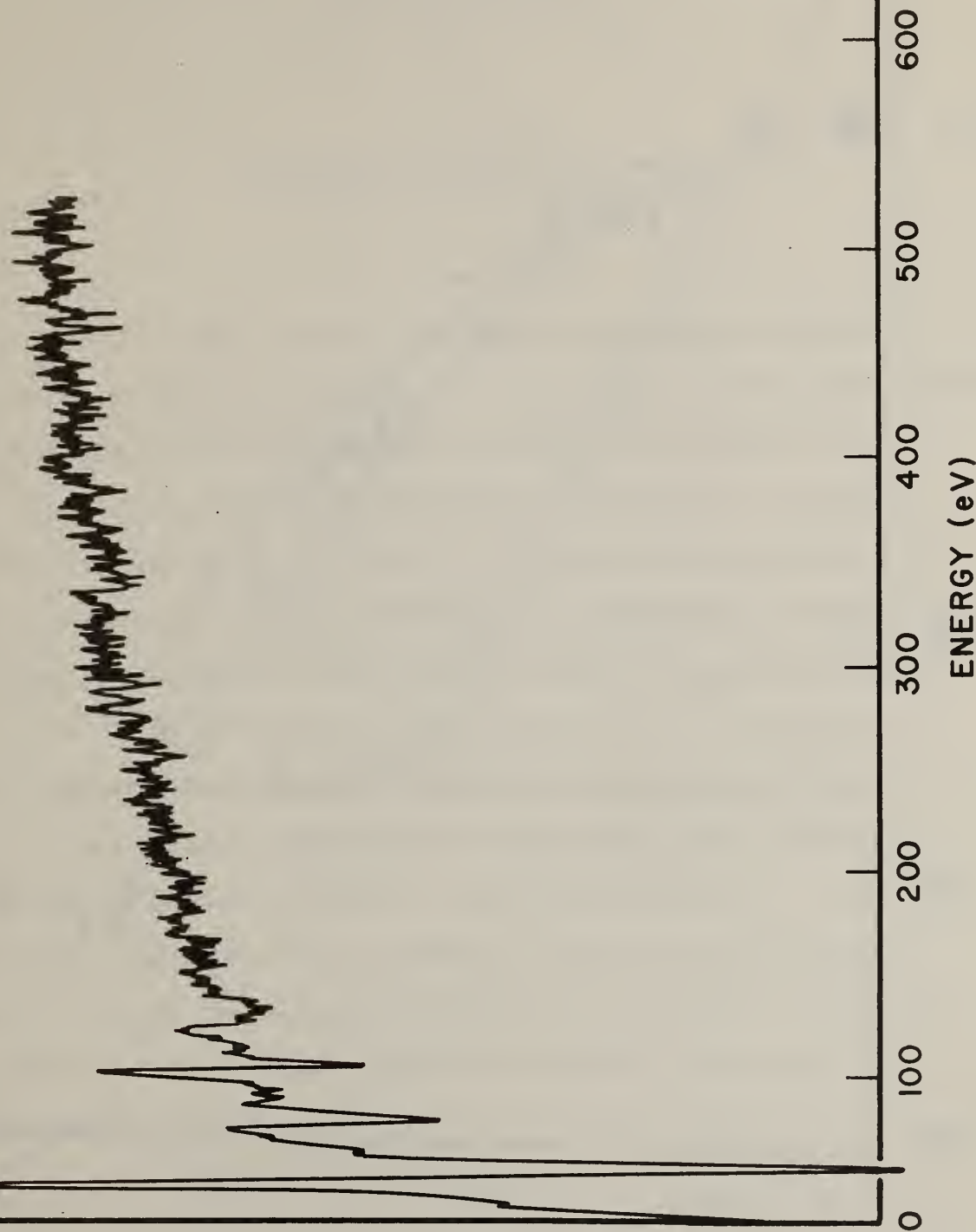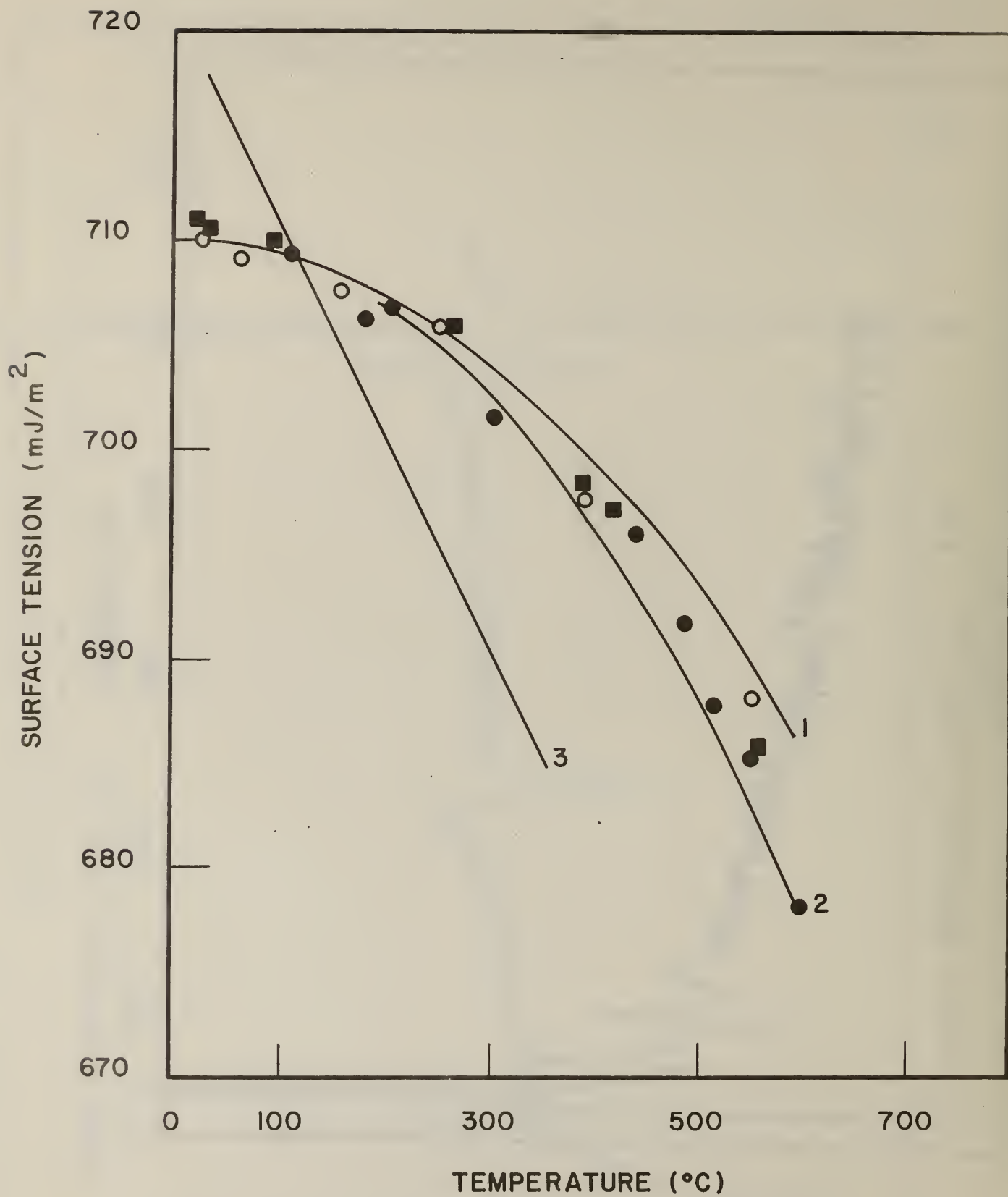The effect of solute gradient induced convection during vertical

solidification on the macrosegregation of Pb-rich Pb-Sn off-eutectic

alloys is determined experimentally as a function of composition and

growth rate. In many cases macrosegregation is sufficient to prevent the

plane front solidification of the alloy. The transition from dendritic to

composite structure is found to occur when the composition of the solid is

close enough to the eutectic composition to satisfy a stability criterion

based on G_L/V (liquid temperature gradient/growth rate). A vertical or

horizontal magnetic field of 0.1T (1 kilogauss) does not reduce macro-

segregation, but downward solidification (liquid below solid) virtually

eliminates macrosegregation in small (∿3 mm) diameter samples.

Additional calculations of the onset of convective and interfacial

instabilities during the directional solidification of lead-tin alloys have

been carried out with particular emphasis on constant gravitational

accelerations of 980 (10^{-6}) cm/s^2.

A. SOLUTAL CONVECTION INDUCED MACROSEGREGATION AND THE DENDRITIC TO COMPOSITE TRANSITION IN OFF-EUTECTIC ALLOYS

Introduction

The ability to solidify two-phase aligned structures from a wide range of compositions near a eutectic composition has importance in the full utilization of this class of composite materials. The early work of Mollard & Flemings[1] claimed that the range of compositions for which plane front composite growth was possible was restricted not only by constitutional supercooling requirements but also by the requirement that convection be avoided. In fact, their experimental work using vertical upward solidification was limited to the Sn-rich side of the Pb-Sn eutectic where the fluid density, influenced by temperature and composition, always decreases with distance from the interface (height). On the Pb-rich side of the eutectic, the concentration gradient in the liquid can cause the density to increase with distance near the interface and possibly cause convection (here termed solutal convection). Subsequently, it was argued[2,3] that as long as a stagnant boundary layer exists whose thickness is large compared to the eutectic spacing, plane front growth of the composite should be possible in the presence of convection. This was in fact verified by experiments[2,4,5] which demonstrated the growth of Pb-rich Pb-Sn composites. However, Verhoeven, Kingery and Hofer[6] subsequently showed that significant macrosegregation (10 w/o) down the length of solidified samples occurs in samples only 1 w/o on the Pb-rich side of the Pb-Sn eutectic, and attributed this macrosegregation to solutal convection.

The purpose of this research is to describe the microstructure and macrosegregation produced during upward solidification of off-eutectic alloys 2-5 w/o from the eutectic composition when the liquid density near

the interface _increases_ with distance from the interface and to determine if a magnetic field or solidification downward can eliminate solutal convection and hence macrosegregation.

Experimental Procedures

Alloys were prepared from 99.99% pure Sn and Pb in evacuated and sealed borosilicate crucibles. The directional solidification furnace is constructed of non-magnetic materials and has a bifilar wound cylindrical resistance heating element with upper and lower sections and a circulating water cooled chill zone. A 3 mm I.D. silica tube containing the desired alloy is pulled down through the chill, sealed by O-rings, at constant velocity to accomplish directional solidification. The cooling water comes directly in contact with the silica tube. Using two separate A.C. proportional temperature controllers for the furnace, and water cooled by a heat exchanger, temperatures are constant to 0.1 °C over an hour and 1 °C over several days. The vertical drive is powered by a synchronous motor with a multi-speed gear box. Speeds from 0.5 μm/s to 0.5 mm/s are possible. The tube is attached to the pull shaft using a device which permits the sample to be suddenly pulled down about 3 cm to quench the liquid-solid interface.

The value of the liquid temperature gradient measured for several typical experiments with 0.25 mm diameter sheathed thermocouples was 360 ± 10 K/cm. This value was assumed for all other experiments. The furnace is designed so that a permanent magnet with a pole diameter of 8 cm and a pole separation of 11 cm could be slid around the furnace to apply a 0.1T (1 kilogauss) horizontal magnetic field. Alternately, an 11 cm diameter solenoid could be placed over the furnace-chill to apply up to 0.1T vertical magnetic

field. Additionally the furnace could be inverted for solidification downward. In this case a fibrous ceramic plug was used to maintain a small upward pressure on the inverted melt to prevent separation of the liquid from the freezing solid.

A specific directional solidification experiment was conducted in the following manner. A tube filled with the desired alloy was inserted through the chill, with the alloy completely in the chill section. The tube was evacuated and the furnace temperature was equilibrated. The sample was then driven quickly into the furnace melting about 12 cm of alloy. The tube was backfilled with argon and temperatures were allowed to stabilize for about 1 minute. Excessive holding times at this stage are undesirable because a layer of Pb-rich solid solution will slowly solidify and disrupt the uniformity of the initial liquid composition. The tube was then pulled at the desired rate until about 6 cm had solidified. The remainder of the sample was then quenched, delineating the liquid-solid interface in the microstructure. The silica was removed with HF acid and the specimens were mounted in a cool-setting epoxy for characterization.

Samples were routinely examined in a longitudinal section (parallel to the solidification direction) using standard metallographic techniques. For each experiment the shape of the liquid-solid interface was examined to be certain that heat flow was unidirectional. In the present experiments, the macroscopic liquid-solid interface of two-phase composite growth, when achieved, was convex towards the liquid by only 10-20 μm across a 3 mm diameter sample.

Measurement of macrosegregation (average composition of the two-phase solid) along the length of solidified samples was performed using two methods,

x-ray fluorescence and a titration method. The former method, which was described previously[7], uses incident monochromatic (22.1 keV) x-rays collimated to 1/2 mm x 1/2 mm. The use of x-rays permits deeper penetration into the samples and hence better averaging over the two-phase structure than does the use of electron probe methods. This data was used to non-destructively evaluate the extent of macrosegregation and to indicate those samples for which the titration method would be used. The titration method[8] was performed on approximately 2 mm discs cut transverse to the growth direction. Accuracy of the titration method is approximately $\pm$ 0.25 w/o Pb.

Experimental Results

Results on the microstructure and macrosegregation of Pb-rich off-eutectic alloys solidified upward with and without magnetic field and downward are presented here and will be discussed in the next section. Directional solidification experiments were conducted vertically upward (liquid above the solid) on the Pb-rich side of the eutectic. In all cases, solidification begins with the dendritic growth of the Pb-rich phase even when the ratio of the temperature gradient G_L in the liquid to the growth velocity V substantially exceeds the requirement of constitutional super-cooling[1] for the bulk composition of the alloy. The volume fraction of dendrites decreases slowly as a function of distance as shown, for example, in Fig. 1, until the structure is a two-phase composite. The region of dendritic growth in most instances is very long compared to D/V (where D is the liquid interdiffusion coefficient) and does not correspond to an initial transient of the type described by Mollard and Flemings[1]. This long region of dendritic growth will be shown to be a manifestation of the macrosegregation which occurs in these alloys due to solutal convection.

41

Table I is a summary of these experiments showing the original composition (C_o), growth rate (V), G_L/V, D/V, the initial length of the liquid alloy (L), the length of the dendritic zone (Z^D), and the average solid compositions at three positions in the solidified samples: $C_s(0.0)$, $C_s(0.1)$ and C_s^D at 0.0, 0.1 fraction solidified and at the transition from dendritic to composite structure, respectively. Fraction solidified, f_s, is the ratio of distance solidified to the initial length of molten alloy. Other experiments conducted with an imposed magnetic field and with solidification downward are included in Table 1.

Fig. 2 shows the measured composition as a function of fraction solidified for five 43.0 w/o Pb alloys solidified at 0.5 µm/s. [The eutectic composition, C_E, is 38.1 w/o Pb.] Two samples were solidified upward without magnetic field with initial melt lengths of 5.2 cm and 11.8 cm respectively. The initial solid composition is very high in Pb content ∿ 72 w/o Pb (the boundary of the two phase field occurs at 81 w/o Pb), and falls to the vicinity of the eutectic composition as solidification proceeds. The fractions solidified f_s^D, at which the dendritic structure disappears in the two samples are essentially identical. Beyond this position the samples continue to solidify nondendritically as a two phase composite with changing composition until at a f_s ∿ 0.22 the rate of change of composition with distance decreases sharply. Because of the excellent agreement of the macrosegregation of these two samples as well as the dendrite disappearance position, it is apparent that fraction solidified is the proper variable to describe changes in composition. This strongly suggests that the dendritic zone is not caused by an initial transient but by macrosegregation. Henceforth, we will use fraction solidified as the length parameter to describe macrosegregation.

Also shown in Fig. 2 are two samples solidified upward with imposed
horizontal and vertical magnetic fields of 0.1T (1 kilogauss). The macro-
segregation and position of dendrite disappearance for these experiments are
similar to the samples solidified without magnetic field. The final sample
shown in Fig. 2 was solidified vertically downward (liquid below solid).
Here a significant reduction in the macrosegregation was observed. Except
for an initial transient (length ∿ 2 D/V) the composition is relatively
constant. [The slight decrease in composition is caused by thermal diffusion.]
Furthermore, the structure is completely two phase composite. There is no
initial region of dendritic growth.

The effect of a faster interface velocity (2.6 μm/s) on macrosegregation
for 43.0 w/o Pb alloys is shown in Fig. 3. Samples solidified upward with
or without a magnetic field show an initial Pb content of ∿ 52 w/o and
freeze dendritically up to fraction solid of about 0.25. Their macro-
segregation profiles are slightly different at large f_s but certainly
macrosegregation is quite evident in both. On the contrary the sample shown
in Fig. 3 which was solidified vertically downward shows very little macro-
segregation and is two phase composite over most of its length. As shown in
Table I, the dendritic region in this sample has not been completely
eliminated by inverted solidification as did occur at 0.5 μm/s. This is
probably due to the closeness of the value of G_L/V compared to the critical
value for plane front growth. (See discussion below and Fig. 7).

With an initial composition closer to the eutectic composition (40.7
w/o Pb) macrosegregation during upward solidification is reduced compared
to 43.0 w/o Pb alloys but is still significant as shown in Fig. 4. The

sample solidified dendritically to a fraction solid of 0.06. On the contrary, the sample solidified downward has a reduced level of macrosegregation and is two-phase composite over its entire length.

Of all the Pb-rich samples solidified upward only one was composite over its entire length (with the exception of a 1 mm initial transient). The composition of this sample was close to the eutectic composition and it was solidified relatively rapidly (40.7 w/o Pb, 5.1 μm/s). The macrosegregation data for this sample is shown in Fig. 5.

Discussion of Results

Upward Solidification - No Field

The extensive macrosegregation shown in Figs. 1 through 5 occurs only for alloys on the Pb-rich side of the eutectic when freezing vertically upward. Experiments on the Sn-rich side of the eutectic under conditions identical to those used in the Pb-rich experiments exhibit only a relatively small amount of macrosegregation which can be quantitatively accounted for by thermal diffusion alone. An example of measured macrosegregation on the Sn-rich side is shown in Fig. 6. The data agrees with previous work of Verhoeven, Warner & Gibson[9], and can be fit using their equation (17) with a thermal diffusion coefficient, D, of 2.1×10^{-8} cm^2/(s·K), a diffusion coefficient of 0.6×10^{-5} cm^2/s and no mixing near the liquid-solid interface (δ large). This absence of significant macrosegregation on the Sn-rich side in experiments conducted under conditions identical to those on the Pb-rich side is strong evidence that solutal convection (and not thermal convection caused by radial temperature gradients) is the cause of the extensive macrosegregation on the Pb-rich side of the eutectic.

It is useful to describe a qualitative model for the macrosegregation and resultant changes in microstructure for Pb-rich alloys. Solutal convection is sufficiently vigorous to disrupt the normal diffusion controlled (Sn-rich) solute field near the liquid-solid interface regardless of whether it is planar or dendritic. This solute is transported by the convection to the bulk liquid far from the interface which is almost always well mixed* by the radial temperature gradients which exist there[9]. Hence the bulk liquid, which initially was of composition C_o on the Pb-rich side of the eutectic, gradually becomes more Sn-rich. This causes a slow change in the solid to compositions which are also more Sn-rich as solidification proceeds. The transition from dendritic to composite structure appears to occur when the solid composition is close enough to the eutectic composition that plane front composite growth becomes stable as documented below. After plane front solidification is established, macrosegregation continues until the bulk liquid composition approaches the eutectic composition. Because the average composition in the liquid at the interface must be very close to the eutectic composition for two-phase plane front growth, the average composition gradient in the liquid vanishes when the bulk liquid composition reaches the eutectic composition. At this point solutal convection presumably ceases. This situation is reflected by the sharp break at $f_s \sim 0.22$ of the macrosegregation curve in Fig. 2. The fact that the solid composition at this point is $\sim$ 44 w/o Pb and not equal to the

---

* In the present experiments the composition of the liquid, determined after quenching, was constant to within $\pm$ 0.25 w/o Pb. The large sample size ($\sim$ 2 mm) used for chemical analysis prevents detection of the solute boundary layer.

liquid composition (38.1 w/o Pb) is caused by a thermal diffusion effect[6].
From Eq. (15) of Ref. 9, the average composition gradient vanishes when
the average solid composition, C_s, is $C_E(1+D'G_L/V)$, which for this alloy
and these growth conditions is 43.9 w/o Pb. Macrosegregation after
this point is greatly reduced and is caused only by thermal diffusion.

A quantitative description of the location of dendrite disappearance is
possible. Fig. 7 is a plot of G_L/V vs. the composition of the solid at the
position where the structure changed from dendritic to composite. It
resembles the expected form of the relation between G_L/V vs. composition for
the stability of plane front solidification, i.e., it falls slightly below
the requirement of the simple constitutional supercooling criterion

$$G_L/V = - m(C_E - C_s)/D$$

where m = 3.2 K/(w/o) and is the liquidus slope of the Pb-rich phase. It
also agrees with the data of Davis & Fryzuk[2] on zone melted off-eutectics
where macrosegregation is avoided by the fact that solid of constant com-
position is fed into the melted zone. Hence the transition from dendritic
to composite structure occurs when macrosegregation has caused the composition
of the solid to change to a level which satisfies a stability criterion for
plane front growth of a composite.

Quantitative description of the observed macrosegregation is more
difficult. Verhoeven et al.[6,9], using a thermotransport-corrected Burton-
Prim-Slichter[10] type (stagnant film) analysis of plane front composite
growth, have formulated an expression to predict macrosegregation. The 40.7
w/o Pb sample run at 5.1 μm/s is dendritic for an extremely short distance
(long compared to D/V) and hence this analysis is applicable. The pre-
viously given value of the thermal diffusion coefficient D', and a value of

90 μm for δ (the thickness of the unmixed zone near the interface) gave the best fit to the measured data in close agreement with δ values of Verhoeven et al.[9]. This calculated curve of the macrosegregation is shown superimposed on the data of Fig. 5. In this experiment, it was determined experimentally that the liquid composition remained on the Pb-rich side of the experiment up to the quench point and solutal convection probably existed throughout this experiment. The calculated value of the bulk liquid composition using this value for δ also agreed to within 0.25 w/o with the measured composition of the quenched liquid. The success of this approach during composite growth is somewhat suprising given the fact that the driving force for solutal convection only exists in the diffusion boundary layer. On the contrary, samples with long regions of dendritic growth cannot be fit with this equation. In the data shown in Fig. 3 a substantial number of data points exist in the dendritic zone of the sample and a marked change in slope occurs as the volume fraction of dendrites decreases. Clearly the existence of the dendritic interface influences both the driving force for solutal convection and the geometry for the flow. Fluid flow during dendritic solidification[11] is known to require a different approach to macrosegregation than a stagnant film approach. Quantitative description of the macrosegregation curves during dendritic growth is a topic for future research.

It is significant to note several aspects of solutal convection observed in this research. Fig. 8 shows an optical micrograph of a quenched liquid solid interface of a 43.0 w/o Pb alloy freezing at 2.6 μm/s. The sample was quenched at f_s = 0.1, so solutal convection was present at the time of

quenching. The Pb dendrites are uniformly spaced across the sample and the eutectic interface appears quite flat. It seems unclear that a single (or double) convection cell would lead to such a microstructure.

Additional insight into the nature of solutal convection is seen in Fig. 2, where the sharp break in the data at $f_s \sim 0.22$ marks the transition from macrosegregation caused by solutal convection to macrosegregation caused by thermal diffusion. This sharp transition from regimes of convection to no convection may be an indication of the extremely low concentration differences (i.e., deviation from eutectic composition) necessary for the onset of convection. Low concentrations for the onset of solutal convection during single phase solidification have been predicted theoretically[12]. For example, for vertical solidification of single phase Pb containing Sn, at an interface velocity of 1 μm/s and a temperature gradient of 200 K/cm, solutal convection will occur at all compositions above 3×10^{-4} w/o Sn.

Another suprising feature of solutal convection is the failure of the small (3 mm) diameter container to suppress convection. The results of Coriell et al.[12] indicate that a solute Rayleigh number based on a length of D/V is significant for the prediction of the onset of solutal convection during solidification. The fact that D/V is smaller than the radius of the tubes used in this study may explain this observation.

The presence of growth rate fluctuations has been observed in some cases in the present study. However, as can be seen for example in Fig. 1, many samples have been obtained which contain no fluctuations. Hence, it is our belief that these fluctuations are caused by artifacts, such as for example, by nonsteady thermal contractions[13]. Solutal convection seems to

be sufficiently steady so as to not cause growth rate fluctuations.

Upward Solidification - Magnetic Field

Static magnetic fields have long been known to influence the flow of electrically conducting liquids[14]. Chandrasekhar[15] calculated the influence of a vertical magnetic field on suppression of thermal convection in an infinite horizontal layer of fluid heated from below. Other theoretical work has been performed for different geometries. Experiments on liquid mercury[16] confirmed the inhibition of thermal convection by a vertical magnetic field. During solidification, liquid temperature fluctuations and associated growth rate fluctuations and solute banding caused by time-dependent convection during the horizontal growth of crystals were eliminated by imposition of a vertical magnetic field[17,18,19]. However, time independent laminar flow may still have been present. Because of this previous work, attempts were made in the present study to suppress solutal convection and the concomitant macrosegration by the imposition of a static magnetic field.

For most experiments a vertical field of 0.1T (1 kilogauss) was used based on the following analysis from Chandrasekhar[15]. The fluid elements are subject to the Lorentz force which is proportional to curl $\overline{H} \times \overline{H}$, where $\overline{H}$ is the magnetic field in the fluid. Clearly, if $\overline{H}$ is constant the Lorentz force vanishes, and the magnetic field does not affect the fluid motion. Even though the applied magnetic field is constant, the magnetic field in the fluid is not in general constant. In fact, a constant $\overline{H}$ will satisfy the basic partial differential equation for $\overline{H}$ if and only if curl $(\overline{u} \times \overline{H})$ vanishes, where $\overline{u}$ is the fluid velocity. Clearly if $\overline{u}$ is parallel to $\overline{H}$,

then $\overline{u} \times \overline{H}$ vanishes, and the magnetic field has no effect on the fluid motion, i.e., if the fluid motion does not cross the magnetic field, there is no effect. More generally, however, a constant $\overline{H}$ is possible if and only if $(\overline{H} \cdot \nabla)\overline{u} = 0$ for an incompressible fluid, which reduces to $H_i (\partial u / \partial x_i) = 0$ for a magnetic field only in the x_i direction. Thus, a constant magnetic field and a vanishing Lorentz force will occur if the fluid velocity is independent of the coordinate x_i in the direction of the magnetic field. Such a case occurs for flow between two infinite horizontal plates heated from below where the critical Rayleigh number is unaffected by a horizontal magnetic field.

Experimental results shown in Figs. 2-3, show little or no effect of a 0.1T (1 kilogauss) magnetic field on reducing the macrosegregation produced by solutal convection. As was described above, the solutal convection present in these experiments is sufficiently steady that growth rate fluctuations do not occur. Hence the nature of the convection present in these experiments is quite different from that observed by Utech & Flemings[17,18] during horizontal solidification. Recent theoretical work may explain the ineffectiveness of a magnetic field on damping solutal convection[12]. For example, for vertical solidification of single phase Pb containing Sn, at an interface velocity of 1 μm/s, a temperature gradient of 200 K/cm and a imposed vertical magnetic field of 1T (10 kilogauss), solutal convection will occur at all compositions above 3×10^{-3} w/o Sn.

Downward Solidification

As shown by the data in Figs. 2-4, solidification of Pb-rich off-eutectic alloys downward greatly reduces macrosegregation. In fact the

remaining macrosegregation in these experiments can be quantitatively accounted for by thermal diffusion. In this geometry the Sn-rich solute layer near the interface is above the Pb-rich liquid away from the interface and for the conditions used in these experiments, creates a stable density gradient near the interface even though the temperature gradient is destabilizing. Outside the solute diffusion layer the density gradient is destabilizing.

At first glance the reason for the reduction of macrosegregation during downward solidification appears obvious. Solutal convection is eliminated because of the stable density gradient near the interface and hence diffusion controlled solidification is not interrupted. However, the large vertical temperature gradient present during these experiments would tend to promote extensive thermal convection farther from the interface. The results indicate, however, that such flow if it exists, is sufficiently distant from the diffusion boundary layer as to be ineffective in causing significant macro-segregation.

A second rationale could be that the small tube diameter (3 mm) is effective in greatly reducing the thermal convection far from the interface. One can calculate a thermal Rayleigh number $R = \alpha g G_L r^4 / \nu \kappa$ for this geometry, where α is the expansion coefficient, g the acceleration of gravity, G_L the temperature gradient in the liquid, r the tube radius, ν the kinematic viscosity and κ the thermal diffusivity. For typical parameters[12] of the present experiments $R \stackrel{\sim}{=} 65$, which is very close to typical critical Rayleigh numbers for closed containers as summarized by Verhoeven[20]. For larger tubes thermal convection away from the interface may become more effective in causing macrosegregation and hence it is anticipated that suppression of

macrosegregation by solidification downward may be very sensitive to tube diameters. This effect was not, however, investigated in the present study.

Conclusions

1. Solute gradient induced convection can cause extensive macro-segregation in off-eutectic alloys.

2. Macrosegregation is frequently sufficiently large to prevent plane front solidification of the alloy.

3. The transition from dendritic to composite structure occurs when the composition of the solid is close enough to the eutectic composition to satisfy a stability criterion based on G_L/V.

4. Horizontal or vertical magnetic fields of 0.1T (1 kilogauss) do not prevent macrosegregation of off-eutectic alloys caused by solutal convection.

5. For small diameter samples, inverted solidification eliminates macrosegregation caused by solutal convection.

B. CALCULATION OF CONDITIONS FOR THE ONSET OF SOLUTAL CONVECTION

Introduction

During the vertical directional solidification of a binary alloy at
constant velocity V, the steady state concentration field is exponential
in form, i.e., $c = c_\infty + (c_\infty/k)(1-k) \exp(-Vz/D)$, where c is the concentration
of solute in the liquid at a distance z from the solid-liquid interface,
the distribution coefficient k is the ratio of the solute concentration
in the solid at the solid-liquid interface to the solute concentration in
the liquid at the solid-liquid interface, c_∞ is the solute concentration
as $z \to \infty$, and D is the liquid diffusion coefficient. The temperature
field is also exponential but with decay length κ/V, where κ is the thermal
diffusivity of the liquid. In general, $\kappa \gg D$ so that the temperature
gradient G_L in the liquid is essentially constant in the region in which
the concentration gradient is significant. It is well known that as the
concentration is increased for fixed V and G_L the planar solid-liquid
interface becomes morphologically unstable. The constitutional supercooling
principle predicts instability when $mG_C > G_L$, where m is the slope of the
liquidus line and $G_C = (c_\infty V/Dk)(k-1)$ is the concentration gradient at the
planar solid-liquid interface. In addition to morphological instability,
there is the possibility of a convective instability. For solidification
vertically upwards (positive z-direction) the thermal gradient alone
results in a negative density gradient (stabilizing) while the solute
gradient alone can cause a negative (stabilizing) or positive (destabilizing)
density gradient depending on the density variation with solute concentration
and the distribution coefficient. When the solute gradient gives rises
to a positive density gradient, e.g., a solute which is rejected at the
solid-liquid interface and which is lighter than the solvent, a convective

53

instability will occur if the solute concentration is sufficiently large that the destabilizing solute field overcomes the stabilizing influences of the thermal field and viscous effects. Thus, for fixed values of velocity V and temperature gradient G_L, as the solute concentration increases, one expects an instability to occur, i.e., for sufficiently small solute concentrations, the planar interface is stable and the horizontal components of the fluid flow velocity vanish (a vertical flow due to the volume change on solidification is always present), but for solute concentrations above some critical value the interface and the fluid flow field are unstable.

In our previous publications[12,21,22], a linear stability analysis and numerical algorithms have been described which allow the calculation of the critical concentration for the onset of convective and morphological instabilities during the directional solidification of binary alloys. In addition, a number of results were obtained for the specific case of the solidification of lead containing tin. In this report we combine the previous results and new results with particular emphasis on small constant gravitational accelerations.

Results and Discussion

We recall that the dependence of the perturbed temperature, concentration, fluid velocity, and interface shape on the horizontal coordinates x and y and the time t is of the form exp $[\sigma t + i(\omega_x x + \omega_y y)]$, where ω_x and ω_y are spatial frequencies. If the real part, σ_r, of the time constant σ is positive for any values of ω_x and ω_y, the system is unstable. If $\sigma_r < 0$ for all values of ω_x and ω_y, the system is stable. We refer to instabilities

corresponding to large values of ω (small wavelengths, $\lambda = 2\pi/\omega$) as morphological instabilities and to instabilities corresponding to small values of ω (large wavelengths) as convective instabilities.

The basic results for the critical concentration c_∞^{**} above which instability occurs as a function of growth velocity are shown in Fig. 9. We have previously discussed the curves corresponding to gravitational accelerations of $g_e = 980$ cm/s^2 and $10^{-4} g_e$. For $g = 10^{-6} g_e$, the convective instability occurs at a lower concentration than the morphological instability only if $V < 1.3$ μm/s. The concentration above which the interface is unstable as a function of the spatial frequency $\omega = (\omega_x^2 + \omega_y^2)^{\frac{1}{2}}$ of the perturbation is shown in Figs. 10 and 11 for $V = 1.2$ and 1.3 μm/s, respectively. The critical concentration c_∞^{**} corresponds to the minimum value of the concentration as a function of ω. The solid curves on the right of Figs. 10 and 11 correspond to morphological instability while the solid curves on the left correspond to convective instability. Along the curves the real part of σ vanishes; along the solid curves σ vanishes while along the dashed curve, which connects the convective and morphological branches, the imaginary part σ_i of σ is non-zero. The value of σ_i is shown in the insets in Figs. 10 and 11 and attains a maximum value of less than $2.0(10^{-4})$s^{-1}. For $V = 1.2$ μm/s, the minimum value of c_∞ is 4.61 wt. % at $\omega = 1.35$ cm^{-1} or a wavelength $\lambda = 4.7$ cm. There is a relative minimum on the morphological branch at $\omega = 204$ cm^{-1} with $c_\infty = 6.47$ wt. % (not shown in the figure). For $V = 1.3$ μm/s, the minimum value of c_∞ is 5.98 wt. % at $\omega = 210$ cm^{-1} (not shown in the figure) and a relative minimum with $c_\infty = 7.15$ wt. % at $\omega = 1.4$ cm^{-1}.

In our previous publications, it was shown that the critical concentrations for convective instability could be correlated in terms of the Rayleigh number R' and the solute Rayleigh number S' based on the length (D/V), i.e.,

$$R' = -g\alpha G_L (D/V)^4 / \nu\kappa$$

$$S' = -g\alpha_c G_c (D/V)^4 / \nu D = (g\alpha_c / \nu Dk)(1-k)(D/V)^3 c_\infty,$$

where α is the thermal coefficient of expansion, ν is the kinematic viscosity and α_c is the solutal coefficient of expansion. To fit our previous results we used an expression of the form

$$S' + a_1 (R')^{a_5} = a_2 \tag{1}$$

or in dimensional form

$$c_\infty = a_3 V^3 / g + a_4 (V^3/g)(g G_L / V^4)^{a_5}, \tag{2}$$

where the a_i are constants independent of G_L, c_∞, V and g. The a_i were determined by minimizing the differences between the numerical values of c_∞ and the values obtained from the above expression. Using the previously determined values of the a_i, we calculate critical concentrations of 0.32, 2.48, 4.27, and 5.42 wt. % for V = 0.5, 1.0, 1.2, and 1.3 μm/s, respectively, for $g = 10^{-6} g_e$; these are in reasonable agreement with the numerically calculated values of 0.31, 2.39, 4.61, and 7.15 wt. % for V = 0.5, 1.0, 1.2, and 1.3 μm/s.

In our previous calculations for $g = g_e$, we obtained oscillatory instabilities with $\sigma_i \sim 0.1$ s^{-1} or a period of the order of 60 s. For $g = 10^{-6} g_e$, $\sigma_i \sim 10^{-4}$ s^{-1} or a period of the order of $6(10^4)$ s. This suggests that the fluid motions are very slow at reduced gravity levels.

To further verify this, we carried out a few calculations with $\sigma_r \neq 0$. For $V = 1.2$ μm/s and $g = 10^{-6} g_e$, a concentration of 7.68 wt. % is required for $\sigma_r = 10^{-4}$ s^{-1} on the convective branch. Thus, although $\sigma_r > 0$ for $c_\infty > 4.61$ wt. % for $V = 1.2$ μm/s, the amplitude of the convective instability for $c_\infty = 7.68$ wt. % increases very slowly, requiring 10^4 s to increase by a factor of e. In contrast, the morphological instabilities are only slightly affected by reduced gravity. For example, for $V = 1.2$ μm/s and $\omega = 205$ cm^{-1}, the concentrations corresponding to $\sigma_r = 0$, 10^{-4}, and 10^{-2} s^{-1} are 6.47, 6.50 and 11.0 wt. %, respectively, for $g = 10^{-6} g_e$ whereas for $g = g_e$, $\sigma_r = 0$, 10^{-4} and 10^{-2} s^{-1} correspond to concentrations of 6.47, 6.49 and 11.2 wt. %, respectively. We emphasize that these calculations for $g = 10^{-6} g_e$ assume that g is constant, and since the convective instabilities develop very slowly, it seems unlikely that this is a valid assumption for space experiments.

Liquid metals have low Prandtl numbers, e.g., the Prandtl number $Pr = \nu/\kappa = 0.0225$ for lead. In contrast, a large class of liquids have much larger Prandtl numbers, e.g., $Pr \sim 10$ for water. In order to study the effect of Prandtl number, we have carried out some calculations using the properties of lead-tin alloys except that the thermal conductivities and thermal diffusivities of both liquid and solid were 100 times lower than the actual conductivities and diffusivities. Thus, the Prandtl number for this hypothetical alloy is 2.25; for fixed G_L and V the thermal Rayleigh number is also increased by a factor of 100. The tin concentrations at the onset of convective instability as a function of growth velocity for $G_L = 200$ K/cm for lead-tin alloys (Pr = 0.0225) and the hypothetical alloy

(Pr = 2.25) are shown in Fig. 12. At low velocities the critical con-
centrations are a factor of 50 greater for the liquid with reduced thermal
properties than for the lead alloy. At higher velocities, the two curves
approach each other and the thermal properties have little effect on the
critical concentration. This behavior can be understood qualitatively
from eq. (1) through the effect of the reduced thermal properties on the
Rayleigh number; in general, however, we expect the a_i to depend on the
Prandtl number.

A few additional calculations of the effect of magnetic fields and
thermal gradients were carried out. These together with previous results
are presented in Figs. 13 and 14. For discussion of these results, see the
previous publications.

The present linear stability analysis and numerical algorithm allows
the determination of the onset of convective and morphological instability
during directional solidification. We plan additional calculations for
conditions and materials relevant to experimental investigations. For a
particular double diffusive system with linear temperature and solute
gradients, Baines and Gill[23] have shown that the spatial frequency ω,
corresponding to the most unstable mode, increases very rapidly as the
concentration exceeds the critical concentration for the onset of in-
stability. Calculations of σ as a function of ω for fixed concentration
c_∞ will allow us to determine whether similar behavior occurs during
directional solidification. Mathematical analysis and algorithm development
for fluid flow occurring in the non-linear regime (after the onset of
instability), with particular emphasis on solute distribution, will be
initiated in the near future.

Acknowledgments

References

1. F. R. Mollard and M. C. Flemings, Trans. AIME, 1967, Vol. 239, p. 1534.

2. K. G. Davis and P. Fryzuk, Can. Met. Quart., 1971, Vol. 10, p. 273.

3. J. D. Verhoeven and R. H. Homer, Met. Trans., 1970, Vol. 1, p. 3437.

4. J. D. Holder and B. F. Oliver, Met. Trans., 1974, Vol. 5, p. 2423.

5. L. Vandenbulcke, R. J. Herbin and G. Vuillard, J. Cryst. Growth, 1976, Vol. 36, p. 53.

6. J. D. Verhoeven, K. Kingery and R. Hofer, Met. Trans., 1975, Vol. 6B, p. 647.

7. W. J. Boettinger, H. E. Burdette and M. Kuriyama, Advances in X-ray Analysis, 1980, Vol. 23, p. 209.

8. M. J. Tschetter and R. Z. Bachman, Talanta, 1974, Vol. 21, p. 106.

9. J. D. Verhoeven, J. C. Warner and E. D. Gibson, Met. Trans., 1972, Vol. 3, p. 1437.

10. J. A. Burton, R. C. Prim, and W. P. Slichter, J. Chem. Phys. 1953, Vol. 21, p. 1987.

11. M. C. Flemings and R. Mehrabian, Solidification, ASM, 1969, p. 311.

12. S. R. Coriell, M. R. Cordes, W. J. Boettinger and R. F. Sekerka, J. Cryst. Growth, 1980, Vol. 49, p. 13.

13. J. D. Verhoeven and E. D. Gibson, J. Cryst. Growth, 1971, Vol. 10, p. 235.

14. J. Hartmann and F. Lazarus, Kgl. Danske Videnskab. Selskab, Met.-Fys. Medd., 1937, Vol. 15, Nos. 6 & 7.

15. S. Chandrasekhar, Hydrodynamic Stability, Oxford Univ. Press, London, 1961 p. 146.

16. B. Lehnert and N. C. Little, Tellus, 1957, Vol. 9, p. 97.

17. H. P. Utech and M. C. Flemings, J. Appl. Phys., 1966, Vol. 37,
     p. 2021.

18. H. P. Utech and M. C. Flemings in Crystal Growth, edited by H. S. Peiser,
     Pergamon Press, New York, 1967, p. 651.

19. M. C. Flemings, Solidification Processing, McGraw-Hill, New York,
     1974, p. 227.

20. J. D. Verhoeven, Trans. Met. Soc. AIME, 1968, Vol. 242, p. 1940.

21. W. J. Boettinger, S. R. Coriell, F. S. Biancaniello and M. R. Cordes
     in NBS: Properties of Electronic Materials, edited by J. R. Manning
     and R. L. Parker, (NBSIR 78-1483, National Bureau of Standards,
     Washington, D.C.) p. 15.

22. W. J. Boettinger, S. R. Coriell, F. S. Biancaniello and M. R. Cordes
     in NBS: Properties of Electronic Materials, edited by J. R. Manning,
     (NBSIR 79-1767, National Bureau of Standards, Washington, D.C.) p. 25.

23. P. G. Baines and A. E. Gill, J. Fluid Mech., 1969, Vol. 37, p. 289.

Table I. Summary of Experiments

C_O (w/o Pb)	V (μm/s)	$G_L/V \times 10^{-6}$ (Ks/cm^2)	D/V (cm)	L (cm)	Fig. No.	$C_s(0)$ w/o Pb	$C_s(0.1)$ w/o Pb	C_s^D w/o Pb	z^D (cm)	f_s^D (z^D/L)	Geometry
43.0	0.5	7.2	0.12	5.2	2	72	61	58.8	0.6	0.12	a
43.0	0.5	7.2	0.12	11.8	2	72	61	60.5	1.3	0.11	a
43.0	0.5	7.2	0.12	7.3	2	69	62	58.6	0.9	0.12	b
43.0	0.5	7.2	0.12	11.2	2	68	65	61.2	1.6	0.14	c
43.0	0.5	7.2	0.12	6.0	2	56.0	45.5	—	$\sim$0	$\sim$0	d
43.0	1.3	2.8	0.05	5.0	—	47.5	46.0	—	0.1	$\sim$0	d
43.0	2.6	1.4	0.02	14.7	3	52	51.0	47.0	3.4	0.23	a
43.0	2.6	1.4	0.02	10.9	3	52	50.5	46	3.3	0.30	b
43.0	2.6	1.4	0.02	8.0	3	44.3	44.0	44.1	0.7	0.09	d
40.7	1.3	2.8	0.05	12.3	4	53	46.5	49.1	0.8	0.06	a
40.7	1.3	2.8	0.05	5.3	4	44.0	42.0	—	$\sim$0	$\sim$0	d
40.7	5.1	0.7	0.01	8.6	5	43.5	42.5	43.4	0.1	$\sim$0	a

a. Upward

b. Upward, 0.1T Vertical Magnetic Field

c. Upward, 0.1T Horizontal Magnetic Field

d. Downward

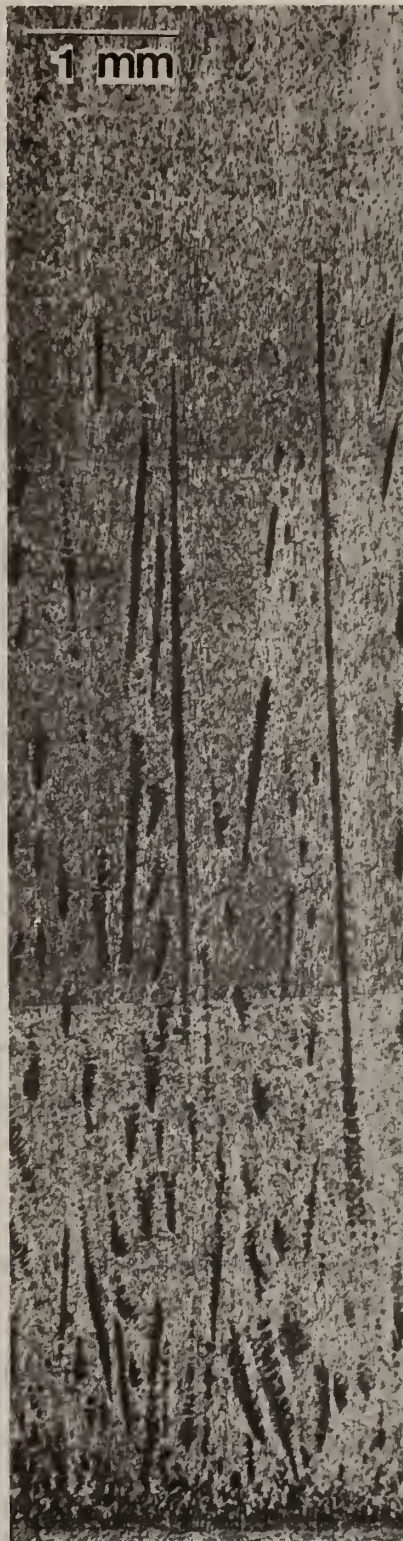The eutectic composition is 38.1 w/o Pb.

Fig. 1.   Longitudinal section of directionally solidified sample
          showing the change in volume fraction of Pb dendrites (dark)
          as a function of distance (fraction solidified). Solidification
          proceeded from bottom to top. At the extreme top there are
          no dendrites. Solidification velocity is 1.3 μm/s – original
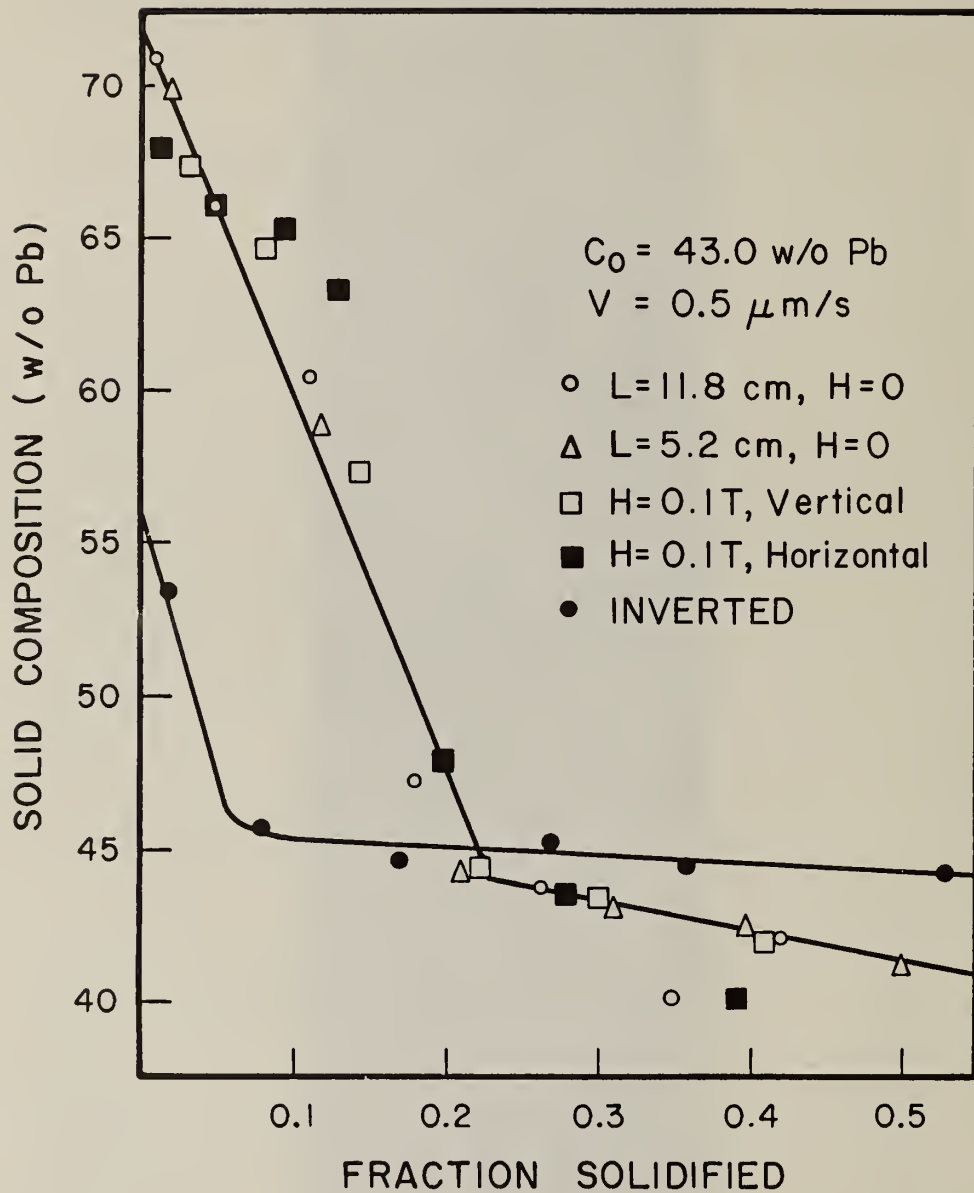   composition is 40.7 w/o Pb.

Fig. 2. Average solid composition versus fraction solidified for
43.0 w/o Pb alloys solidified at 0.5 μm/s showing extensive
macrosegregation during upward solidification, negligible
effect of magnetic field and large effect of inverted solidi-
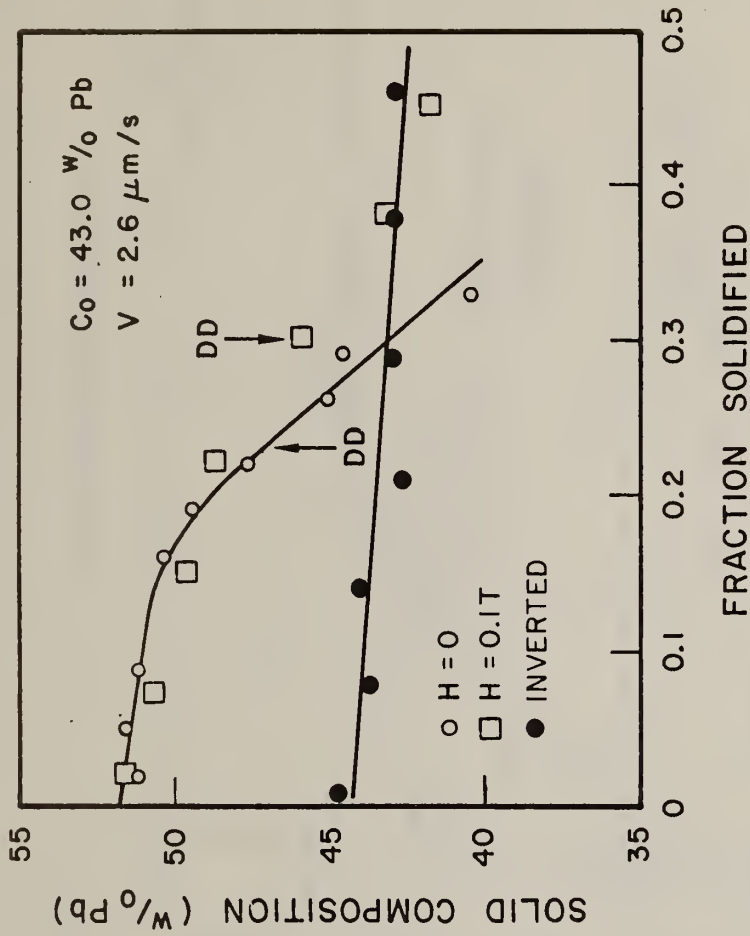fication on reduction of macrosegregation.

Fig. 3.   Average solid composition versus fraction solidified for
43.0 w/o Pb alloys solidified at 2.6 µm/s. Inverted solidi-
fication greatly reduces the macrosegregation. The symbol
DD respresents the positions of transition from dendritic to
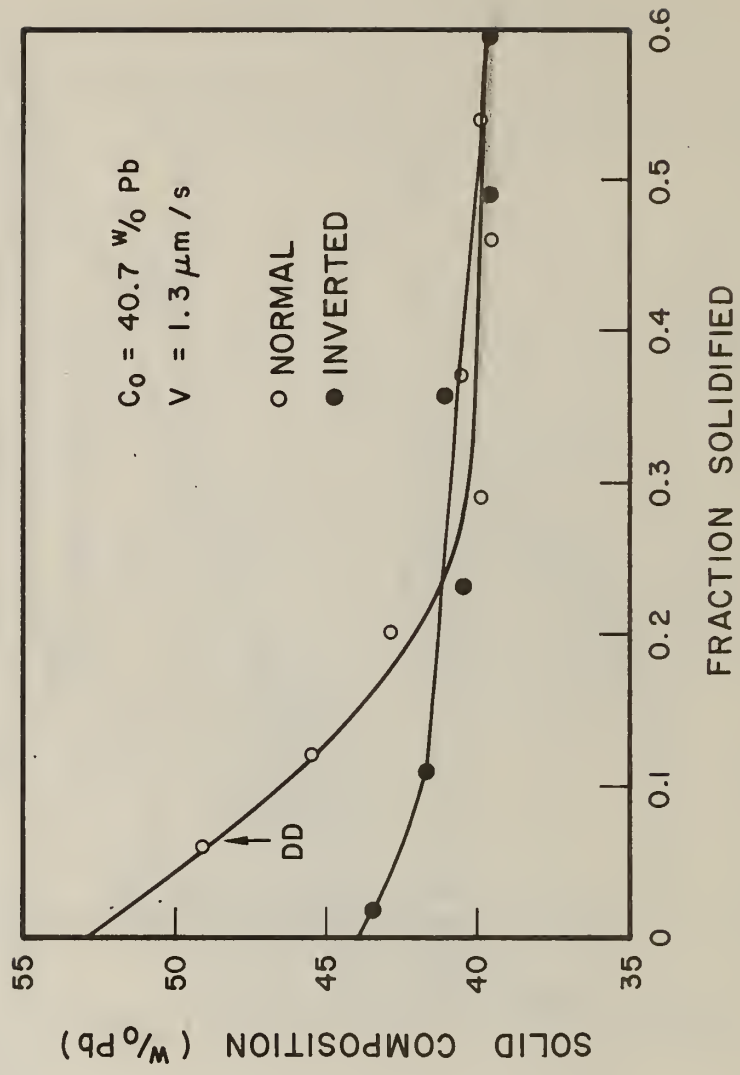composite structure.

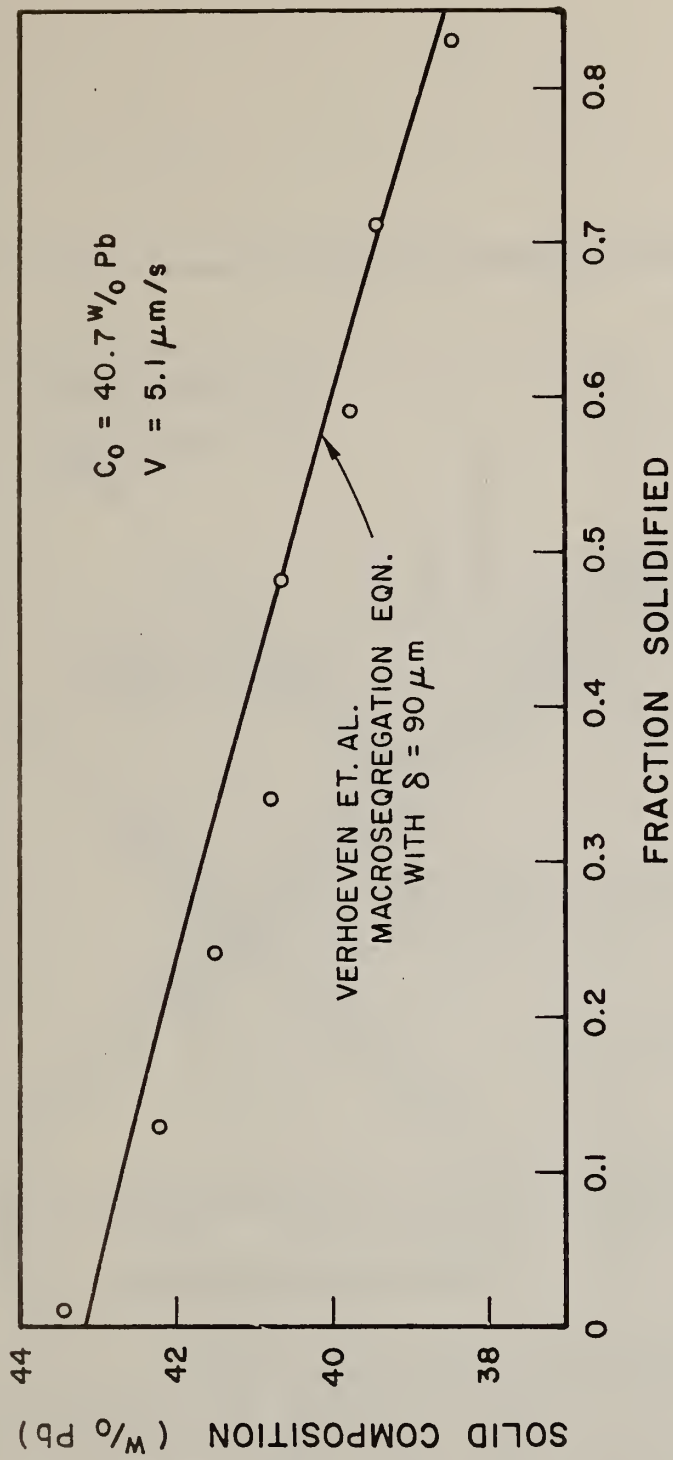Fig. 4.   Average solid composition versus fraction solidified for 40.7 w/o Pb alloys solidified at 1.3 μm/s.

Fig. 5. Macrosegregation data for a 40.7 w/o Pb alloy solidified upward at 5.1 μm/s. The curve is the best fit of the data using only δ as a parameter in equation (17) of Ref. (9).
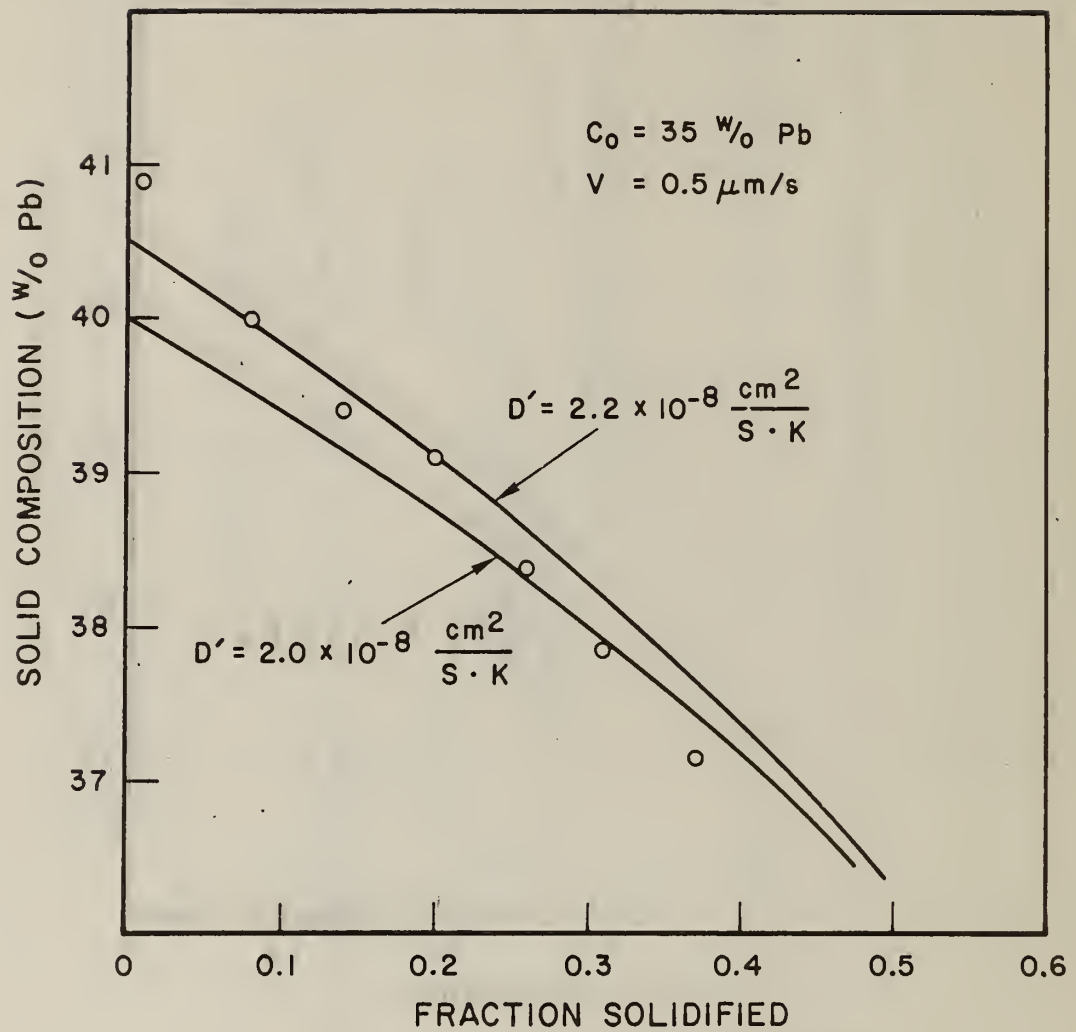
Fig. 6. Average solid composition versus fraction solidified for a 35 w/o Pb alloy at 0.5 μm/s. For this alloy on the Sn-rich side of the eutectic, solutal convection is absent and the relatively small amount of macrosegregation is caused by thermal diffusion.
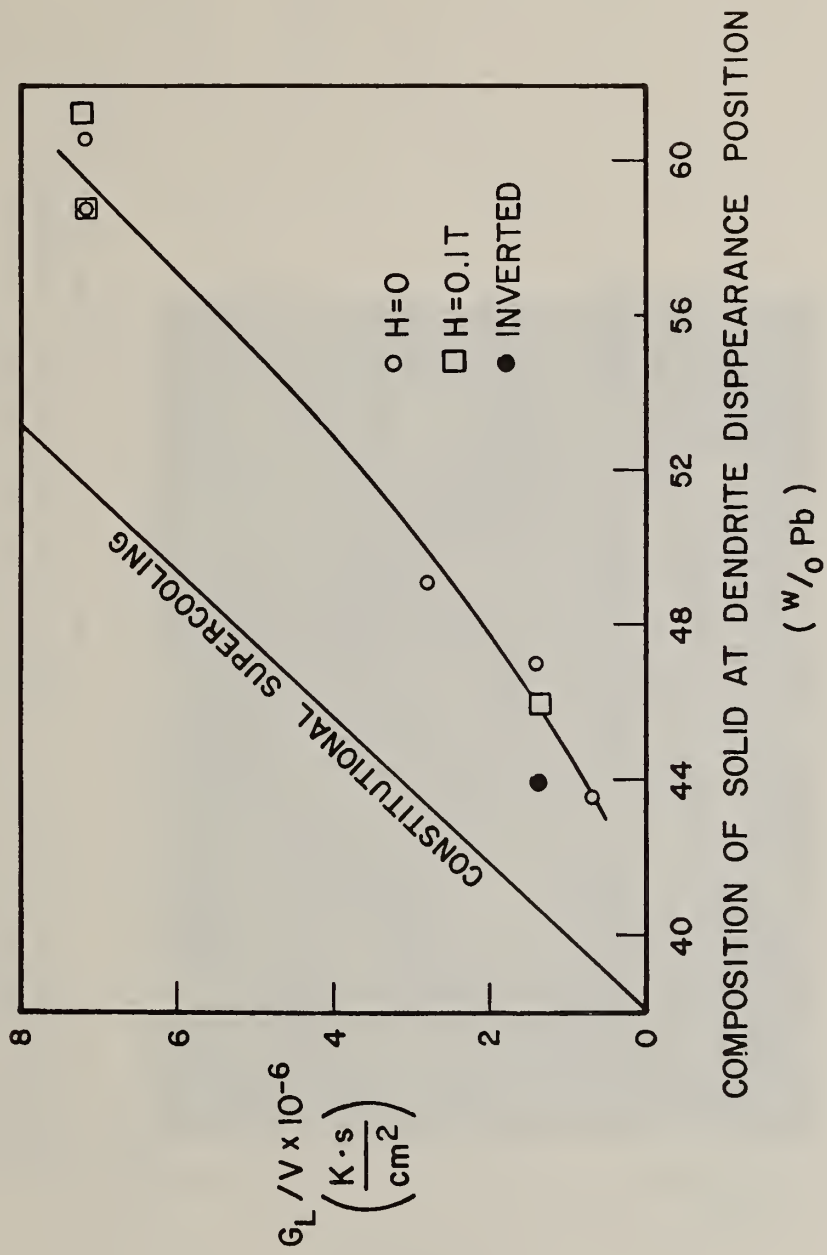
Fig. 7. A plot of G_L/V versus solid composition at the position of dendrite disappearance for all of the samples. The data follows the general trend of plane front interface stability for off-eutectic alloys.
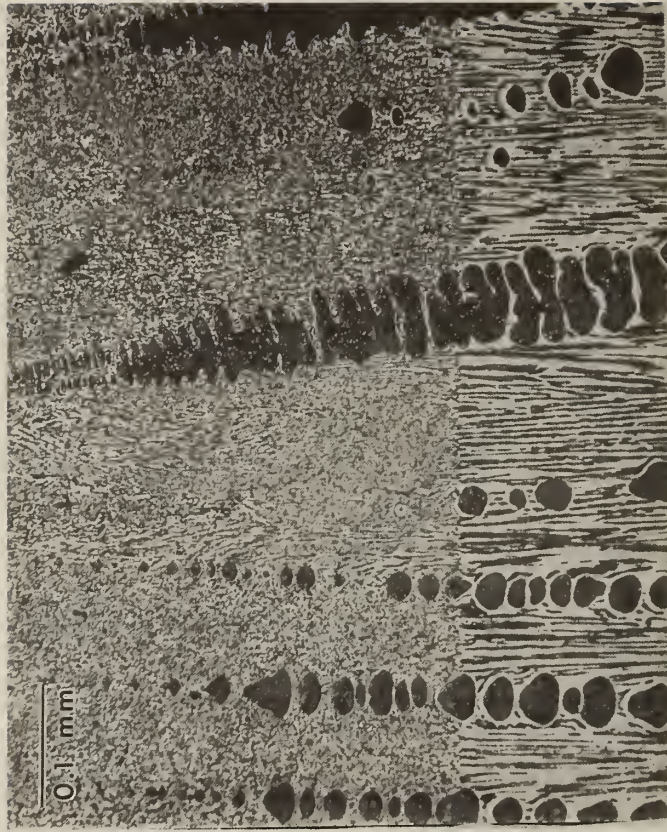
Fig. 8. Longitudinal section of liquid-solid interface quenched during directional solidification with solutal convection. Note the uniform distribution of Pb dendrites as well as the flatness of the interdendritic eutectic liquid-solid interface.
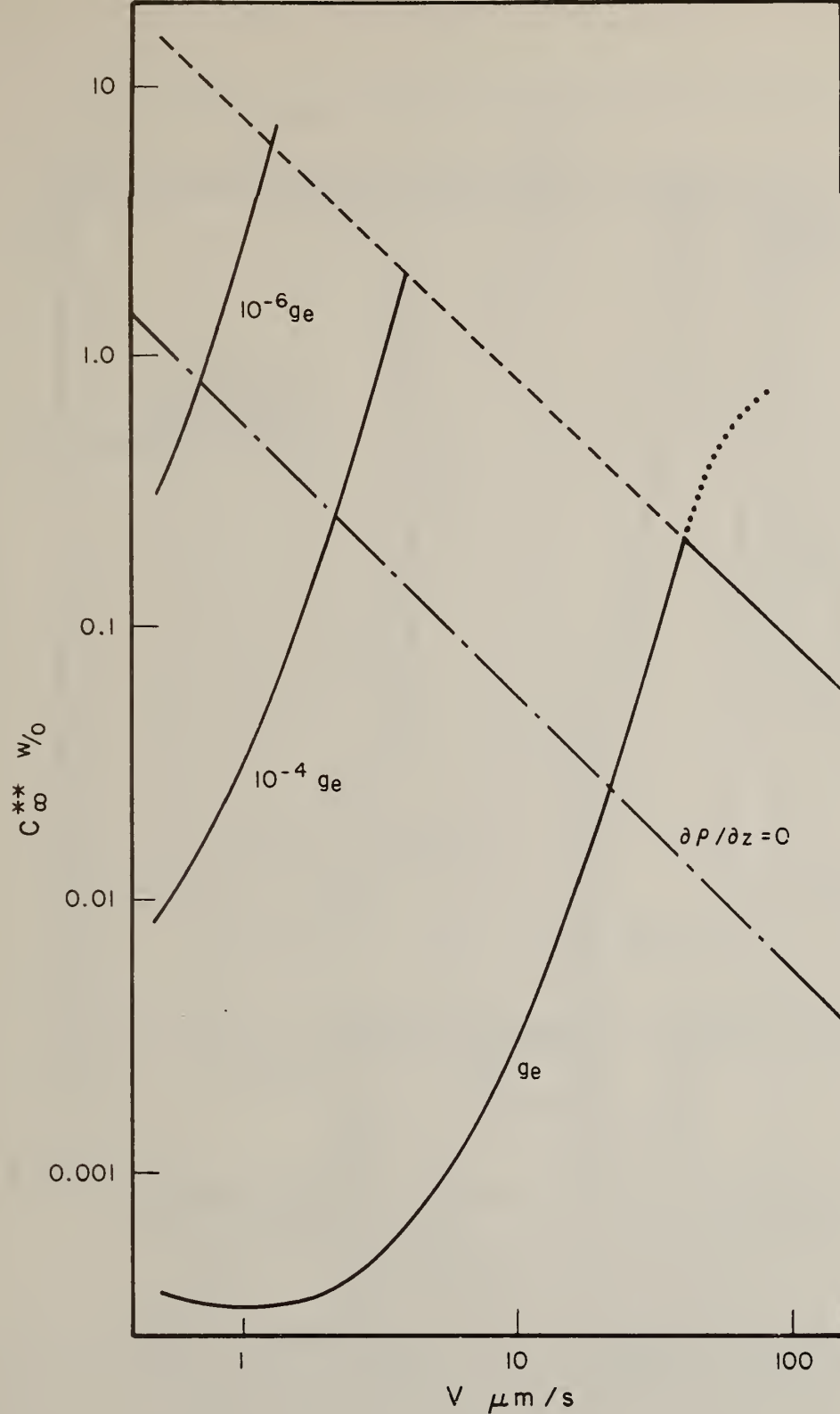
Fig. 9. The critical concentration c_∞^{**} of tin above which instability occurs as a function of the velocity V of directional solidification of lead-tin alloys for a temperature gradient G_L in the liquid of 200 K/cm. The solid curves represent gravitational accelerations of g_e = 980 cm/s^2, 10^{-4} g_e, and 10^{-6} g_e. The upper line with negative slope represents the onset of morphological instabilities; the nearly parallel dashed-dot line labeled $(\partial\rho/\partial z)$ = 0 represents the neutral density criterion. The dotted extension of the curve labeled g_e corresponds to oscillatory instabilities.

71

Fig. 10. The concentration at the onset of instability during directional solidification at V = 1.2 µm/s of a dilute alloy of tin in lead as a function of the spatial frequency ω of a sinusoidal perturbation; the temperature gradient G_L in the liquid is 200 K/cm and the constant gravitational acceleration is 980 (10^{-6}) cm/s². The solid curves mark the onset of non-oscillatory instabilities ($\sigma_i=0$); whereas the dashed curves mark the onset of oscillatory instabilities (the value of σ_i is given in the inset).
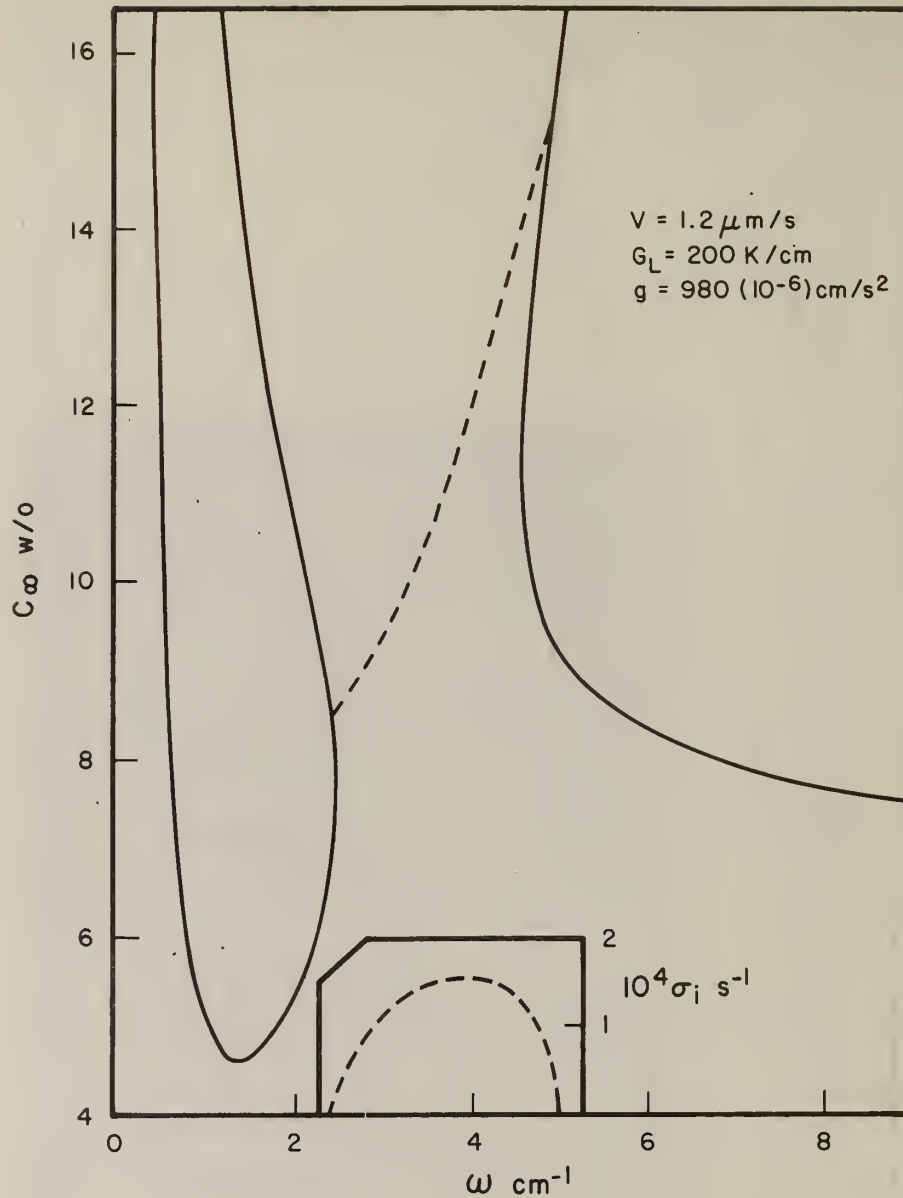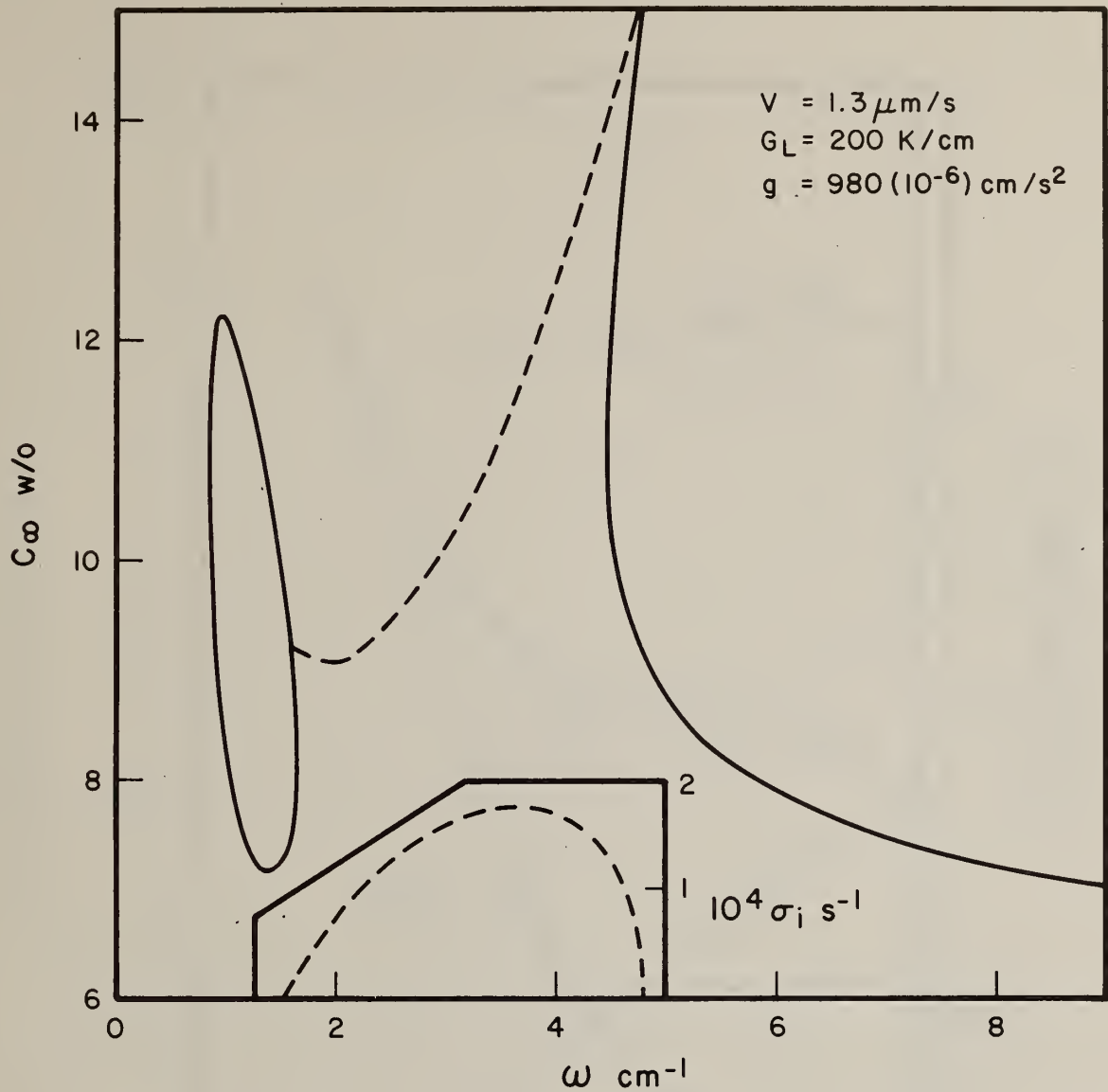
Fig. 11. The concentration at the onset of instability during directional solidification at V = 1.3 μm/s of a dilute alloy of tin in lead as a function of the spatial frequency ω of a sinusoidal perturbation; the temperature gradient G_L in the liquid is 200 K/cm and the constant gravitational acceleration is 980 (10^{-6}) cm/s². The solid curves mark the onset of non-oscillatory instabilities ($\sigma_i=0$); whereas the dashed curves mark the onset of oscillatory instabilities (the value of σ_i is given in the inset).
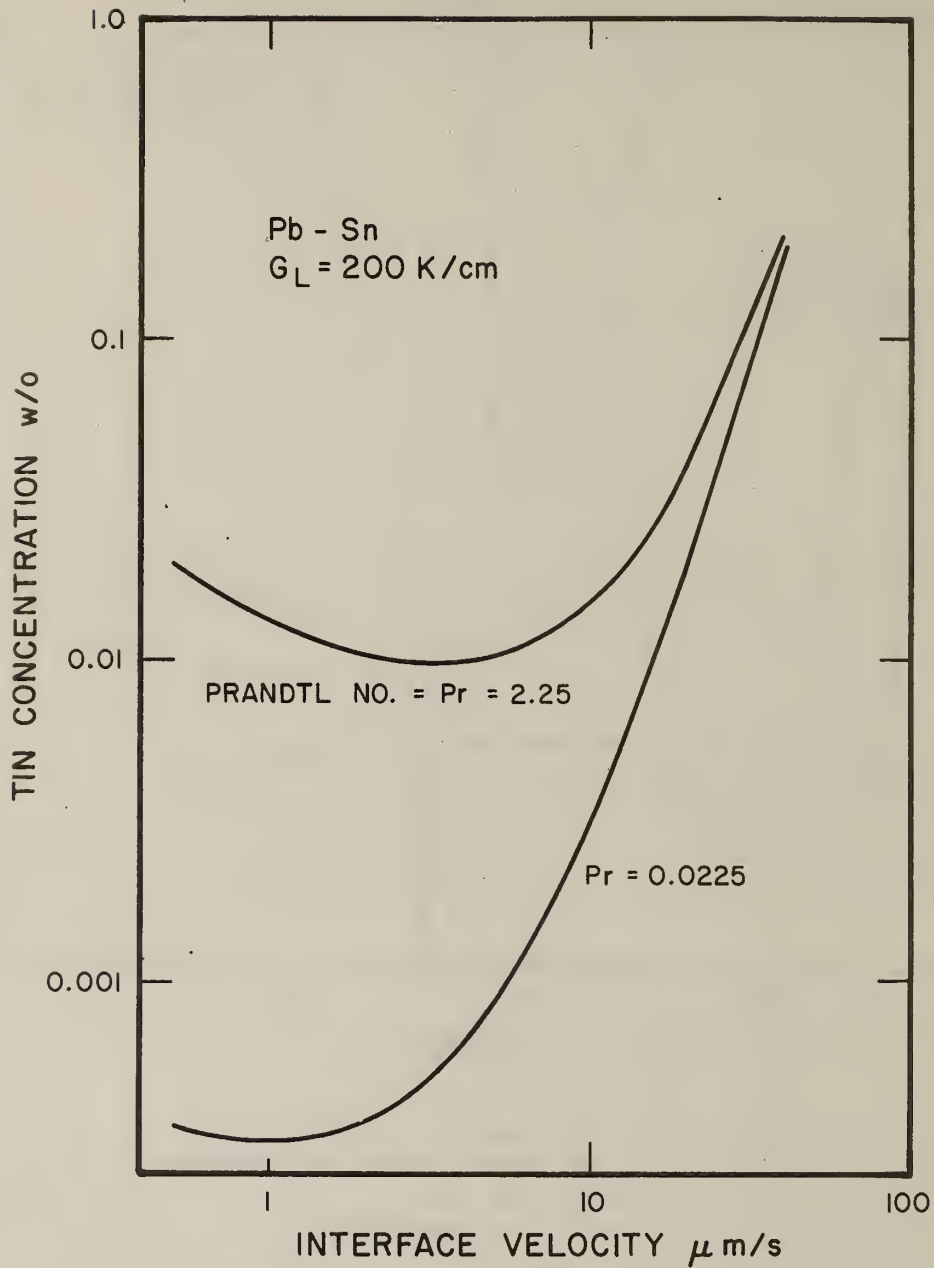
Fig. 12. The critical concentration of tin above which instability
occurs as a function of the velocity of directional solidi-
fication for a temperature gradient in the liquid of 200 K/cm.
The curve with Prandtl number Pr = 0.0225 corresponds to a
lead-tin alloy whereas the other curve corresponds to calculations
for a hypothetical lead-tin alloy with thermal properties
reduced by a factor of 100, i.e., Pr = 2.25.

74
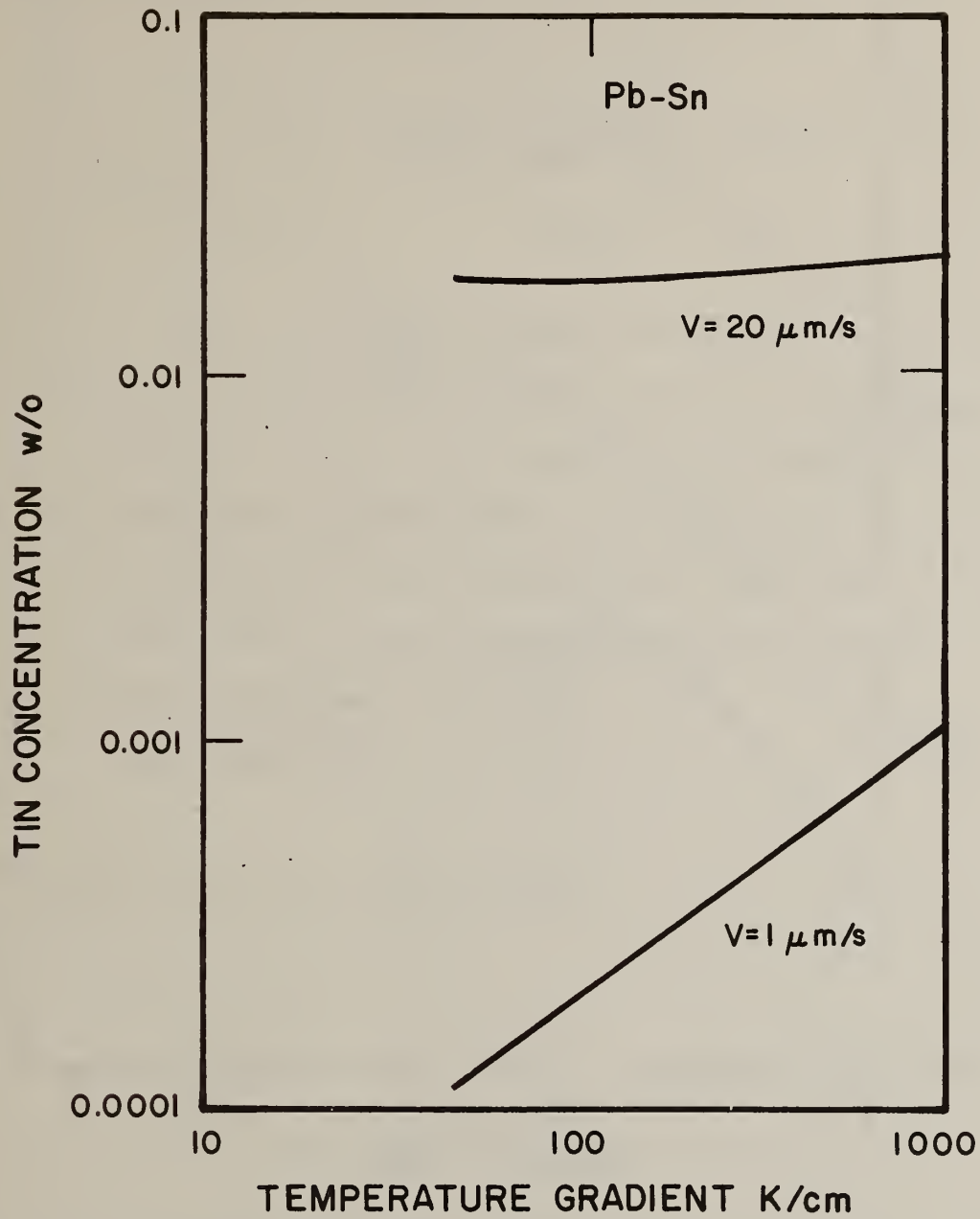
Fig. 13. The critical concentration of tin in lead above which in-
stability occurs as a function of the temperature gradient in
the liquid for solidification velocities of 1.0 and 20.0 μm/s.
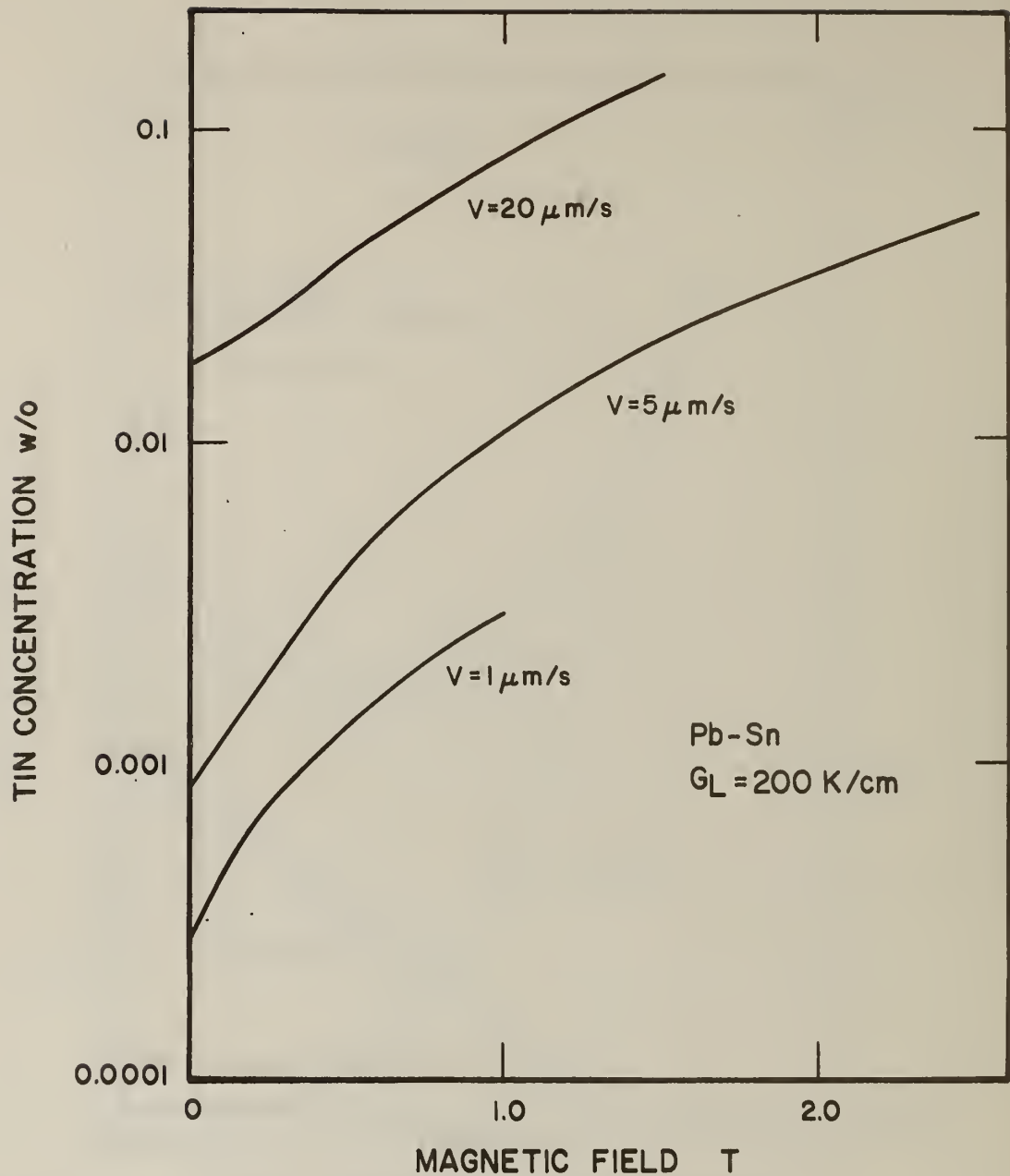
Fig. 14. The critical concentration of tin in lead above which in-
stability occurs as a function of the strength of a vertical
magnetic field for solidification velocities of 1.0, 5.0, and
20.0 μm/s and a temperature gradient of 200 K/cm.

Task 3

A Thermochemical Study of Corrosive Reactions in Oxide Materials

H. S. Parker

Ceramics, Glass and Solid State Science Division
Center for Materials Science

Summary

Phase assemblages of selected compositions on the joins
$K[Fe_{.5}Si_{.5}]O_2$–SiO_2 and $KFeO_2$–SiO_2 have been determined after heat
treatment at oxygen partial pressures of 10^{-6} and 10^{-17} atm and
temperatures in the 800°–1400°C range. Excessive reaction between
platinum containers and melts containing some ferrous iron was noted.
A comparison of conventional and containerless techniques for phase
equilibrium studies is presented.

Introduction

The objectives of this task are to investigate the nature, extent and limitations on experimental studies imposed by sample-container reaction at high temperature and to evaluate containerless techniques for melt and solid state investigations. Alkali and transition elements are among the most reactive and are of great technological importance because of their application in the fields of MHD, fuel cells, catalysts and solid state electronic and ionic conductors. Reaction with the container can severely compromise the bulk composition of the sample and adversely affect the electrical and chemical properties. This, together with the inability in general to electromagnetically levitate ceramic materials, makes low gravity experiments attractive for containerless study of such materials.

The general approach is to select a system of current technological importance and investigate: a) the maximum temperature limits for the container material and characterize the reaction products, b) determine the equilibrium phase assemblages in selected portions of the systems within the limitations imposed by a), and c) in collaboration with MSFC provide specimens for levitation experiments at MSFC and characterize and correlate results of levitation experiments with container experiments to evaluate problems associated with low gravity experiments.

The system being investigated is the K_2O-iron oxide-SiO_2 system. This system is of major interest to the magnetohydrodynamics (MHD) effort, where these oxides are present as components of seed and coal slag.

78

The first portion of this system investigated during the course of this project was compositions on the $KFeO_2$-"Fe_2O_3" binary. Due to the high temperatures involved (T > 1500°C) platinum was chosen as the container material. As a result of this study, it was reported [1] that, contrary to the expected result, platinum was a suitable container at temperatures as high as 1600°C, provided most of the Fe was kept in the 3+ state. Also, the existence of a β'''-alumina structure type phase was reported.

As an extension of this study, selected compositions in the K_2O-iron oxide-SiO_2 system have been examined at lower partial pressures of oxygen, where divalent iron is present.

Experimental Procedures

The preparation of compositions for study and characterization methods following heat treatment has been described [1,2]. The same methods were utilized for this portion of the study, except that all calcinations and heat treatments were performed in controlled partial pressures of oxygen.

In order to provide atmosphere control during heat treatment of specimens, a gas blending and purifying train was assembled. Mass flow-meters were used to establish desired mixing ratios of inert gas (argon), $95N_2/5H_2$, N_2 and O_2. The inert gas was further purified by passing over hot titanium sponge at approximately 800°C when desired. The actual oxygen partial pressure in the furnace atmosphere was continuously monitored using a stabilized zirconia oxygen sensor. The furnace chambers consisted of impermeable high purity alumina tubes provided with suitable metal end fittings for gas flow and temperature measurement, with silicone rubber gaskets.

Because of the lower temperatures involved, the choice of container materials included iron, gold and platinum. The use of iron as a container material must be limited, however, to oxygen pressures determined by the Fe-FeO equilibrium, of the order of 10^{-12} to 10^{-17} atm at the temperatures involved in this study. Gold containers were utilized for heatings at higher oxygen pressures and temperatures up to the 1000°-1050°C range. For heatings above this temperature, platinum containers were used.

Experimental Results

The compositions, temperatures and oxygen partial pressures investigated are shown in Table 1. Selected initial compositions on two joins were examined, the $K(Fe_{.5}Si_{.5})_2$-SiO_2 join in the K_2O-"FeO"-SiO_2 system and the analogous $KFeO_2$-SiO_2 join in the K_2O-Fe_2O_3-SiO_2 system. Thus, all final compositions fall between these bounding planes in the system K-Fe-Si-O. The compositions in the $K(Fe_{.5}Si_{.5})O_2$-SiO_2 join are an extension to lower silica content of the region studied earlier by Roedder [3]. The $KFeO_2$-SiO_2 join has been studied in air by McDaniel [4].

When heated at temperatures of 800°C and oxygen partial pressures of 10^{-6} atm, all compositions on the $K[Fe_{.5}Si_{.5}]O_2$-SiO_2 join yielded a phase similar in structure to the high temperature orthorhombic form of $KFeSiO_4$ previously reported [4,5]. In air, this orthorhombic $KFeSiO_4$ transforms reversibly to a low temperature hexagonal form at about 945°C. Apparently, the reduced oxygen pressure during these experiments increases the stability region of the orthorhombic structure. Reheating in air at

Table 1. Compositions Investigated in the System K_2O-Iron Oxide-SiO_2.

Initial Composition	Temp.[a] °C	Time hr	P_{O_2} atm	Results[b]
$80K(Fe_{.5}Si_{.5})O_2:20SiO_2$	800	24	10^{-6}	phase similar to orthorhombic $KFeSiO_4$ structure
$75K(Fe_{.5}Si_{.5})O_2:25SiO_2$	800	24	10^{-6}	phase similar to orthorhombic $KFeSiO_4$ structure
$2K(Fe_{.5}Si_{.5})O_2:SiO_2$	700	24	10^{-17}	poorly crystalline, orthorhombic $KFeSiO_4$ like phase + SiO_2
	800	37	10^{-6}	phase similar to orthorhombic $KFeSiO_4$ structure
	800	93	air	reheat of preceding specimen, hexagonal $KFeSiO_4$ structure type
$5K(Fe_{.5}Si_{.5})O_2:3SiO_2$	810	32	10^{-6}	phase similar to orthorhombic $KFeSiO_4$ structure
	900	120	10^{-6}	melted, phase similar to orthorhombic $KFeSiO_4$ structure
$4K(Fe_{.5}Si_{.5})O_2:3SiO_2$	800	72	10^{-6}	phase similar to orthorhombic $KFeSiO_4$ structure
$4KFeO_2:3SiO_2$	800	40	10^{-6}	phase similar to orthorhombic $KFeSiO_4$ + Fe_3O_4
	1033	42	10^{-6}	phase similar to Fe_3O_4 + phase similar to orthorhombic $KFeSiO_4$

81

Composition				Phase[b]
$KFeO_2:SiO_2$	800	40	10^{-6}	phase similar to hexagonal $KFeSiO_4$
	1033	42	10^{-6}	phase similar to orthorhombic $KFeSiO_4$ + Fe_3O_4 + unknown
	1015	20	10^{-17}	melted, glass, no crystalline phases present
	1225	72	10^{-6}	melted, phase similar to orthorhombic $KFeSiO_4$
	1350	23	10^{-6}	melted, phase similar to orthorhombic $KFeSiO_4$
$KFeO_2:2SiO_2$	800	40	10^{-6}	$KFeSi_2O_6$-like phase + tr. Fe_2O_3
	1033	42	10^{-6}	melted, unknown phase
$KFeO_2:3SiO_2$	800	40	10^{-6}	melted, SiO_2 + Fe_2O_3 + unknown

a/ All compositions calcined at 600° and 700°C for 80–100 hours with periodic grindings prior to heat treatments shown in table. Compositions containing divalent Fe were annealed in P_{O_2} = 10^{-6}, initial compositions containing only trivalent iron were calcined in air.

b/ Based on microscopic examination and powder x-ray diffraction examination for phase identification.

82

800°C of a sample of $2K(Fe_{.5}Si_{.5})O_2:SiO_2$ previously heated at 800°C in $P_{O_2} = 10^{-6}$ atm (Table 1) resulted in oxidation and formation of the expected hexagonal, low temperature structure of $KFeSiO_4$. Heating at lower partial pressures of oxygen, 10^{-17} atm, showed decomposition of the orthorhombic structure, with the appearance of free SiO_2 in the x-ray diffraction pattern.

Compositions on the $KFeO_2$-SiO_2 join, prepared by calcining in air to yield trivalent iron, showed generally similar results to those initially containing divalent iron in that phases having structures similar to hexagonal and orthorhombic $KFeSiO_4$ were observed after heating at reduced oxygen pressures. The initial composition $4KFeO_2:3SiO_2$ is known [4,5] to have a tetragonal structure in air, at temperatures above 850°C, however, apparently not stable at partial oxygen pressures of 10^{-6} atm. Melting points of compositions on this join are lowered 100°–150°C by heating at the oxygen pressures shown in Table 1 as compared to the same compositions heated in air [4,5].

The use of gold containers for low temperature experiments was generally satisfactory. In cases where melting occurred, minor gold-sample reaction was evident. For temperatures above the gold limit where platinum was used, reaction between the molten specimen and platinum was pronounced. Attempts to prepare homogenous glasses for equilibrium recrystallization experiments at oxygen partial pressures of 10^{-8} atm and temperatures in the 1200°–1400°C range were unsuccessful. Three compositions were tried: $KFe^{+3}SiO_4$, $2K[Fe_{.5}^{+2}Si_{.5}]O_2:SiO_2$ and

$5K[Fe^{+2}_{.5}Si_{.5}]O_2:SiO_2$. Reaction between the platinum containers and the molten specimens was observed in all three compositions. Consider-able embrittlement of the platinum due to iron pickup was evident. In the case of the 1400°C heating, traces of the melt were observed on the outside of the container suggesting diffusion through the container wall.

Conclusion and Discussion

Phase assemblages of selected compositions on the joins $K[Fe_{.5}Si_5]O_2-SiO_2$ and $KFeO_2-SiO_2$ have been determined after heat treatment of specimens at oxygen partial pressures of 10^{-6} and 10^{-17} atm. The use of gold as a container appears to be suitable for lower temperatures where no liquid is present. Attempts at higher temperatures to prepare homogenous glasses for equilibrium recrystallization experiments were unsuccessful due to excessive reaction between the platinum container and ferrous iron in the melt at these oxygen pressures.

Discussions with Dr. Oran of MSFC have shown that it is not feasible to acoustically levitate in a 1-g environment and simultaneously heat specimens of these materials to the required temperatures, either for preparation of homogenous glasses or for melting point studies. An alternate technique is the use of aerodynamic jet levitation and it is suggested that this possibility be explored further.

A comparison of experimental conditions and requirements for con-ventional and containerless phase equilibria studies as well as anticipated problem areas are given in Tables 2 and 3.

Table 2. Comparison of Experimental Conditions for Phase Equilibria Studies.

	CONVENTIONAL	CONTAINERLESS
Specimen	Pre-reacted, powder, packed into tube, tube sealed. Mass ⩠0.1 to 0.3 g	Pre-reacted powder, formed into sphere or right cylinder. Mass ⩠0.1 to 0.3 g
Maximum Heating Rate	No restrictions, plunge into hot furnace	Limted only by thermal stress resistance of specimen
Temperature		
A. Measurement	Thermocouple or optical pyrometry ±1° to ±5°C	Two color pyrometry or non-contacting method
B. Control	±2° to ±5°C	Better than ±25°C at final temperature
C. Time at Temperature		
1. Subsolidus Experiments	hrs to days	Not feasible at present
2. Solidus and Liquidus Determination	Minutes to 1-2 hrs after isothermal equilibrium	Minutes to 1 hr after isothermal equilibrium
Cooling Rate	Quench into water	As rapidly as possible
Characterization and Evaluation	In all cases, specimens are examined post-test by optical and scanning electron microscopy and x-ray diffraction to determine phase assemblage, partial or complete melting. Where appropriate, chemical analyses of specimens are performed.	

Table 3. Some Problem Areas Associated with Containerless Experiments.

1) Heating technique for 1300° - 1800°C range

    1) radiant wall furance

    2) laser

    3) arc-image furnace

2) Temperature measurement and control

    1) two-color pyrometer

    2) other non-contacting method

3) Thermal gradients in specimen must be as small as possible

4) Changes in bulk composition of specimen must be measured or estimated from vapor pressure measurements

5) Density of specimen will change with sintering and melting during experiment

6) Electrical conductivity will vary with both temperature and composition

In the case of low gravity experiments, electromagnetic positioning is an alternate technique applicable to a more limited class of oxide materials. As part of an investigation in the area of refractory oxides having good electronic conductivity, a group of NBS investigators has recently reported [6] conductivities as high as 1 $ohm^{-1}cm^{-1}$ in the 100°-250°C range in calcium-doped yttrium chromites. Melting points are in excess of 1750°C, making the choice of container material severely limited for high temperature property measurements. The conductivities appear to be large enough to make electromagnetic positioning feasible.

References

1. J. R. Manning, NBS: Properties of Electronic Materials, NBSIR 79-1767, pp. 82-95, June 1979.

2. J. R. Manning and R. L. Parker, NBS: Properties of Electronic Materials, NBSIR 78-1483, pp. 84-100, June 1978.

3. E. Roedder, Am. J. Sci. (Bowen Volume), pp. 435-456 (1952).

4. C. L. McDaniel, unpublished work.

5. R. S. Roth, Advances in Chemistry Series "Solid State Chemistry: A Contemporary Overview", to be published.

6. T. Negas, W. R. Hosler and L. P. Domingues, Proc. Saint-Vincent Conf. on Energy and Ceramics, Faenza, Italy, May 1979.

Task 4

Thermodynamic Properties of Refractory Materials
at High Temperatures

Jack H. Colwell

Chemical Thermodynamics Division
Center for Thermodynamics and Molecular Science

Summary

The current status of the program to obtain high temperature (1500-4000 K) heat capacities of materials while they are levitated in a space environment is presented. The heat capacities are to be derived from the simultaneous measurement of the radiant heat loss and the rate of temperature change of spherical samples as they cool freely. Details of the thermal gradients to be expected in both metallic and nonmetallic samples have been examined. In metallic samples the gradients, in general, will be tolerably small and cause little difficulty. In nonmetallic samples the gradients will be large but by making measurements on samples of different size, it should be possible to get moderately precise values of both the heat capacity and the thermal conductivity. The upper temperature limit of the experiments will be determined by sample vaporization and will occur when the vapor pressure reaches the vicinity of 10 Pa (10^{-4} atm). The program for a ground-based simulation of the free-cooling experiment is discussed.

Introduction

The purpose of this research is to measure the heat capacities of refractory materials at high temperatures, 1500–4000 K, by using the low-gravity environment of space to maintain the samples without physical contact. The samples will be spherical, fabricated in that form as solids and maintained in that form as liquids by their surface tension. They will be heated to a high temperature and then allowed to freely cool by radiation in a cold-walled vacuum chamber.

As the sample cools its temperature will be determined by radiation pyrometry and the total radiative heat loss will be determined simultaneously using a wide-band pyroelectric detector. The ratio of the heat loss to the rate of change of temperature will be a measure of the heat capacity.

To give an indication of the nature of the experiment, two pertinent quantities are presented in Fig. 1. The rate of cooling of a sphere by radiation is obtained, assuming no thermal gradients, by equating the rate of heat loss

$$dH = -4\pi R^2 \epsilon\sigma T^4 dt \tag{1}$$

with the thermal capacity

$$dH = (4/3)\pi R^3 c\rho dT \tag{2}$$

which yields

$$dT/dt = -3\epsilon\sigma T^4/(c\rho R). \tag{3}$$

ϵ is the total hemispherical emissivity, σ the Stefan-Boltzmann Constant, c the specific heat and ρ the density. In Fig. 1 the rate of cooling as a function of temperature is shown for a sphere of radius R = 0.5 cm with values of ϵ and ρc typical of refractory metals. For the region of interest the rate varies quite widely, from 20 K/s to nearly 1000 K/s. Since it is

reasonable to consider measurements on samples as small as 1 mm radius, the inverse dependence on the radius, Eq. (3), would lead to cooling rates as high as 5000 K/s. The detectors will be operating at frequencies of about 1 kHz, so the temperature will not be changing appreciably during the sampling period even for the highest cooling rate. Depending on sample size, the free-cooling period will last between about 5 and 30 seconds for coolings to 2000 K and considerably longer for coolings extending below that temperature.

The total power radiated by the sample, as shown in Fig. 1, gets quite large at the highest temperatures and will, of course, be even larger for larger samples or ones with higher emissivities. At these levels, the heating of specimens to the desired temperature will become a major problem. For metals, inductive heating will be the principal source, but to reach the highest temperatures it may have to be supplemented with a radiative source. Nonmetals will almost certainly require supplementary heating. The large amount of power being radiated by the sample, however, will simplify considerably the determination of that power at a distance. As a result, there should be no problem with signal level except possibly for the pyroelectric detectors with very small samples at the lowest temperatures.

We foresee no insurmountable obstacle to the free-cooling experiments from the physical measurement aspect, that is, the radiation pyrometry measurement or the measurement of total radiant power with pyroelectric detectors. Some of the problems in making these measurements have been pointed out in an earlier report[1] and are further discussed in this report. The real limitation to the free-cooling experiments arise from the experimental approach. Because of the rapid cooling of the samples, temperature gradients will exist in the samples and for those of low thermal conductivity

will be quite large. At some point these will make it impossible to extract

meaningful data from the measurements. We have spent considerable effort

in the determination of the temperature gradients likely to be encountered

in the experiments and what information can be extracted. The vaporization

and/or decomposition of the sample will determine the maximum temperatures

which can be reached in these experiments. Both of these limitations on

the applicability of the experiments will be discussed as well as the

current plans for future development.

Temperature Gradients

The thermal gradients within a sphere, freely cooling by radiation,

are given by the Fourier equation

$$\frac{\partial^2 T}{\partial r^2} + \frac{2}{r}\frac{\partial T}{\partial r} = \frac{1}{\alpha}\frac{\partial T}{\partial t} \tag{4}$$

with the thermal diffusivity $\alpha = \lambda/\rho c$, λ being the thermal conductivity and

ρc the density times the specific heat, i.e., the heat capacity per unit

volume. Solutions to Eq. (4) must satisfy the boundary condition

$$\lambda\frac{\partial T}{\partial r} = \epsilon\sigma T^4 \quad \text{at} \quad r = R, \tag{5}$$

where $\lambda\ \partial T/\partial r$ is the heat conducted to the surface of the sphere which must

equal the heat radiated from the surface given by the Stefan-Boltzmann

relation $\epsilon\sigma T^4$. The T^4 term in the boundary condition, Eq. (5), makes the

equation nonlinear and it cannot be solved analytically. Solutions to this

problem have been obtained by other workers[2,3] using the numerical method

of finite differences, but their results are not available to us in a

usable form. We are fortunate in having two generalized programs in the

NBS computer library for the numerical solutions of nonlinear partial

differential equations. The programs are MOL1D (method of lines, one dimension)[4] and PDECOL (partial differential equations, collocation over piecewise polynominals)[5]. The MOL1D program can be used to produce tabulated temperature values at various radii for a given set of times. We have used this program in generating the data discussed below. The program can be made very general in allowing for various initial temperature gradients and for different temperature dependences of the physical parameters, c, ρ, ε, and λ. The results are somewhat awkward to use in that one cannot conveniently generate data for different input parameters at the same temperatures. The PDECOL program produces a polynomial solution which may be better suited for this purpose but it has not been run to date.

To describe and understand the temperature gradients in free-cooling spheres it has been extremely useful to define what we term the "limiting parabolic temperature distribution." Once a cooling sphere has this limiting distribution, its form will be maintained for the rest of the cooling cycle. To derive this limiting temperature distribution we assume first, that a gradient exists and second, that the gradients do not change as the sample cools. The second assumption is not strictly true, of course, and will be modified subsequently. In Fig. 2 we define the quantities describing the heat flow from a sphere; Q is the power radiating from the surface of the sphere of radius R, and q is the heat flux across a surface within the sphere at radius r. If all parts of the sphere are cooling at the same rate, and assuming that c, ε, and λ are all independent or only weak functions of T, then

$$q = \frac{4\pi r^3}{4\pi R^3} Q = \frac{r^3}{R^3} Q. \tag{6}$$

This equation simply states that as the sphere cools, each volume element

gives up the same amount of heat and that all the heat must be conducted to the surface at R. For q to be conducted across the surface at r, the temperature gradient at r must be such that

$$q = -4\pi r^2 \lambda \frac{dT}{dr}. \qquad (7)$$

Q is given by the Stefan-Boltzman relation

$$Q = 4\pi R^2 \epsilon \sigma T_s^4 \qquad (8)$$

where T_s indicates the surface temperature.

Substituting (7) and (8) into (6) we have

$$dT = -\frac{\epsilon \sigma T_s^4}{\lambda \Theta} r dr, \qquad (9)$$

and integration from r to R yields

$$T(r) = T_s [1 + \frac{\epsilon \sigma T_s^3}{2\lambda R}(R^2 - r^2)]. \qquad (10)$$

The temperature at the center of the sphere relative to that at the surface is

$$\frac{T(o)}{T_s} = [1 + \frac{\epsilon \sigma T_s^3 R}{2\lambda}], \qquad (11)$$

the temperature difference being

$$\Delta T = T(o) - T_s = \frac{\epsilon \sigma T_s^4 R}{2\lambda} \qquad (12)$$

These equations are accurate when the temperature difference, ΔT, is only a few percent of T_s, but not for large values. Eq. (12) shows that the temperature difference is diminishing as T_s drops whereas the initial assumption in Eq. (6) was that the difference was constant. To be correct, the temperature at the center of the sphere must drop more than the temperature at the surface. Therefore, q in Eq. (6) must be proportionately larger toward the center of the sphere by an amount which varies with r and T much as $T(r)/T_s$. We have found that modifying Eq. (6) so that

$$q = [T(r)/T_s]^2 \frac{r^3}{R^3} \quad Q = [1 + \frac{\varepsilon\sigma T_s^3}{2\lambda R}(R^2-r^2)]^2 \frac{r^3}{R^3} Q, \qquad (13)$$

solving for a new $T(r)/T_s$ using Eqs. (7) and (8), and by iterating repeatedly, one obtains

$$T(r) = T_s[1 - \frac{\varepsilon\sigma T_s^3}{2\lambda R}(R^2-r^2)]^{-1} \qquad (14)$$

which closely fits the computed results.

In Fig. 3 we compare the temperature distributions derived from the partial differential equation (solid lines) with the predicted limiting parabolic distributions (dashed lines). We have assumed an initial condition of uniform temperature at 3000 K. The material parameters are λ = 1.0 W/cm·K, ρc = 3.0 J/K·cm^3, and ε = 0.3, values that correspond to tungsten and are relatively typical of most refractory metals. When the sphere initially starts to cool, the surface temperature drops rapidly until the temperature distribution within the sphere becomes parabolic and then the entire sphere commences to cool uniformly. This system reaches the limiting parabolic distribution in slightly over 0.5 seconds and after the temperature has fallen only about 2 1/2%. It is interesting to note that the limiting temperature distribution depends only on the thermal conductivity and not on the heat capacity. Once the limiting distribution is established, the heat capacity determines the rate of cooling only. The solution of the partial differential equation is needed to describe how the initial conditions die away and at what point the limiting parabolic behavior is applicable.

Shown in Fig. 4 are results for spheres of three different radii for a hypothetical nonmetal where the material parameters, λ = 0.046 W/cm·K, ρc = 4.6 J/K·cm^3, and ε = 0.3, are similar to those of solid alumina. The initial condition is again a uniform temperature of 3000 K and the material parameters are considered to be independent of temperature. In the figure

the time variable is reduced by dividing by the radius of the spherical specimen (see Eq. (3)) which permits a better comparison of the effect of the radius. We see that initially the surface temperature of the larger samples falls more rapidly (on our reduced time scale) until the limiting parabolic gradient is reached. The limiting distributions for the spheres are reached when t/R is approximately 3, 6, and 12 s/cm for the 0.125, 0.25, and 0.5 cm radii, respectively. At $t/R = 20$ the surface temperatures are nearly identical and the proportionality of the temperature differences to the radii is obvious. That the three surface temperatures are the same at this time is only coincidental, for once the samples have achieved the limitng parabolic distribution, the surface temperature of the smaller sphere is always cooling faster (in t/R units) than the larger sphere. This is a consequence of the initial rapid cooling of the surface of the larger sphere, so that it was losing proportionately less heat during subsequent periods than the smaller sphere. As a result, the average temperature of the larger sphere will always be greater than that of the smaller sphere. At lower temperaures, when the temperature gradients are small, the surface temperature of the larger sphere will be higher than that of the smaller sphere.

The magnitude of the change in the apparent heat capacities caused by the temperature gradients can be readily calculated when the gradients have the limiting parabolic form. The observed temperature change during a given time interval is that of the surface temperature, T_s. The heat evolved during that interval, however, will depend on the change in the average temperature of the sample. The change in this average temperature, T_{av}, on cooling will always be greater than the change in T_s because of the diminishing gradient with diminishing temperature. As a result, the apparent heat capacity, i.e., the observed energy radiated divided by the change in T_s, will always be greater than the actual heat capacity. The average

temperature for a sphere as determined by

$$T_{av} = \frac{1}{(4/3)\pi R^3} \int_o^R 4\pi r^2 T(r)\,dr, \tag{15}$$

and using Eq. (14) for T(r) gives

$$T_{av} = \frac{3T_s}{bR^3}\left[1 - \frac{1}{\frac{b}{a}R}\tan^{-1}\left(\frac{b}{a}R\right)\right], \tag{16}$$

where $a = 1 - \varepsilon\sigma T_s^3 R/(2\lambda)$ and $b = \varepsilon\sigma T_s^3/(2\lambda R)$.[6]

In Table 1, changes in T_{av} are given for each of two different radii, conductivities and surface temperatures. The results show that the increase in the apparent heat capacity over the actual varies, as might be expected,

Table 1. Changes in T_{av} relative to changes in T_s for spheres of two different radii and two different thermal conductivities including the percentage increase in the apparent heat capacity over the actual heat capacity

λ(W/K·cm)	T_s(K)	ΔT_s	R = 0.25 cm			R = 0.5 cm		
			T_{av}	ΔT_{av}	%ΔC	T_{av}	ΔT_{av}	%ΔC
0.1	3000 2950	50	3071.24 3016.50	54.74	9.5	3147.58 3087.49	60.09	20.2
0.1	2500 2450	50	2533.87 2481.20	52.65	5.3	2569.09 2513.57	55.52	11.0
1.0	3000 2950	50	3006.91 2956.46	50.45	0.9	3013.87 2962.96	50.91	1.8
1.0	2500 2450	50	2503.33 2453.07	50.26	0.5	2506.67 2456.15	50.52	1.0

linearly with R, inversely with λ, and as the temperature cubed. The increases found for λ = 0.1 W/K·cm are distressingly large for the conductivities of most

nonmetals will lie at or below this value. The conductivities of refractory metals tend to lie between about 0.3 and 1.2 W/K·cm, so the increase in apparent heat capacity will be sizable even for many metals.

Because the heat capacity increase is nearly an exact linear function of the sample radius, it should be a relatively simple matter to correct for the increase by measuring samples of different size. Indeed, when the apparent heat capacity increase is large, it should be possible to determine thermal conductivities from a set of precise data. This process could be appreciably complicated by the temperature dependence of c, λ, and ε; these quantities were taken as constants in the above analysis, but they are usually relatively weak functions of T. This will work for solids but may break down completely for liquids if there is any stirring of the sample. If a sample is heated inductively, appreciable stirring action will occur during the heating period which may take time to die away. If a sample were radiantly heated in a low-gravity environment it may remain quiescent, but this will have to be determined. It is our intention, however, to use induction coils, operating at low power levels, to electro-magnetically position the samples within the apparatus. This action alone would probably add some stirring action to a liquid sample.

Sample Vaporization

In the high-temperature levitation calorimetry carried out by David Bonnell with John Margrave,[7] the upper temperature limit of the experiments was determined by the vaporization of the refractory metal samples. In their case, the samples were in an inert-gas atmosphere and the vaporizing atoms condensing into a smoke which physically obscured the sample. This occurred at vapor pressures of about 10 Pa, which, in general, corresponds to temperatures about 200 K above the melting point of the metals.

97

The free-cooling experiments will be in a vacuum so there will not be any smoke formation; sample vaporization, however, will still cause difficulties and determine the high temperature limit for the experiments. Assuming the evaporation coefficient for metals to be $\mu = 1$, the rate of evaporation at 10 Pa will be about $W = 10^{-3}$ g/cm^2·s. Using a sample density of $\rho = 12.5$ g/cm^3, the rate of sample loss will be $W/\rho = 8 \times 10^{-5}$ cm/s. As a fraction of the total sample, this will be $F = W4\pi R^2/(4/3\pi R^3\rho) = W/(R\rho) = 8 \times 10^{-5}/R$ s^{-1}. For R between 0.1 and 1 cm the loss will be less than 0.1%/s and can probably be ignored. This vaporizing material will, however, be condensing on the apparatus. Consider a detector or detector objective lense 10 cm from a sample of R = 0.5 cm, the rate of deposition of the metal coating on these objects will be about 2 nm/s. This may seem a small amount but considering that an opaque metallic coating has a thickness of about 50 nm, indicates that the detectors will have to be protected if exposed to samples vaporizing at these rates for periods of a few seconds or more.

The heat loss from a sample will be significant at vapor pressures of 10 Pa. Using $\Delta H_v = 750$ kJ/mol for the heat of vaporization of refractory metals,[8] and $V_m = 10$ cm^3/mol as the molar volume, the power of heat loss by vaporization at a vapor pressure of 10 Pa is $P_v = W\Delta H_v/(\rho V_m) = 6$ W/cm^2. In Table 2, P_v is compared with the radiative power, P_R, for surfaces at three different temperatures.

Table 2. Power of evaporative heat loss (vapor pressure = 10 Pa) compared with radiative power ($\varepsilon = 0.3$) at various surface temperatures

T(K)	P_v(W/cm^2)	P_R(W/cm^2)	P_v/P_R x 100(%)
2000	27	6	22
3000	·137	6	4.4
4000	435	6	1.4

It is apparent that with samples at temperatures where the vapor pressure is 10 Pa, a significant correction will have to be made for sample vaporization, and for those sample materials reaching that pressure at low temperatures, the correction will have to be of fairly high accuracy.

There are also potential problems from the sample vapor due to its absorption spectrum. Nearly all materials will have absorption bands in the region of interest, 0.3 μm to 15 μm for the total radiance measurement. The atomic absorption lines of metal vapors will probably remain sharp up to pressure of 10 Pa and block out very little of the total radiation. Above that pressure, however, the lines will begin to broaden and an appreciable amount of radiation from the sample would be blocked from the detector. For the radiation pyrometry, which will use narrow bandwidths between 0.4 and 1 μm, care will have to be taken that absorption lines do not occur at the wavelengths being used.

This discussion on vaporization has been restricted to metals because of the availability of data and the generalizations that can be made. The same type of problems and limitations will occur with nonmetallic samples and will probably be much more involved and stringent. The evaporation coefficient will most likely be less than 1 and vaporization can be accompanied by dissociation of the molecular species so that quantities such as rates and heats of vaporization are less well defined. Molecular species in the vapor will make the absorption spectrum much more complex with numerous broad absorption bands. Finally, if decomposition is occurring at the surface, the radiative properties of the surface could be altered considerably and introduce errors in interpretation of the radiation measurements.

Total Radiance Measurement

The unique aspect of the free-cooling experiment and that with least
precedent, is the proposal to use pyroelectric detectors to measure the
total radiant heat loss from the sample. The detectors must be uniformly
black over the wavelength 0.4 to 14 μm which will include 99% of the radiation
from samples at temperatures between 1500 and 4000 K. When the field of
view of the detector encompasses the entire sphere of the sample, the
signal will be proportional to the total hemispherical emittance,[1] the
proportionality will be the area of the detector relative to the area of
the sphere whose radius is the distance from the detector to the center of
the sample.

A pyroelectric is a poled ferroelectric, which, when heated, changes
its spontaneous polarization. LiTaO$_3$ detectors will be used because the
883 K Curie temperature of this material makes it well suited for a high
temperature apparatus and they are available in a wide range of products
from several manufacturers. A pyroelectric detector has electrodes on two
sides of a thin wafer of material forming a capacitor, a change in polarization
of the material can then be used to generate a current in an external
circuit. The current is proportional to the rate of change of temperature
so that radiation from a continuous source must be chopped to get useable
response. A black coating is applied to the front surface of the pyroelectric
to enhance the light absorption and the back surface is bonded to the
mounting which serves as a heat sink. Fig. 5 shows the thermal response of
an idealized pyroelectric detector. The diagram at the top of the figure
describes the model used; P is the power of the incident radiation, c is
the thermal capacity of the pyroelectric which is at temperature T, h is
the thermal conductance to the heat sink at T_o. The response of the model

100

is given by

$$\frac{P - h(T-T_o)}{P - h(T_i-T_o)} = e^{-\frac{h}{c}t} \tag{17}$$

which is plotted as curve A in Fig. 5 with P = O and the initial temperature,
$T_i > T_o$ and as curve B with P = P and $T_i = T_o$.   The thermal response of the detector
to chopped radiation is represented by the saw-toothed curve which rises from T_o when
the radiation is turned on until reaching a steady state. At the steady
state, the temperature of the pyroelectric will be following the path
indicated by the arrows at the intersection of curves A and B in Fig. 5.
For this idealized example, the electrical response will be a square wave
when the chopping period is sufficiently small compared with the thermal
relaxation of the device, $\tau = c/h$. As the chopping period is made longer,
the curvature in the thermal response will become more evident and the
square wave will begin to droop.

The model for the thermal response is idealized in several ways.
Foremost is that the model implies that the pyroelectric is uniformly
heated whereas it actually responds to the thermal pulse as it propagates
through the material. Also, the black coating introduces a thermal lag
which together with electrical response of the circuit produce a sizable
rise-time for the device. Fig. 6 shows oscilloscope tracings of the response
of a pyroelectric detector at four different chopping frequencies. At 300
Hz the rise time of the response is very evident but part of this is due to
the transition period of the chopper. The constant voltage period is
somewhat less than a millisecond. At 150 Hz the voltage is essentially
constant for more than 1 1/2 ms. At 75 Hz the droop in the voltage signal
is evident and from the 15 Hz curve the thermal time constant for the
device of 15-20 ms can be deduced. It was intended that this particular

detector could be used at 300 Hz with the voltage sampled for 1 ms during each half cycle. The 300 Hz curve in Fig. 6 shows that either the sampling period or the chopping frequency will have to be reduced to get the full signal.

Gold black is used for the absorptive coating on the pyroelectric detectors and numerous reflectance measurements have shown these coatings to be uniformly black to between 98 and 100% for wavelengths from 0.3 to 10 μm. Beginning between 10 and 20 μm there is a drop-off to values as low as 90% with the position of the drop-off varying from sample to sample. At wavelengths above 10 μ, however, we are concerned only with the long wavelength tail at the lowest temperature so the errors introduced should be small. Because of the smallness of the detectors and the degree of difficulty in making accurate reflectance measurements, the blackness of individual detectors cannot be determined directly and must be assumed to be similar to the measured coatings.

The calibration of the pyroelectric detectors will present some difficulties. The response of the detectors are supposed to be linear over the range of power to be covered by the experiments for samples of 0.1 to 1 cm radius and temperatures from 1500 to 4000 K. The linearity and magnitude can be established to a fair degree of precision using standard tungsten filament lamps. There will be, however, uncertainties of several percent arising from the transfer of the calibration as well as the original lamp calibration itself.

Current Experimental Plan

Because of the untried nature of the pyroelectric detection system in particular and the free-cooling experiment in general, we are proceeding

with a ground based simulation of the space experiment. The setup to be used is shown in Fig. 7 where in place of the sample being levitated within the apparatus, it is simply suspended from a wire of the same material. Tungsten is the material of choice since with its high melting point, 3650 K, experiments could probably be run at temperatures up to 3500 K or, as is more likely, up to the limit of the available power for induction heating. The heat capacity and emittance are reasonably well known for solid tungsten so that the observed results for the free-cooling of the sample can be compared with calculated results. The correction for the heat leak to the suspension wire will probably be relatively small and, in any case, it can be minimized by electrically heating the wire. A hole drilled in the sample can be used for blackbody temperature measurements so that it will not be necessary to rely on any assumptions about the surface emittance in order to determine the sample temperature. The simulated experiments will allow investigation of many of the problem areas such as reflected light getting into the wide aperture of the pyroelectric detector and light reflected from the coils back onto the sample.

A high-speed, 12 bit, digital voltmeter will be used to record the amplified pyroelectric detector signals. The unit is controlled and the data logged by a desk-top computer. Pyrometry will initially be carried out with an existing millisecond pyrometer, but we are about to start designing a new pyrometer which will be dedicated to the free-cooling experiments. The pyrometer will be a two or three color instrument sampling at millisecond intervals. Control and data logging will be handled by the same system used for the pyroelectric detector.

Conclusions and Discussion

The upper temperature limit of the free-cooling experiments will be limited by the vaporization of the sample. This will occur when the vapor pressure of the material reaches the vicinity of 10 Pa.

For nonmetals there will be problems from numerous sources. The low electrical conductivity may preclude inductive heating and limit the ability to use radio frequency fields for positioning the samples. The transparency of some nonmetallic materials will cause difficulties in temperature determinations[1]. Temperature gradients, determined by the thermal conductivity of the material, will limit the precision of the derived physical quantities. For $\lambda < 0.01$ W/K·cm, it may be difficult to extract any meaningful results from the data. For $0.01 < \lambda < 0.1$ W/K·cm, it should be possible to obtain both heat capacities and thermal conductivities of moderate precision for solid samples. For $\lambda > 0.1$ W/K·cm, relatively precise heat capacities should be obtained together with a low precision value of λ, again for solid samples. Meaningful data on liquid samples with λ much below 1 W/K·cm could only be obtained in the limits of rapid stirring or no stirring. It will probably not be possible to derive heats of fusion from the cooling curves of poorly conducting materials.

With metals, vaporization of the sample appears to be the only impediment to heat capacity measurements by the free-cooling technique. The high thermal conductivity of the samples will keep the gradients small enough that stirring within liquid samples will produce only a minor perturbation on the measurements. It is unfortunate that with few exceptions (Hf, Zr, and Pt), the vapor pressure of high-melting metals will limit the experiments to temperatures just slightly above their melting points, because it would be of great value to obtain the heat capacities of liquid metals over a

wide temperature range. The free-cooling experiments do, however, open a new prospect; to measure the heat capacities of the liquid metals into the supercooled range. Containerless samples should, and have been observed[9] to, supercool to a considerable extent. The free-cooling experiment will permit the heat capacity to be determined all the way to the point where solidification commences and the sample recalesces. It will also be possible to change the sample size and thus the rate of cooling, which may produce variations in the extent of supercooling and even possibly the heat capacity. The prospect of the supercooling experiments with metals makes the development of the free-cooling technique worthwhile even if the determination of nonmetal heat capacities were to turn out to be infeasible.

References

[1] J. H. Colwell, NBSIR 79-1767, NBS: <u>Properties of Electronic Materials</u>,
     J. R. Manning, Ed., p. 103.

[2] D. L. Ayers, J. Heat Trans., Trans. ASME <u>92</u>, 180 (1970).

[3] G. Wouch, E. L. Gray, R. T. Frost, and A. E. Lord, Jr., High Temp.
     Sci. <u>10</u>, 241 (1978).

[4] J. M. Hyman, The NYU Report-Method of Lines Solution of Partial
     Differential Equation, Oct. 1976, or contact James M. Hyman, Group
     T-7, Mail Stop 233, Los Alamos Scientific Laboratory, Los Alamos, New
     Mexico 87545.

[5] N. K. Madsen and R. F. Sincovec, ACM-TOMS <u>5</u>, 326 (1979).

[6] Using Eq. (10) as an approximation for T(r), a much simpler expression
     is obtained for T_{av}:
     $$T_{av} = T_s + \frac{2}{5}\left(\frac{\varepsilon\sigma T_s^4 R}{2\lambda}\right)$$

[7] David W. Bonnell, Ph.D. Thesis, Rice University, Houston, Texas (1972).

[8] S. Dushman and L. R. Koller, <u>Scientific Foundations of Vacuum Technology</u>,
     2nd Edition, S. Dushman and J. M. Lafferty, Eds. (Wiley, N.Y., 1962),
     Chap. 10; R. E. Honig, <u>The Characterization of High-Temperature Vapors</u>,
     John L. Margrave, Ed. (Wiley, N.Y., 1967), Appendix A.

[9] D. W. Bonnell and W. J. Boettinger, private communications.
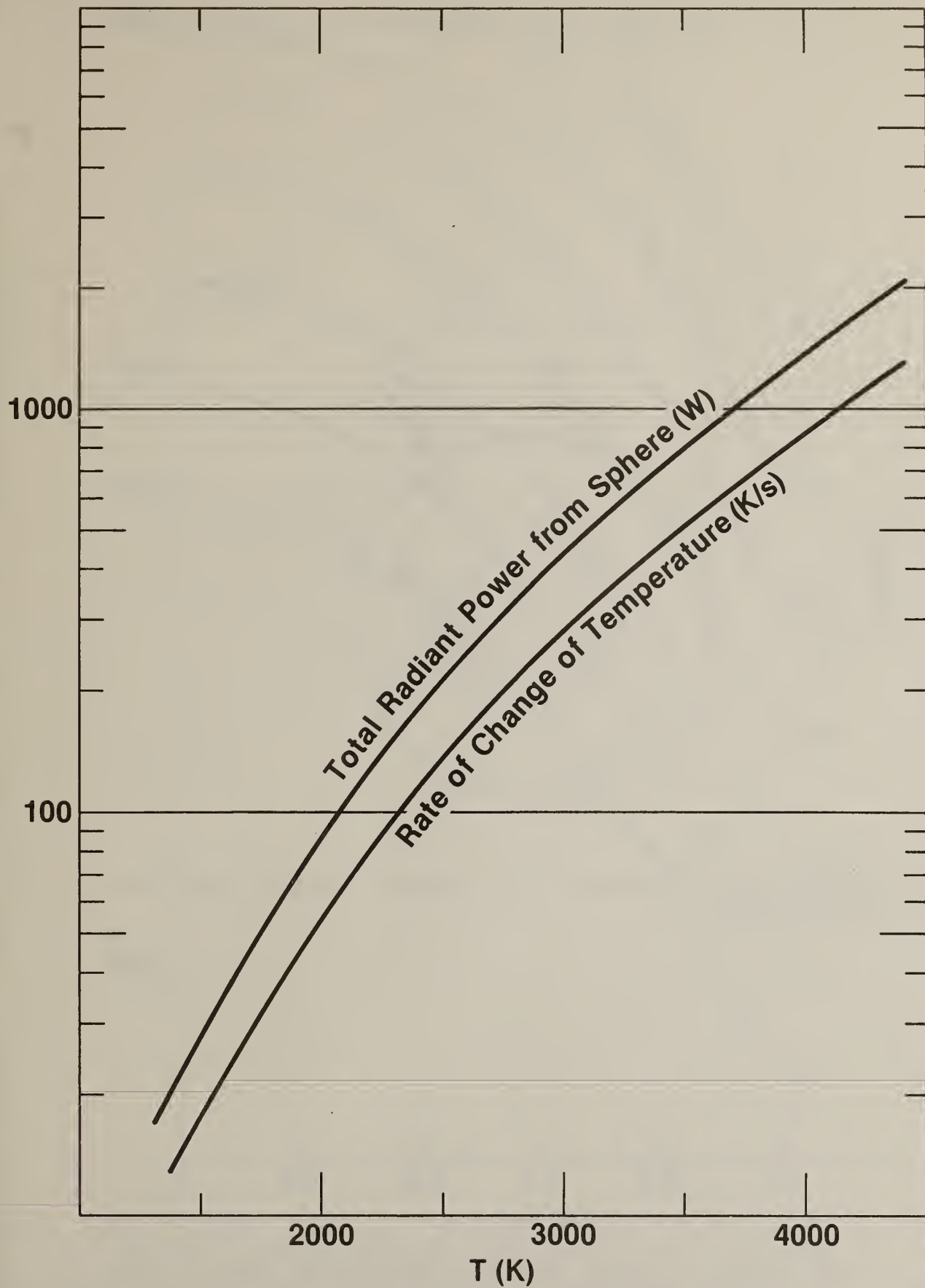
Fig. 1. The rate of temperature change and total radiant power for a
free-cooling 1 cm sphere of refractory material, $\varepsilon = 0.3$,
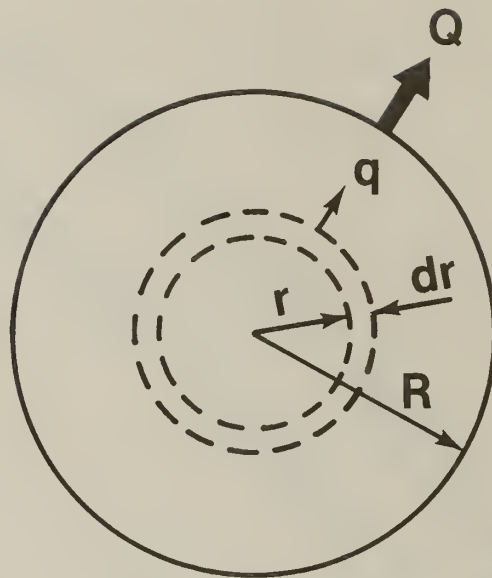$\rho c = 3.0$ J/K·cm³.

107

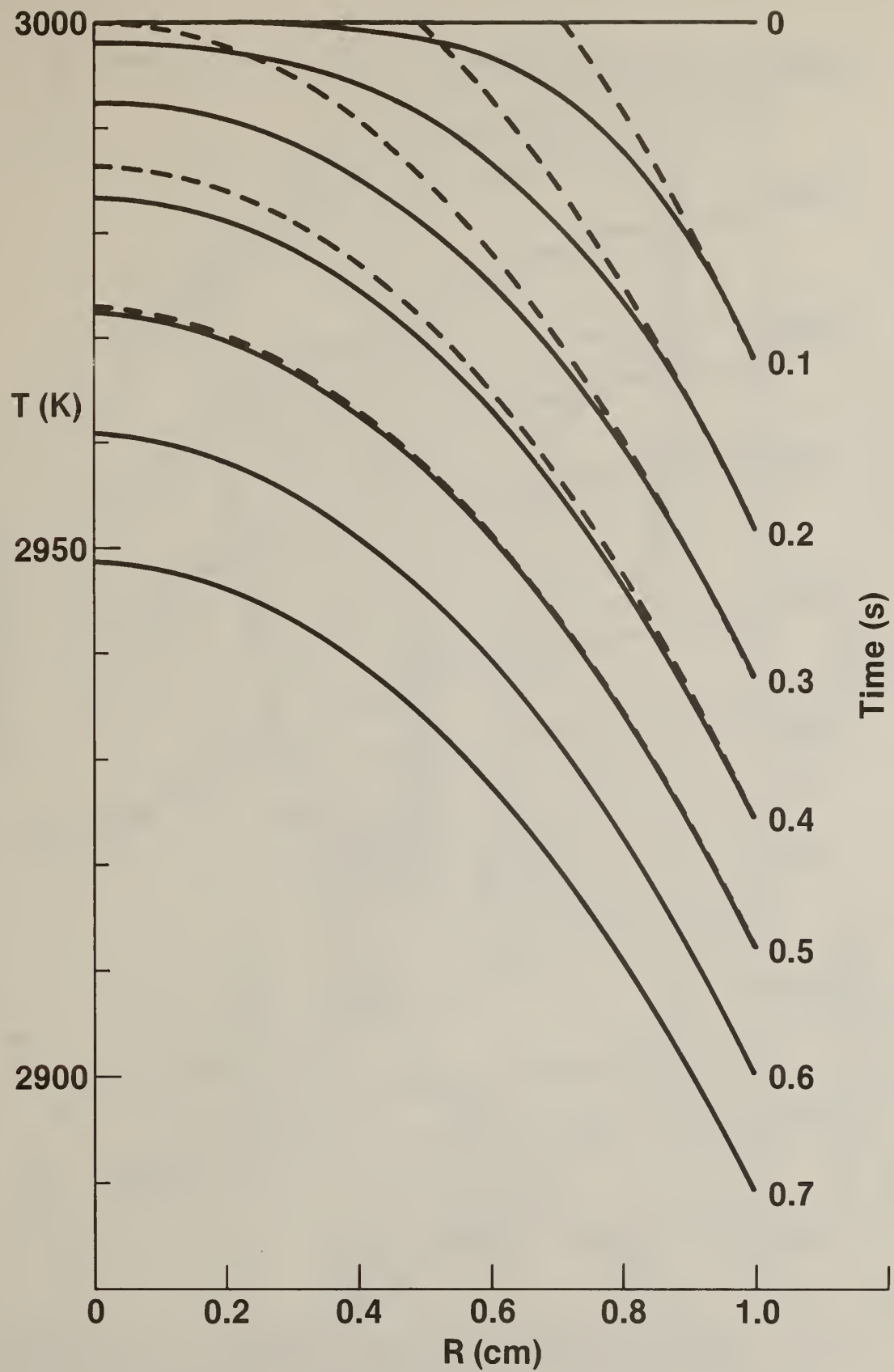Fig. 2. Diagram for the derivation of the limiting parabolic temperature distribution.

Fig. 3. Temperature gradients in a sphere of 1 cm radius freely cooling by
radiation from an initial constant temperature of 3000 K. The
material parameters, $\varepsilon = 0.3$, $\rho c = 3.0$ J/K·cm^3, and $\lambda = 1$ W/K·cm
correspond closely to those of tungsten. The solid curves are
solutions of the partial differential equation describing the system.
The dashed curves are the limiting parabolid temperature
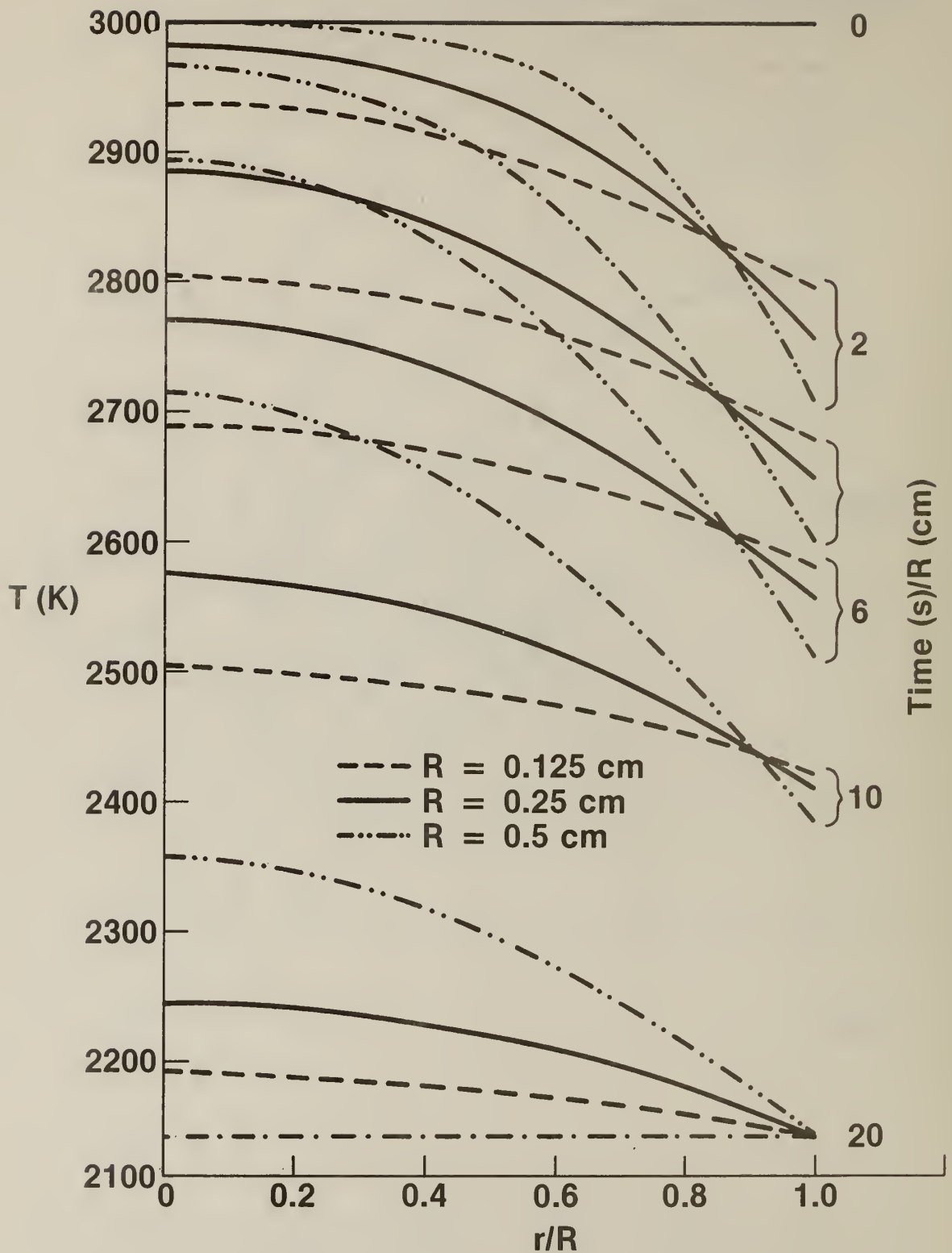distributions for the same surface temperatures.

109

Fig. 4. Temperature gradients in freely cooling spheres of three different
radii of a hypothetical material with $\varepsilon = 0.3$, $\rho c = 4.6$ J/K·cm^3 and
$\lambda = 0.046$ W/K·cm. The initial condition is a uniform temperature
of 3000 K. The dash-dot line at the bottom is a reference line to
highlight the direct proportionality of the magnitude of the
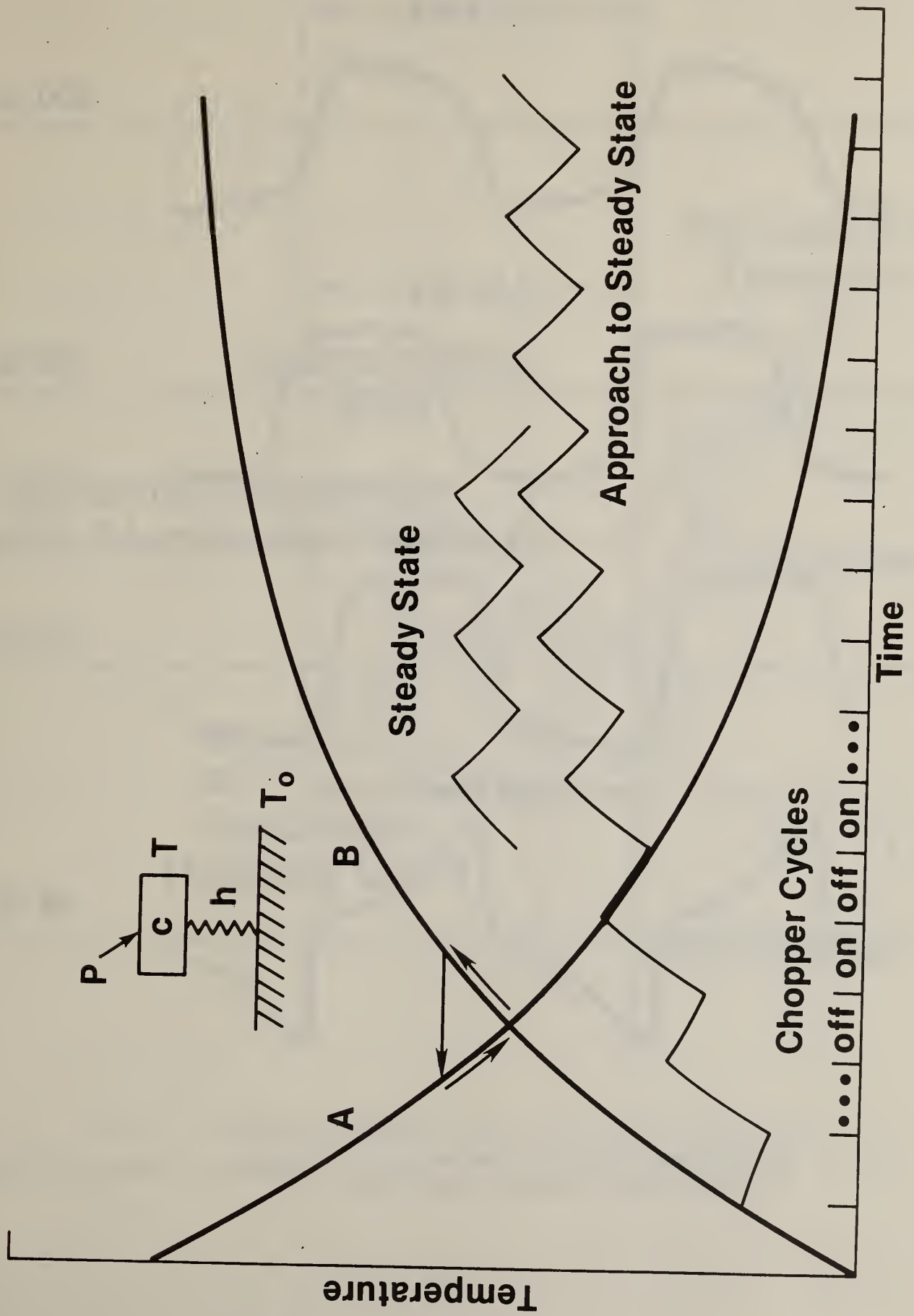gradients to the radii.

110

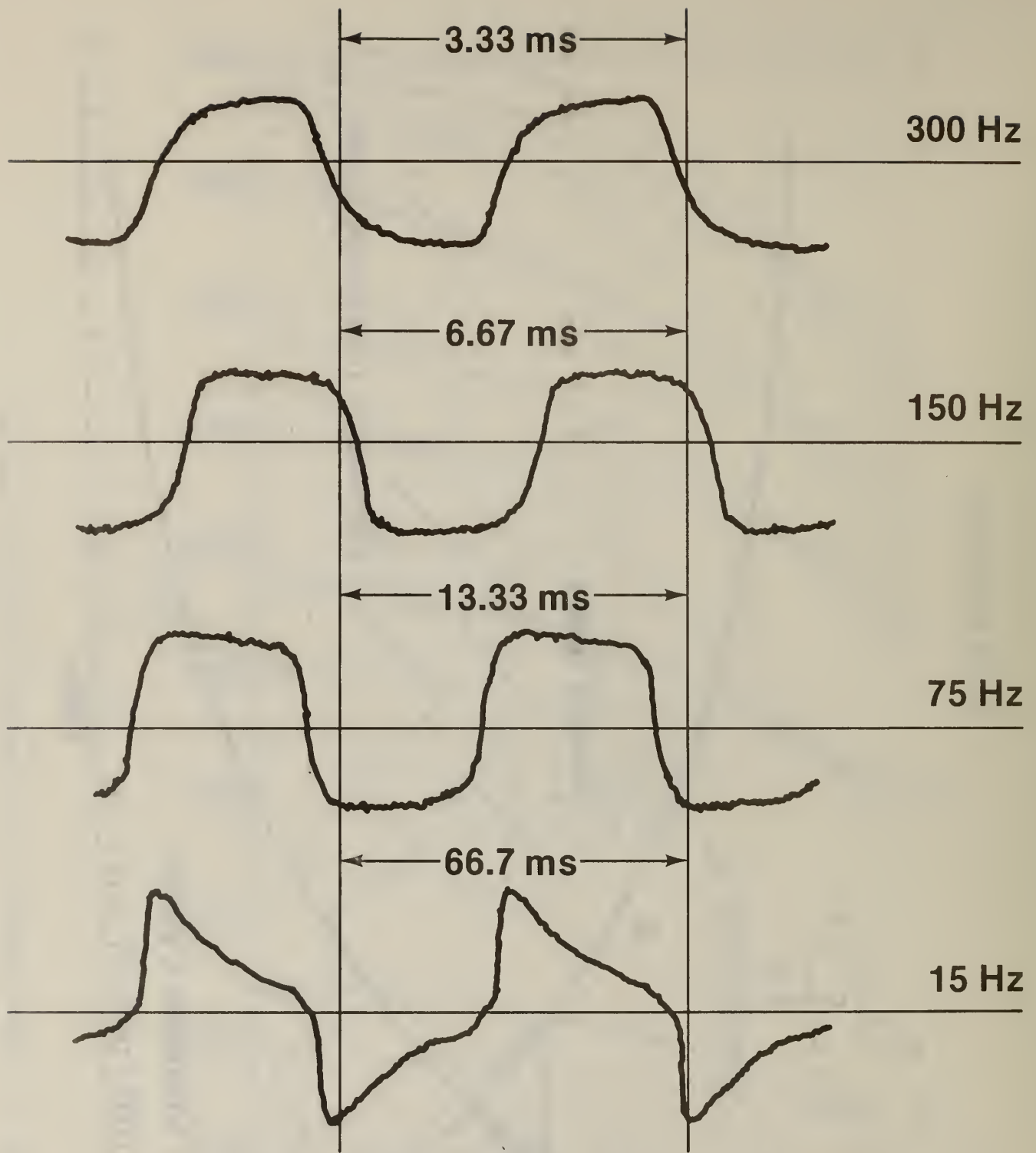Fig. 5. Thermal behavior of an idealized pyroelectric detector.

111

Fig. 6. Oscillograph tracing of the output of a pyroelectric detector at four different light chopping frequencies.

Pyroelectric Detector

Suspension Wire

Spherical Specimen with Blackbody Cavity

Chopper

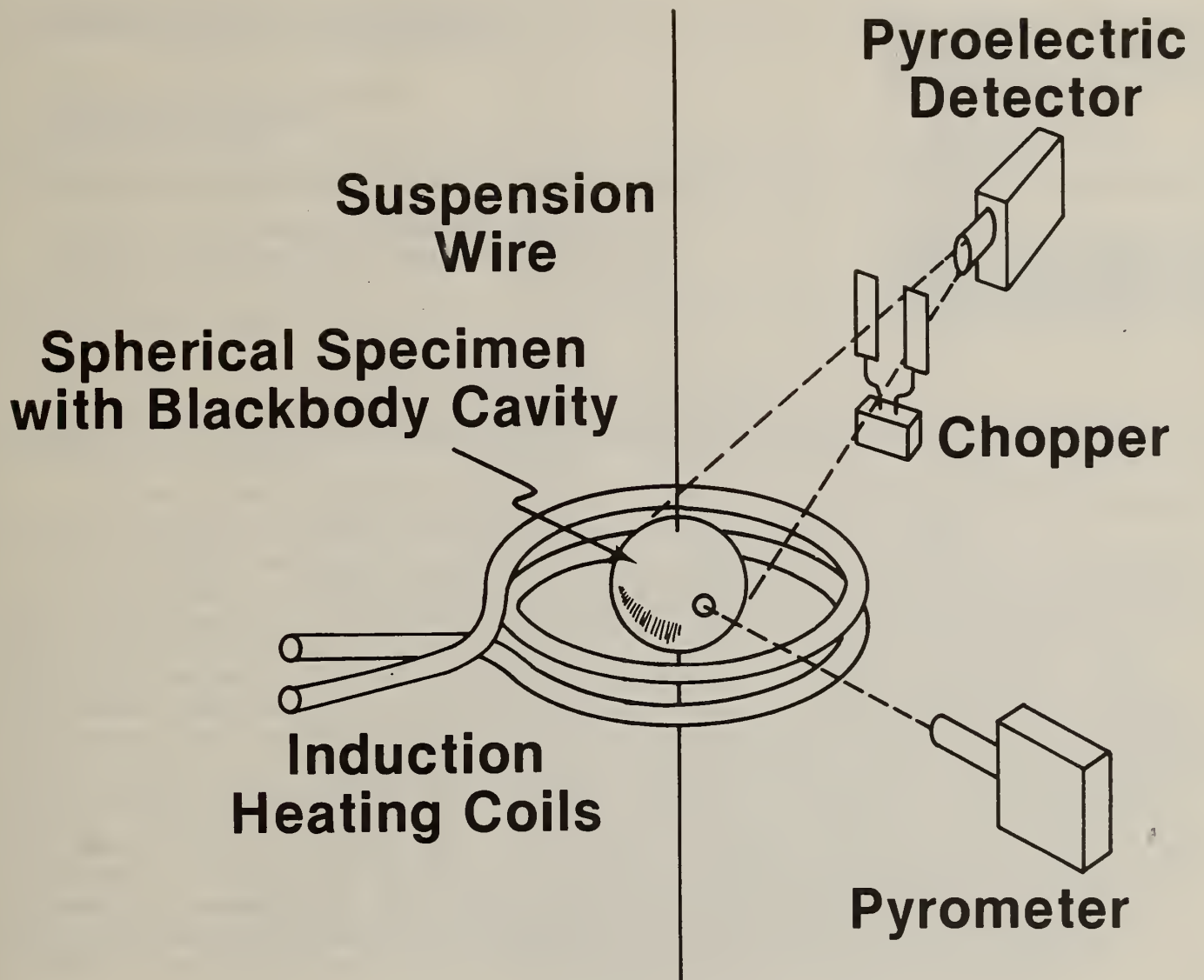**Induction Heating Coils**

Pyrometer

Fig. 7. Diagram of simulated space free-cooling experiment.

U.S. DEPT. OF COMM. BIBLIOGRAPHIC DATA SHEET	1. PUBLICATION OR REPORT NO. NBSIR 80-2082	2. Gov't. Accession No.	3. Recipient's Accession No.

4. TITLE AND SUBTITLE NBS: Materials Measurements	5. Publication Date July 1980
	6. Performing Organization Code

7. AUTHOR(S) J. R. Manning	8. Performing Organ. Report No.

9. PERFORMING ORGANIZATION NAME AND ADDRESS NATIONAL BUREAU OF STANDARDS DEPARTMENT OF COMMERCE WASHINGTON, DC 20234	10. Project/Task/Work Unit No.
	11. Contract/Grant No. Government Order H-27954B

12. SPONSORING ORGANIZATION NAME AND COMPLETE ADDRESS (Street, City, State, ZIP) Materials Processing in Space Program National Aeronautics and Space Administration Washington, DC 20546	13. Type of Report & Period Covered Annual Apr. 1979 – March 1980
	14. Sponsoring Agency Code

15. SUPPLEMENTARY NOTES

☐ Document describes a computer program; SF-185, FIPS Software Summary, is attached.

16. ABSTRACT *(A 200-word or less factual summary of most significant information. If document includes a significant bibliography or literature survey, mention it here.)*

The report describes NBS work for NASA in support of NASA's Materials Processing in Space Program covering the period April 2, 1979 to April 1, 1980.

The results obtained are given in detailed summaries in the body of the report. Briefly, in Task 1 – Surface Tensions and Their Variations with Temperature and Impurities – measurements in an Auger spectrometer of surface impurity concentrations on liquid gallium showed that the principle impurities were oxygen and carbon. The impurities showed a tendency to collect into plates or clumps. In Task 2 – Solutal Convection During Directional Solidification – in Pb-rich Pb-Sn off-eutectic alloys, macrosegregation caused by solutal convection was not reduced by vertical or horizontal fields of 0.1T, but downward solidification (liquid below solid) virtually eliminated macrosegregation in small ($\sim$ 3 mm) diameter samples. In Task 3 – A Thermochemical Study of Corrosive Reactions in Oxide Materials – phase assemblages of selected compositions on the joins $K[Fe_{0.5}Si_{0.5}] O_2 - SiO_2$ and $KFeO_2 - SiO_2$ were determined over a large range of oxygen partial pressures and the temperature range 800 °C to 1400 °C. In Task 4 – Thermodynamic Properties of Refractory Materials at High Temperatures – use of pyroelectric detectors to determine the radiant heat loss from spherical samples as cooling occurs in free-cooling experiments is being investigated.

17. KEY WORDS *(six to twelve entries; alphabetical order; capitalize only the first letter of the first key word unless a proper name; separated by semicolons)*

Auger measurements on liquids; convection; gallium; heat capacity; lead-tin alloys; magnetic field effect; phase diagram; potassium-iron-silicon oxides; solidification; surface tension; thermodynamic properties

18. AVAILABILITY ☒ Unlimited	19. SECURITY CLASS (THIS REPORT) UNCLASSIFIED	21. NO. OF PRINTED PAGES 116
☐ For Official Distribution. Do Not Release to NTIS		
☐ Order From Sup. of Doc., U.S. Government Printing Office, Washington, DC 20402, SD Stock No. SN003-003-	20. SECURITY CLASS (THIS PAGE) UNCLASSIFIED	22. Price $9.00
☒ Order From National Technical Information Service (NTIS), Springfield, VA. 22161		